

SEARCH FOR W' PRODUCTION IN THE SINGLE-TOP CHANNEL WITH THE
ATLAS DETECTOR

By

Patrick True

A DISSERTATION

Submitted to
Michigan State University
in partial fulfillment of the requirements
for the degree of

Physics - Doctor of Philosophy

2014

ABSTRACT

SEARCH FOR W' PRODUCTION IN THE SINGLE-TOP CHANNEL WITH THE ATLAS DETECTOR

By

Patrick True

This thesis presents the search for $W' \rightarrow tb$ using the LHC pp collision data collected with the ATLAS detector at a center-of-mass energy of 8 TeV. The primary backgrounds to this search are ttbar, $W+jets$, and multijets processes. To reduce the contributions of these backgrounds we require a leptonic final state and use Boosted Decision Trees to discriminate between signal and background-like events. This measurement gives limits on the $W' \rightarrow tb$ cross-section times branching ratio and on the ratio of coupling constants g'/g as functions of the W' mass.

ACKNOWLEDGMENTS

Thanks Amber.

TABLE OF CONTENTS

LIST OF TABLES	vii
LIST OF FIGURES	ix
Chapter 1 Introduction	1
Chapter 2 Theory	3
2.1 The Standard Model	3
2.1.1 The forces	4
2.1.2 The particles	6
2.1.2.1 Jets	7
2.1.3 The Lagrangian	9
2.2 Beyond the Standard Model theories	11
2.2.1 Extensions of $SU(2) \otimes U(1)$	12
2.2.2 Effective Lagrangian approach	12
Chapter 3 ATLAS and the LHC	13
3.1 The Large Hadron Collider	13
3.1.1 The Accelerator Chain	13
3.2 The ATLAS detector	15
3.2.1 Detector geometry	15
3.2.2 Magnet system	17
3.2.3 Inner detector	18
3.2.3.1 Pixel detector	20
3.2.3.2 Semiconductor tracker	21
3.2.3.3 Transition radiation tracker	22
3.2.4 Calorimeters	23
3.2.4.1 Electromagnetic Calorimeter	24
3.2.4.2 Hadronic Calorimeter	25
3.2.5 Muon Spectrometer	28
3.2.5.1 Monitored drift tubes	29
3.2.5.2 Cathode strip chambers	31
3.2.5.3 Resistive plate chambers	32
3.2.5.4 Thin gap chambers	32
3.2.6 Triggering and data acquisition	33
Chapter 4 Object Definitions	36
4.1 Electron definition	37
4.2 Muon definition	38

4.3	Jet definition	40
4.3.1	Jet b-tagging	42
4.4	Missing transverse energy definition	43
Chapter 5	Background Simulation	44
5.1	Monte Carlo simulation	44
5.2	Data driven estimates	45
5.2.1	$W+jets$ normalization	47
5.2.2	Multijets estimate	48
Chapter 6	Event selection	49
6.1	Composite objects	49
6.1.1	W boson and neutrino reconstruction	49
6.1.2	Top quark reconstruction	51
6.1.3	W' reconstruction	52
6.2	Data triggers	52
6.3	Cut flow	53
Chapter 7	Multivariate analysis	57
7.1	Boosted decision trees	58
7.1.1	Overtraining	61
7.1.2	Variable selection	62
7.1.3	BDT parameter optimization	64
7.1.4	BDT output distributions	79
Chapter 8	Statistical analysis	81
8.1	Systematic uncertainties	81
8.1.1	Jet energy scale (JES)	81
8.1.2	Jet energy resolution (JER)	83
8.1.3	Jet reconstruction efficiency	84
8.1.4	Jet vertex fraction (JVF)	84
8.1.5	b-tagging performance	84
8.1.6	Lepton energy scale and resolution	85
8.1.7	Lepton trigger and reconstruction	86
8.1.8	Missing transverse energy (MET)	86
8.1.9	Parton distribution function (PDF)	87
8.1.10	Initial state radiation and final state radiation (ISR/FSR)	87
8.1.11	Monte Carlo event generator and parton showering	87
8.1.12	Theoretical cross-sections	88
8.1.13	$W+jets$ normalization	89
8.1.14	Multijet normalization	89
8.1.15	Luminosity	89
8.2	Limit setting procedure	89
8.3	Results	93

Chapter 9 Conclusion	96
BIBLIOGRAPHY	97

LIST OF TABLES

Table 2.1	The fundamental particles of the Standard Model and their properties [1].	8
Table 4.1	Definition of variables used for electron identification cuts [2].	39
Table 4.2	Definition of muidcombined muon reconstruction cuts.	40
Table 5.1	Cross-sections and k-factors for generated W' samples.	46
Table 5.2	Simulated background samples with associated cross-sections, k-factors, generating programs and showering programs.	46
Table 5.3	$W+$ jets normalization factors.	48
Table 6.1	Event yields for signal samples, background samples, and data by analysis channel.	56
Table 7.1	Boosted decision tree variable lists for the four analysis channels. Variables are ranked by importance.	64
Table 7.2	Optimized Boosted decision tree parameters for each of the four analysis channels.	79
Table 8.1	Summary table of the systematic shifts in signal and background event yields of the 1tag analysis channels.	82
Table 8.2	Summary table of the systematic shifts in signal and background event yields of the 2tag analysis channels.	82
Table 8.3	Expected and observed mass limits for a W'_R boson in the individual analysis channels.	94
Table 8.4	Expected and observed mass limits for a W'_L boson in the individual analysis channels.	94

Table 8.5	Expected and observed mass limits for a W'_R boson in the combined analysis channels.	95
Table 8.6	Expected and observed mass limits for a W'_L boson in the combined analysis channels.	95

LIST OF FIGURES

Figure 3.1	Cutaway diagram of the ATLAS detector [3].	16
Figure 3.2	Illustration of the ATLAS magnet system, showing the barrel solenoid, barrel toroid, and endcap toroid coils [4].	19
Figure 3.3	Cutaway diagram of the ATLAS inner detector [5].	20
Figure 3.4	Cutaway diagram of the ATLAS calorimeter systems [6].	24
Figure 3.5	Cutaway diagram of the ATLAS muon spectrometer and toroid magnet systems [7].	30
Figure 6.1	Illustration of the $W' \rightarrow t\bar{b}$ process.	50
Figure 7.1	An example decision tree which sorts input events into signal and background bins. The variables used in the decision tree are described in Section 7.1.2	60
Figure 7.2	Comparison of data to Monte Carlo prediction of the 1st-5th variables by importance in the 2jet 1tag BDT	65
Figure 7.3	Comparison of data to Monte Carlo prediction of the 6th-10th variables by importance in the 2jet 1tag BDT	66
Figure 7.4	Comparison of data to Monte Carlo prediction of the 11th-15th variables by importance in the 2jet 1tag BDT	67
Figure 7.5	Comparison of data to Monte Carlo prediction of the 16th-18th variables by importance in the 2jet 1tag BDT	68
Figure 7.6	Comparison of data to Monte Carlo prediction of the 1st-5th variables by importance in the 3jet 1tag BDT	69
Figure 7.7	Comparison of data to Monte Carlo prediction of the 6th-10th variables by importance in the 3jet 1tag BDT	70

Figure 7.8	Comparison of data to Monte Carlo prediction of the 11th-15th variables by importance in the 3jet 1tag BDT	71
Figure 7.9	Comparison of data to Monte Carlo prediction of the 1st-5th variables by importance in the 2jet 2tag BDT	72
Figure 7.10	Comparison of data to Monte Carlo prediction of the 6th-10th variables by importance in the 2jet 2tag BDT	73
Figure 7.11	Comparison of data to Monte Carlo prediction of the 11th-14th variables by importance in the 2jet 2tag BDT	74
Figure 7.12	Comparison of data to Monte Carlo prediction of the 1st-5th variables by importance in the 3jet 2tag BDT	75
Figure 7.13	Comparison of data to Monte Carlo prediction of the 6th-10th variables by importance in the 3jet 2tag BDT	76
Figure 7.14	Comparison of data to Monte Carlo prediction of the 11th-13th variables by importance in the 3jet 2tag BDT	77
Figure 7.15	The BDT output distribution with the signal and background processes split into testing and training samples for (a) the 2jet 1tag analysis channel (b) the 2jet 2tag analysis channel (c) the 3jet 1tag analysis channel (d) the 3jet 2tag analysis channel.	80

Chapter 1

Introduction

Humanity has always sought to understand. People have progressed from an intuitive understanding of the universe based on practical experience to a more scientific understanding based on logic and the rigorous study of phenomena. The understanding brought about by science has allowed humanity to achieve feats which would otherwise be impossible, and we continue to seek more understanding. At the forefront of this quest, particle physicists work to understand the most basic components of the universe and the most fundamental of interactions between them. The field has progressed from classical theories of the four natural elements, through the chemical elements and nuclear structure, to modern relativistic quantum field theories that describe the most fundamental objects yet imagined. Continuing research in the field takes many forms: precision measurements of trapped and isolated particles over months allow theoretical models to be tested, detection of particles accelerated by supernovae allows access to an energy regime physicists are unable to recreate on Earth, and experiments at particle colliders allow for the investigation of the rarest phenomena.

This dissertation describes the search for $W' \rightarrow t\bar{b}$ using the ATLAS detector at CERN. This is a search for a new particle using the largest detector at the largest, highest energy particle collider ever built and is part of an international research program in collaboration with a multinational research group from around the world. The dissertation is divided into chapters intended to first establish the environment the analysis takes place in, to build up the analysis from basic components, and finally to present the results and put them into

context with the rest of the field. Towards this end the chapters are as follows:

- **Chapter 2** discusses the theoretical background for the analysis.
- **Chapter 3** describes the physical apparatus of the experiment.
- **Chapter 4** defines the analysis level objects reconstructed from the detector response.
- **Chapter 5** details the simulation methods used to model the backgrounds and potential signal processes.
- **Chapter 6** defines the criteria for an event to be included in the analysis.
- **Chapter 7** describes the multivariate analysis technique and its specific implementation.
- **Chapter 8** details the results of the analysis and their statistical significance.
- **Chapter 9** discusses the results of the analysis and their context in current research.

Chapter 2

Theory

High energy physics attempts to deal with the fundamental particles and forces of the universe, and the Standard Model (SM) of high energy physics is the theoretical framework used in this analysis. The Standard Model describes the universe as being composed of 17 fundamental particles and their interactions through three of the four fundamental forces. This analysis is a search for a W' particle not included in the Standard Model which would be indicative of other physical theories, collectively called Beyond the Standard Model (BSM) theories. There are a wide variety of BSM theories therefore this analysis is performed in a model independent manner using an effective Lagrangian. The motivation behind searching for a W' is explored by examining some representative BSM theories and their consequences. The focus of this chapter is not to derive the Standard Model or any BSM theories from first principles, but rather to provide a practical framework and context in which to understand this analysis and the implications of the results.

2.1 The Standard Model

The Standard Model has provided accurate predictions of experimental observables for over 40 years. It was developed after decades of experimentation had catalogued a myriad of particle states. The properties of these states were observed to follow patterns and symmetries, and eventually these symmetries were developed into the Standard Model. The symmetries

of the Standard Model are described in group theory terms as $SU(3) \otimes SU(2) \otimes U(1)$ with each symmetry giving rise to its own conservation law. The Standard Model is a quantum field theory arising from a unification of quantum mechanics and special relativity, and is mathematically described by a Lagrangian [8].

2.1.1 The forces

The Standard Model includes three of the four fundamental forces of nature, the electromagnetic, weak, and strong forces. The electromagnetic and weak forces can be unified into a single electroweak force similar to the unification of the electric and magnetic forces into the electromagnetic force. The electroweak force is described by the $SU(2) \otimes U(1)$ symmetry of the Standard Model and is mediated by the massless photon as well as the massive W and Z bosons. One of the greatest theoretical achievements of the Standard Model was the prediction of the existence and masses of the W and Z bosons well before their experimental discovery. The strong force is described by the $SU(3)$ symmetry of the Standard Model and is mediated by massless gluons. The strong force differs from the electroweak force in that the strong force grows with increased distance between objects while the electroweak force diminishes, which has unique consequences. There have been many attempts to unify the strong force with the electroweak force and even to include a quantum field theory of gravity, such as supersymmetry or string theory. However, there is no clear experimental evidence to support these theories and they are not considered part of the Standard Model [9].

The electroweak force is a unification of the electric, magnetic, and weak forces. The electric and magnetic forces were unified by Maxwell in 1879. The resulting electromagnetic force decreases as the distance between objects increases, and the force is carried to infinite distance by its massless mediator, the photon. The weak force is responsible for a wide

range of observed phenomena, including beta decay and the violation of parity and charge-momentum conservation. These processes can be described with phenomenological theories at low and intermediate energies, however at higher energies above a few GeV the weak theories are unstable on their own. The weak force is similar to the electromagnetic in that the force decreases as the distance between objects increases, however the weak force is mediated by the massive W and Z bosons and so has a limited range of typically 2.5 am. It is only after unification that electroweak theory provides consistent predictions for the energy ranges probed by modern accelerators of up to several TeV [9].

The strong force is responsible for holding baryons, mesons, and nuclei together and is described in the Standard Model by quantum chromodynamics (QCD). QCD describes the strong force using a type of charge called “color” which comes in three colors and their anticolors. Quarks each carry either a color or anticolor charge and gluons, the mediating particles of the strong force, carry both a color and an anticolor charge. The color charge carried by the gluons is a key difference between QCD and quantum electrodynamics (QED) in which the mediating particle is charge neutral. This means that gluons are self-interacting and do not form a free gluon field and also that QCD is not locally gauge invariant and so it is a non-Abelian gauge theory. This leads to antishielding of bare color charges by the vacuum and the force between colored objects becoming larger as the distance between them increases. This corresponds with the fact that only colorless objects are observed in nature and with the formation of particle shower “jets”, as discussed further in Section 2.1.2.1, from what would otherwise be bare color charged objects [9].

2.1.2 The particles

The Standard Model contains 17 fundamental particles and their anti-particles which compose all objects. These particles can be classified into leptons, quarks, and bosons as shown in Table 2.1. For each particle in Table 2.1 there is a corresponding anti-particle with opposite electric charge. In general a particle name or symbol refers to both the particle and its anti-particle except where they are explicitly distinguished between, thus “electron” refers to both electrons and positrons in general. The structure visible in Table 2.1 is not accidental and is vital to our understanding of the particles.

The six lepton flavors can be classified into 3 generations, each containing a charged lepton and a neutrino. The charged leptons all are massive and carry an electrical charge of -1, while the neutrinos are electrically neutral and their masses have not been directly observed. The current best limits on the mass of each neutrino flavor are given in Table 2.1 because the observation of neutrino flavor oscillations [10] implies that neutrinos are not massless but no mass measurements have been made yet. The leptons do not interact through the strong force, so the charged leptons only interact through the weak and electromagnetic forces and the neutrinos can only interact weakly. Because neutrinos can only interact through the weak force their interaction with matter, such as a detector, is rare and specialized experiments are necessary to study them. In contrast the first generation charged lepton, the electron, is easily detected through electromagnetic interactions and is readily available in nature. This difference in detectability has lead to the term “lepton” generally indicating the charged leptons with the neutrinos being indicated separately.

Similar to the leptons, the quarks can also be described by 3 generations, each containing 2 flavors. Each generation contains one quark with an electric charge of $2/3$ and one quark

with an electric charge of $-1/3$, called up-type and down-type respectively based on the first generation quarks with those charges. Quarks interact through all 3 of the forces in the Standard Model and thus are readily detectable using a variety of methods. Since quarks have a color charge, bare quarks will typically form jets as described in Section 2.1.2.1 and cannot be directly measured.

The final group of particles in Table 2.1 is the bosons. The bosons all have integer spins, with the photon, gluon, W and Z bosons all being spin 1 and the Higgs boson being spin 0. The photon, W and Z bosons are the mediating particles of electroweak theory with the W and Z bosons gaining their masses through the Higgs mechanism. The Higgs mechanism adds a quartic complex scalar field potential to the theory which is locally gauge invariant. Through an appropriate choice of parameters the field is made to have a non-zero expectation value and induce spontaneous symmetry breaking in the $SU(2) \otimes U(1)$ electroweak group. After further reparameterization and an appropriate choice of gauge, what is left is the massive W and Z bosons, the massless photon, and a new massive Higgs boson, which was just recently discovered at the LHC [11, 12]. The final boson is the gluon which mediates the strong force. The gluon has a color and anticolor charge which makes it self-interacting, and a bare gluon will form a jet as described in Section 2.1.2.1.

2.1.2.1 Jets

Jets are phenomenological objects that are formed when individual colored particles, single quarks and gluons, are produced at sufficiently high energies. As the colored particle moves away from the initial colored object it is connected to, the energy of the strong interaction between them increases until it becomes energetically favorable to produce a quark-antiquark pair from the vacuum for the particle and the initial colored object to be bound to. This

Particle	Symbol	Mass	Charge [e]	Spin
Leptons				
Electron	e	511 KeV	-1	1/2
Electron Neutrino	e_ν	<2.05 eV	0	1/2
Muon	μ	106 MeV	-1	1/2
Muon Neutrino	μ_ν	<0.17 MeV	0	1/2
Tau	τ	1.78 GeV	-1	1/2
Tau Neutrino	τ_ν	<18.2 MeV	0	1/2
Quarks				
Up	u	2.3 MeV	2/3	1/2
Down	d	4.8 MeV	-1/3	1/2
Charm	c	1.28 GeV	2/3	1/2
Strange	s	95 MeV	-1/3	1/2
Top	t	173 GeV	2/3	1/2
Bottom	b	4.18 GeV	-1/3	1/2
Bosons				
Photon	γ	0	0	1
W^\pm Boson	W^\pm	80.4 GeV	± 1	1
Z Boson	Z	91.2 GeV	0	1
Gluon	g	0	0	1
Higgs	H	126 GeV	0	0

Table 2.1: The fundamental particles of the Standard Model and their properties [1].

production of new hadrons is called hadronization and it absorbs a small amount of the initial colored particle's energy. This hadron will decay and the process will repeat itself until there is insufficient energy remaining for further hadronization, creating a narrow shower of hadrons that in total have the same energy and momentum as the original colored particle. This particle shower is called a jet and it is used as the detectable stand-in for the original particle. This is a general picture of what happens to bare quarks and gluons and there are subtle differences depending on the flavor of the initial particle, in particular if the initial particle is a top or bottom quark. Because of their large mass, top quarks almost exclusively decay into a W boson and bottom quark before hadronization can occur creating a very different signal from other quarks. Bottom quarks also have unique phenomenology in that the hadron produced with the initial bottom quark has an unusually long lifetime and will travel a detectable distance before the b quark decays and further hadronization takes place, creating a secondary vertex [9].

2.1.3 The Lagrangian

The mathematics of the Standard Model is typically formulated in terms of a Lagrangian L and the Lagrangian density \mathcal{L} such that $L = \int \mathcal{L} d^3x$. The Standard Model includes many different phenomena so it is useful to group the terms of the Lagrangian density by the physical motivation as seen in Equations 2.1 [13].

$$\mathcal{L} = \mathcal{L}_{EW} + \mathcal{L}_{QCD} + \mathcal{L}_{Yuk} \quad (2.1)$$

The Lagrangian density that describes the electroweak force is given in Equation 2.2.

$$\mathcal{L}_{EW} = -\frac{1}{4}F_{\mu\nu a}F_a^{\mu\nu} + D_\mu\phi D^\mu\phi - \mu^2\phi^2 - \lambda(\phi^2)^2 \quad (2.2)$$

The first term describes the electroweak interactions with the index a running over the photon, W and Z bosons. $F_{\mu\nu}$ is the electroweak field tensor and is defined as:

$$F_{\mu\nu} = \partial_\mu A_\nu - \partial_\nu A_\mu - [A_\mu, A_\nu] \quad (2.3)$$

Since electroweak theory is abelian, $[A_\mu, A_\nu] = 0$ and $F_{\mu\nu}$ is simplified. The last three terms of Equation 2.2 describe the Higgs field. The first of these is the kinetic term where D_μ is the covariant derivative defined as:

$$D_\mu = \partial_\mu - gA_\mu \quad (2.4)$$

The final two terms of the electroweak Lagrangian density describe the Higgs potential.

The QCD Lagrangian density is given in Equation 2.5.

$$\mathcal{L}_{QCD} = \sum_j \bar{\psi}(i\gamma^\mu D_\mu - m_j)\psi - \frac{1}{4}G_{\mu\nu a}G_a^{\mu\nu} \quad (2.5)$$

The first term describes the quarks with index j running over all six of the quarks with masses m_j . The covariant derivative D_μ is similar to Equation 2.4 but now contains eight gauge fields corresponding to the eight gluons denoted by the index a :

$$D_\mu = \partial_\mu - g_a A_{\mu a} \quad (2.6)$$

The second term of the QCD Lagrangian density describes the gluons. $G_{\mu\nu a}$ is analogous

to $F_{\mu\nu}$ in the electroweak Lagrangian density, but for each of the eight gauge fields.

$$G_{\mu\nu a} = \partial_\mu A_{\nu a} - \partial_\nu A_{\mu a} - [A_{\mu a}, A_{\nu a}] \quad (2.7)$$

Since QCD is a non-abelian theory, $[A_{\mu a}, A_{\nu a}] \neq 0$ and $G_{\mu\nu a}$ does not simplify in the same way as $F_{\mu\nu}$.

The Yukawa Lagrangian density describes the fermions and is given in Equation 2.8.

$$\mathcal{L}_{Yuk} = \sum_a \bar{\psi} (i\gamma^\mu D_\mu - G_a \phi) \psi \quad (2.8)$$

The index a runs over the fermions, with the covariant derivative defined in Equation 2.4. The mass of each fermion is determined by $G_a \phi$ where G_a is the fermion's coupling to the Higgs field ϕ , and in this way the Higgs field gives the fermions their masses.

2.2 Beyond the Standard Model theories

While the Standard Model has described the observations of particle physics experiments for over 40 years, there are known problems with the theory. The Standard Model does not include gravity, which has been experimentally verified many times. There is no mechanism to produce the amount of matter-antimatter asymmetry that is observed in the universe. The Standard Model does not include a suitable dark matter particle to match astronomical observations. While mathematically possible, the observed masses of the W and Z bosons require very precise cancellations of parameters which seem unnatural. While this list is by no means exhaustive, there have been decades of work to solve these problems with BSM theories.

2.2.1 Extensions of $SU(2) \otimes U(1)$

Theories that include a W' boson often extend the $SU(2) \otimes U(1)$ electroweak symmetry which describes the W boson. The simplest such extension is $SU(2) \otimes SU(2) \otimes U(1)$, where the new $SU(2)$ can be a right handed extension of the left handed $SU(2)$ group which describes the Standard Model weak interactions or some other $SU(2)$ symmetry. The $SU(2) \otimes U(1)$ symmetry can also be extended by embedding the $SU(2)$ into a group of higher degree, resulting in symmetries such as $SU(3) \otimes U(1)$ or $SU(4) \otimes U(1)$. Each of these extensions contains a myriad of specific theories with different coupling structures and a variety of experimental predictions [1]. Since there is currently no strong experimental evidence to distinguish between these theories, this analysis does not assume any specific theory but instead uses an effective Lagrangian approach.

2.2.2 Effective Lagrangian approach

In all of these theories the W' boson is described by a Lagrangian density term of the form given in Equation 2.9.

$$\mathcal{L}_{W'} = \frac{1}{2\sqrt{2}} V'_{ij} W'_\mu \bar{f}^i \gamma^\mu (g'_R (1 + \gamma_5) + g'_L (1 - \gamma_5)) f^j \quad (2.9)$$

This Lagrangian density includes arbitrary right handed and left handed coupling strengths g'_R and g'_L respectively. These coupling strengths are a common metric across all models regardless of how they are determined within each theory, and thus they are a model independent parameter which can be experimentally measured or constrained. For this analysis we use benchmark W'_R and W'_L models where g'_R and g'_L are equal to g_L for the Standard Model W.

Chapter 3

ATLAS and the LHC

The search for $W' \rightarrow t\bar{b}$ requires a very large and extensive experimental setup. In order to set limits competitive to those currently in the literature, particles need to be collided with atleast several TeV of energy, and in order to correctly identify W' events from the background the products of these collisions need to be carefully measured. The ATLAS (A Toroidal Lhc ApparatuS) experiment meets these criteria, it is the largest collider detector ever built and is capable of very precise measurements of the products of particle collisions. The collisions it measures are produced by the Large Hadron Collider (LHC) which is designed to collide particles with up to 14 TeV center of mass energy.

3.1 The Large Hadron Collider

3.1.1 The Accelerator Chain

The LHC is only the final accelerator in a chain designed to take ions from rest, accelerate and collide them at up to 14 TeV center of mass energy. This acceleration occurs in stages, with protons being accelerated through a separate chain than other ions such as lead. Since my analysis uses only proton-proton collisions I will detail only their acceleration here. The proton source is a bottle of hydrogen gas, which is stripped of its electrons and accelerated to a 50 MeV proton beam by the Linac2 linear accelerator [14]. This 50 MeV proton beam

is then passed to the Proton Synchrotron Booster (PSB) which accelerates the beam to 1.4 GeV in four superimposed synchrotron rings before injecting the bunches into the Proton Synchrotron (PS). By adjusting the timings of the four superimposed rings of the PSB and varying which rings the PS is filled from a plethora of bunch patterns can be selected based on the current operating goals [15]. The PS accelerates the proton beam from 1.4 GeV to 25 GeV in a 628 meter circumference synchrotron. The PS also does the final bunch splitting, creating the bunch pattern which will be kept through the remainder of the beam acceleration and collision [16]. After being accelerated and bunched by the PS, the beams enter the Super Proton Synchrotron (SPS) for final acceleration and tuning before injection into the LHC. The SPS is a synchrotron nearly 7 km in circumference which accelerates the proton beam up to 450 GeV before injecting it into the LHC [17].

The final stage of the accelerator chain is the LHC itself. The LHC is a 27 km circumference synchrotron with 2 superimposed rings which resides in what was previously the Large Electron-Positron collider (LEP) tunnel at CERN. It consists of 1104 superconducting dipole magnets designed to reach a peak field of 8.33 T to bend the proton beams around the ring, and 384 quadrupole magnets per ring to control the focusing of the beams. Each ring has a further 536 quadrupole, 1608 sextupole, 784 octupole, and 616 decapole magnets to control the beams and correct instabilities in the beams due to couplings during acceleration and collision. Nominally the LHC is designed to collide proton bunches at ATLAS every 25 nanoseconds with a center of mass energy of 14 TeV, however it is still early in the LHC program and these were not the conditions that the 2012 dataset was taken under. Due to difficulties with the magnet fault protection system the collisions took place with 8 TeV center of mass energy, and because the accelerator and beams are being actively studied a variety of beam configurations were used with bunches separated by 25-75 nanoseconds [18].

3.2 The ATLAS detector

The ATLAS detector is one of two large general purpose experiments which studies collisions produced by the LHC. It is designed to able to perform a wide variety of searches and measurements by collecting as much information as possible about the products of each collision. ATLAS uses a multilayered design that has become standard for large collider experiments and can be seen in Figure 3.1. The innermost portion is called the inner detector which provides fine granularity tracking of charged particles. Moving radially outwards from the interaction point the next detectors are the calorimeters which measure the energy of the particles, and the outermost portion of the detector consists of the muon system which detects and tracks muons traveling through ATLAS. Each of these portions of ATLAS are made up of sub-detector systems designed to work together with the other systems and provide more information than any single technology detector [19].

3.2.1 Detector geometry

Before detailing each detector system that makes up ATLAS it is useful to discuss the coordinate system used in the experiment. The center of the detector is taken to be the origin and the z-axis extends along the beam line with positive being counterclockwise around the LHC when viewed from above. The x-axis points towards the center of the LHC and the y-axis points vertically upwards. While this forms a complete basis to describe the detector and it is sometimes used, it is not the most common coordinate system. Ignoring gravitational effects all directions transverse to the beams are equivalent and can be described by an angle ϕ taken to be 0 along the x-axis and increasing right-handedly with respect to the z-axis. The angle from the beam line is a common parameter for describing decays. However because

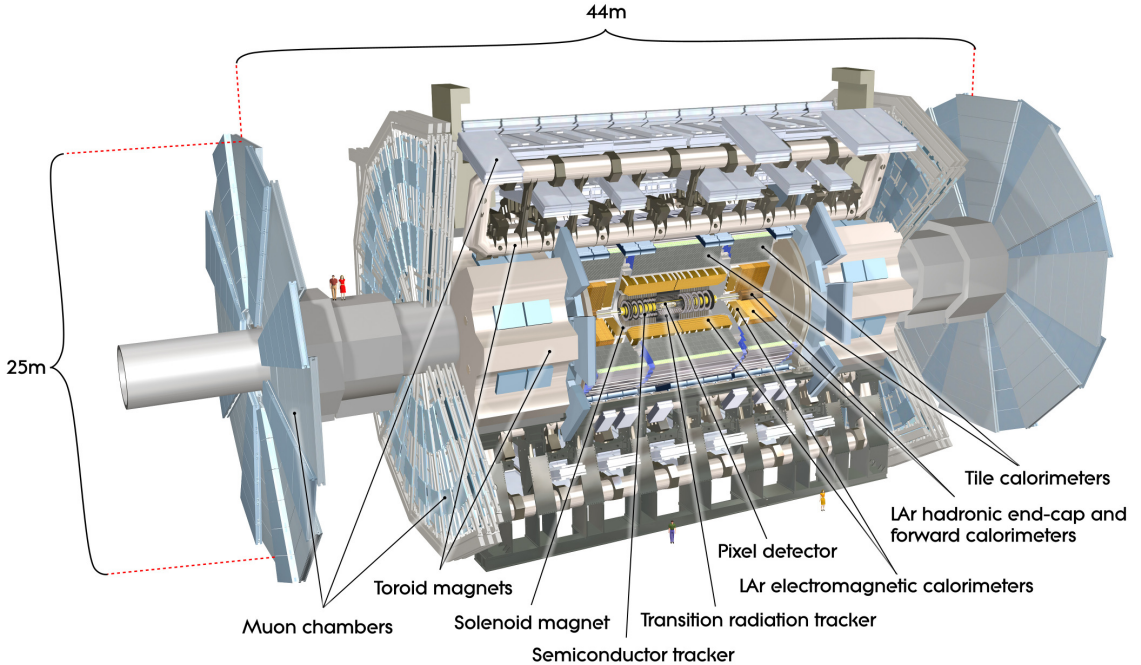


Figure 3.1: Cutaway diagram of the ATLAS detector [3].

objects are produced with Lorentz boosts in the z direction ranging from 0 to nearly 1 it is more useful to use a relativistic invariant to describe this angle. The equation for the Lorentz invariant rapidity (y) is:

$$y = \frac{1}{2} \ln \left(\frac{E + p_z}{E - p_z} \right) \quad (3.1)$$

While useful, the rapidity of a particle is dependent on the particle's mass and a different rapidity coordinate system to describe the detector would be necessary for each mass. Almost all particles produced by the LHC have $m \ll E$ so we can calculate rapidity with $m = 0$ and it is approximately the rapidity for all particles produced by the LHC. This is called the pseudorapidity (η).

$$\eta = \frac{1}{2} \ln \left(\frac{|\vec{p}| + p_z}{|\vec{p}| - p_z} \right) \quad (3.2)$$

Which can be rewritten using the angle from the z-axis (θ) as:

$$\eta = -\ln \left(\tan \left(\frac{\theta}{2} \right) \right) \quad (3.3)$$

Thus pseudorapidity is a purely geometric quantity, with $\eta = 0$ corresponding to the transverse plane and $|\eta| = \infty$ corresponding to the beamline. In detector parlance regions with small $|\eta|$ are called “central” and regions with larger $|\eta|$ are called “forward.”

3.2.2 Magnet system

The ATLAS detector has three large superconducting magnet systems, the superconducting solenoid, the barrel toroid, and the endcap toroids as shown in Figure 3.2. The purpose of these magnets is to bend the path of charged particles as they propagate through the detector. With careful tracking of a charged particle’s path through the magnetic field, it is possible to determine the particle’s momentum [19].

The superconducting solenoid is a cylinder 5.3 m long and 2.63 m in diameter. It has 1173 turns of superconducting wire in a single layer along its length with an operating current of 7.6 kA. The inner volume contained by the solenoid has a central magnetic field of 2 T with a peak field of 2.6 T at the superconducting wire. The solenoid is designed to be as thin as possible in order to minimize the interaction between itself and particles from physics events. The particles pass through the 19 cm thick (at most 0.66 radiation lengths) solenoid before they enter the calorimeters [20].

The barrel toroid consists of 8 coils each of which is a 25.3 m long and 5.35 m wide

“racetrack” design. These magnets run the length of ATLAS with their long dimension running parallel to z and their short dimension running radially. They are spaced evenly around the detector with their outer edge at a radius of 10.05 m. Each coil contains 120 turns of superconducting wire with an operating current of 20.5 kA which produces a peak field of 3.9 T [20].

The two endcap toroids complete the ATLAS magnet system. Each endcap contains 8 coils of a racetrack design similar to the barrel toroid, however these coils are 4.5 m in the radial direction and 5 m in the z direction. The endcap coils are offset from the barrel toroid coils by 22.5° in ϕ so that they bisect the angle between adjacent barrel toroid coils. They are aligned in z to share a common outer edge with the barrel toroid, and are placed radially from 0.825 m to 5.35 m. With 116 turns per coil of superconducting wire carrying 20 kA, the endcap toroids produce a peak field of 4.1 T [20].

3.2.3 Inner detector

The ATLAS inner detector is designed to provide excellent tracking information for charged particles with $|\eta| < 2.5$ produced by the LHC and is comprised of three concentric subsystems as shown in Figure 3.3. The pixel detector is nearest the beamline and provides the most precise position information with 97 million channels across three layers in the barrel region and with 43 million channels across five disk layers at both ends. Moving radially outwards from the beamline the next subsystem is the semiconductor tracker (SCT) which uses eight layers of thin silicon microstrip sensors in the barrel and 44 sensor layers in each endcap, with alternating layers at a 40 mrad angle to each other to allow full determination of position. The final subsystem of the inner detector is the transition radiation tracker (TRT) which is a straw tube system consisting of a barrel section containing axial straws and 18 radial straw

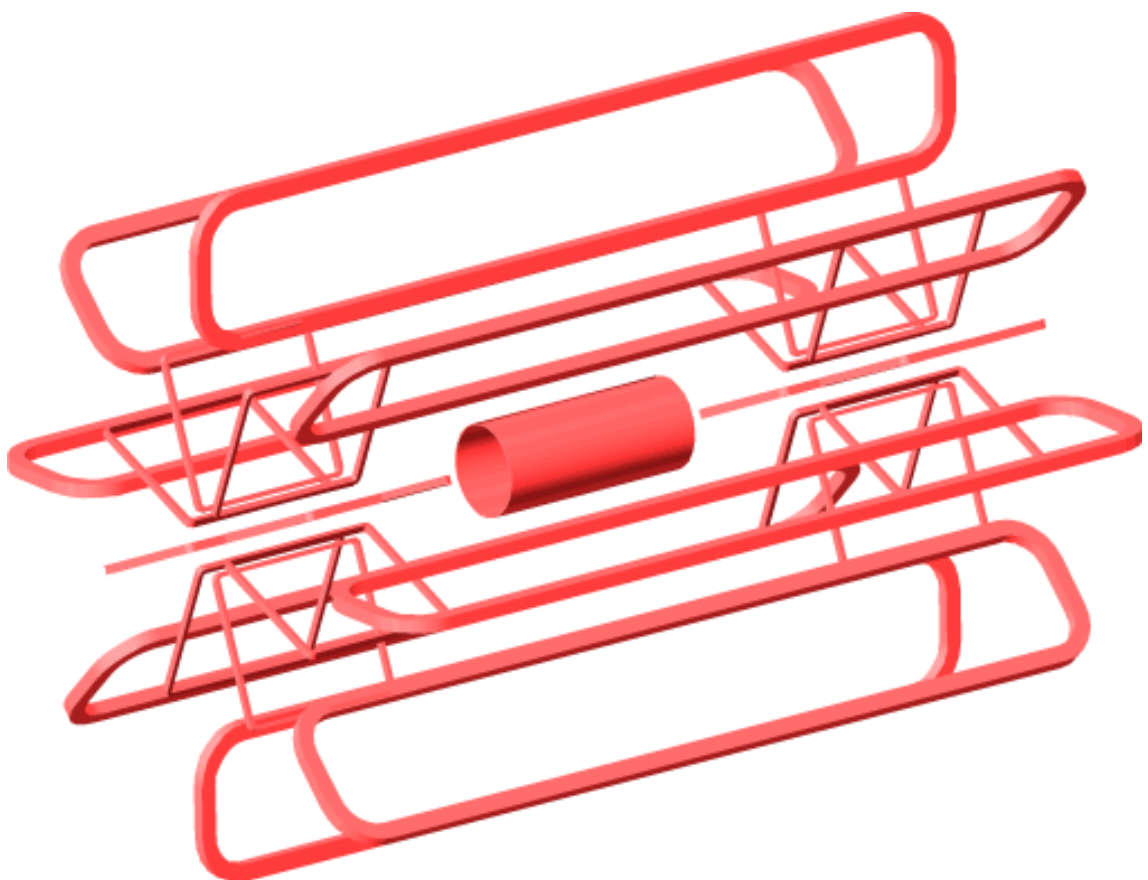


Figure 3.2: Illustration of the ATLAS magnet system, showing the barrel solenoid, barrel toroid, and endcap toroid coils [4].

wheel segments in each endcap, designed so that most particles will transverse 36 detecting straws [19].

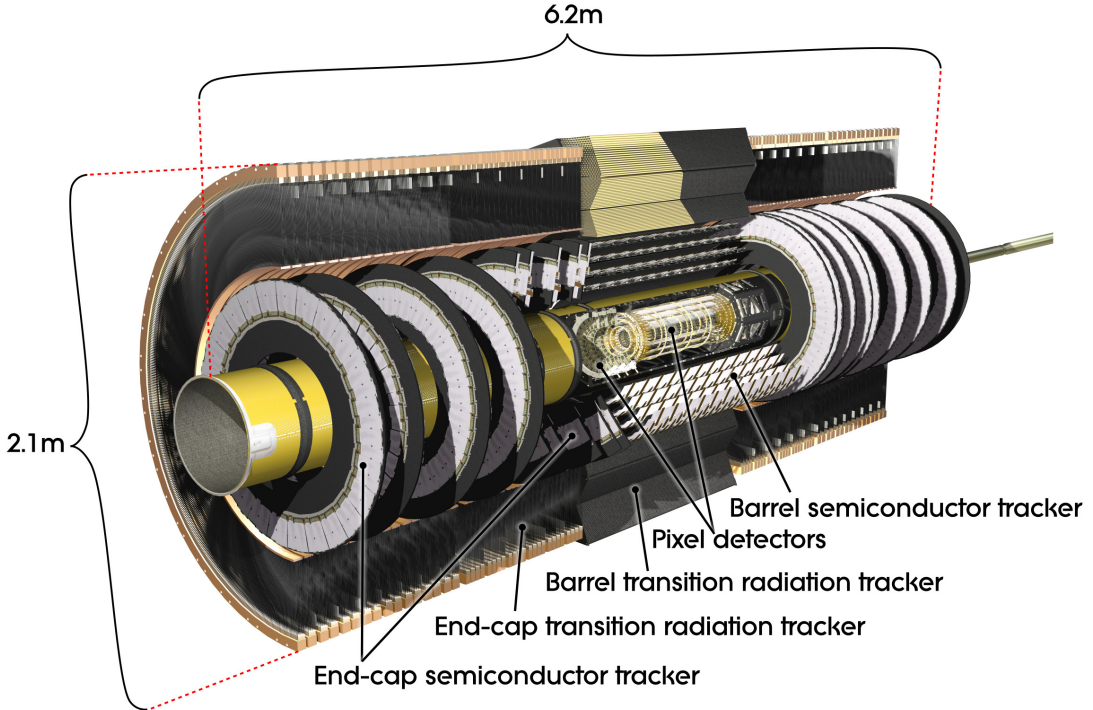


Figure 3.3: Cutaway diagram of the ATLAS inner detector [5].

3.2.3.1 Pixel detector

The pixel detector has the highest granularity and offers the best positioning and tracking information of charged particles in ATLAS. The system contains three barrel layers with three transverse disk layers at each end. The barrel layers are all 801 mm long, with the innermost layer located at a mean radius of 50.5 mm, the middle layer at 88.5 mm, and the outermost layer at 122.5 mm. The disk layers are all identical annuli with an inner radius of 89 mm and outer radius of 150 mm. These disks are placed at a mean $|z|$ of 495 mm, 580 mm, and 650 mm. This gives the pixel detector a total detecting area of 1.7 m^2 and

coverage of $|\eta| \leq 2.5$ [19] [21].

The active medium in the detector is silicon sensor cells $50 \mu\text{m} \times 400 \mu\text{m}$ in size. In the barrel layers the long dimension is in the z direction and in the disk layers the long dimension is radial. These sensor cells are bump bonded to readout chips with each chip reading an 18×160 cell array. The signal from each cell is amplified and compared to a programmable threshold on each chip. If the signal exceeds the threshold the location is stored in a buffer on the chip to be read out via optical link in the case of a level 1 trigger acceptance, as detailed in Section 3.2.6 [19, 21].

3.2.3.2 Semiconductor tracker

While the pixel detector provides the highest resolution for tracking particles, the technology is not cost-effective to use to cover the larger areas corresponding to larger radii. The next subdetector is the semiconductor tracker (SCT) with four cylinders at radii of 299 mm, 371 mm, 443 mm, and 514 mm and nine disks at both endcaps with mean $|z|$ of 853.8 mm - 2720.2 mm. Each cylinder is 1492 mm long and contains two layers of silicon microstrip sensors at a 40 mrad angle to each other. The microstrip sensors are each 63.6 mm wide and 64 mm long rectangles divided into 768 microstrips each $16 \mu\text{m}$ wide [22]. The endcap disks have a more complicated geometry with each disk containing 1-3 “rings” of sensor modules depending on position. Each endcap module has two layers of microstrip silicon sensors at a 40 mrad angle to each other, similar to the barrel modules, however unlike the barrel modules the endcap microstrip sensors are tapered to form trapezoidal segments rather than rectangular. This tapering also causes variable microstrip widths of $16 \mu\text{m} - 20 \mu\text{m}$. Each module for both the endcap and barrel regions has four silicon sensors (two per layer) attached to central logic circuits which amplify the signals from each microstrip and compare

them to a programmable threshold. Similar to the pixel detector, the channels with signals exceeding the threshold are stored in a buffer to be read out if the event is accepted by the level 1 trigger system [19, 22, 23].

3.2.3.3 Transition radiation tracker

The final subdetector of the inner detector is the TRT. While both the pixel detector and SCT use variations of silicon detector technology, the TRT uses a modification of drift tube technology to detect particles. The TRT is divided into one barrel and two endcap sections. The barrel section consists of 52544 straw-tubes arranged in 73 layers parallel to the beam axis. Each straw-tube is a drift tube 1441 mm long and 4 mm in diameter and contains a 70% Xe, 27% CO_2 and 3% O_2 gas mixture. Each straw-tube also contains a central 31 μm diameter gold-plated W-Re wire which is held at a potential of -1.53 kV relative to the straw-tube wall [24].

The endcaps are each made up of 122,880 straw-tubes arranged radially in 160 layers. These straw-tubes are identical to those used in the barrel except that they are each 370 mm long. These endcap straw-tubes are bundled into modules called wheels of 8 layers each, and the wheels are distributed with $848mm \leq |z| \leq 2710mm$ to give nearly uniform coverage in η [25]. Overall the barrel covers $|\eta| < 1.0$ and the endcaps cover $1.0 < |\eta| < 2.0$ with most particles traversing a total of 30 straw-tubes.

As a charged particle traverses each straw it causes primary ionization within the gas, which undergoes avalanche multiplication as it accumulates toward the wire giving an amplification factor of 2.5×10^4 with the operating gas mixture and voltage. The unique feature of the ATLAS TRT is that surrounding each straw-tube is a layer of transition radiation (TR) material. The TR material is made up of many layers of polypropylene and polyethylene,

and is designed to maximize the production of transition radiation produced by charged particles traversing the boundary between the two materials with different dielectric constants. The transition radiation produced in the TR material is generally a soft x-ray photon which is absorbed by the xenon in the straw-tubes, ionizing the xenon and producing an energy cascade much larger than a typical ionizing particle does when traversing a straw tube. This is particularly useful because electrons and charged pions are difficult to discriminate between, however the energy of transition radiation is proportional to $\gamma = E/m$ which allows for an additional rejection factor of 50-100 depending on the electron quality definition as described in Section 4.1 [19, 26].

3.2.4 Calorimeters

Having measured the positions of particles as precisely as possible in the inner detector, the next detector systems particles will encounter are designed to measure their energy. The electromagnetic (EM) calorimeter is nearest the beamline covering $|\eta| < 3.2$ and uses liquid argon (LAr) technology with lead absorber plates in a distinctive accordion pattern. The hadronic calorimeter resides around the EM calorimeter, using scintillating tiles with iron absorbers in the barrel region of $|\eta| < 1.7$ and using LAr technology with copper and tungsten absorbers in the $1.5 < |\eta| < 3.2$ and $3.1 < |\eta| < 4.9$ regions respectively. The layout of these systems can be seen in Figure 3.4. It is important that the calorimeter system provides the best containment of particles possible while maintaining good energy resolution so that the total energy of events can be determined [19].

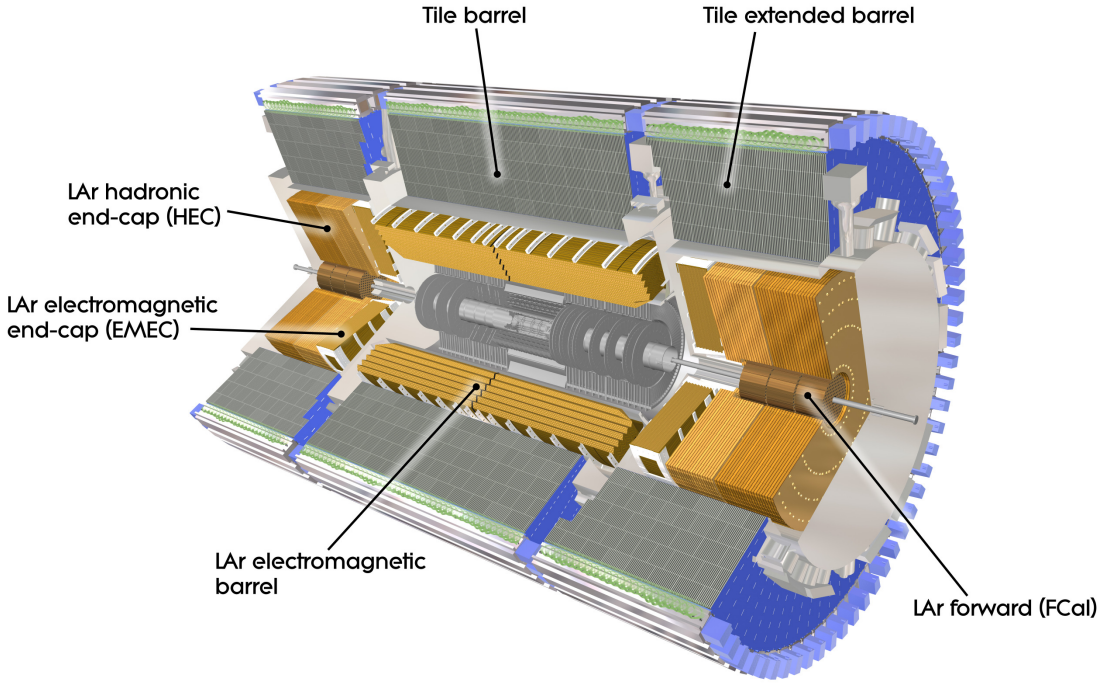


Figure 3.4: Cutaway diagram of the ATLAS calorimeter systems [6].

3.2.4.1 Electromagnetic Calorimeter

The ATLAS EM calorimeter is divided into a barrel section, a presampler, and two endcap sections. The barrel calorimeter is made up of two half barrels which surround the superconducting solenoid and covers the range $|\eta| < 1.475$ with one half barrel covering $\eta > 0$ and the other half barrel covering $\eta < 0$. Each half barrel is a cylinder 3.2 m long and has a 2.8 m inner radius and 4 m outer radius. There are 1024 accordion-shaped absorber plates arrayed radially in each half barrel with the oscillations increasing in amplitude as radius increases which provides uniform density in ϕ . The absorbers are 1.53 mm thick lead for $|\eta| < 0.8$ and 1.13 mm thick lead for $0.8 < |\eta| < 1.475$ with 0.2 mm thick stainless steel sheets glued to each side to provide structural support. Centered between consecutive absorbers is a readout electrode held at 2 kV relative to the absorber with the 2 mm gap between the electrode

and absorber filled with liquid argon. Electrically charged incident particles will shower via Bremsstrahlung in the absorber and this shower will exit the thin absorber layer and enter the liquid argon. The shower ionizes the liquid argon and this ionization is collected at the electrode where it is amplified and read out at both the inner and outer edges of the calorimeter [27].

The presampler is a 22 mm thick detector covering the interior of the barrel calorimeter. It is similar to the barrel detector in that uses liquid argon with 1.9-2.0 mm gaps between electrodes, however unlike the barrel calorimeter the presampler has no absorbers. The purpose of the presampler is to measure showers produced by interactions with the material between the interaction point and the EM calorimeter and improve the energy resolution of the EM calorimeter [28].

The endcap sections are each a wheel 630 mm thick with a 330 mm inner radius and 2098 mm outer radius which covers $1.375 < |\eta| < 3.2$. Each wheel is further divided into an inner wheel and an outer wheel by a 3 mm gap located at $|\eta| = 2.5$. The endcaps have a design similar to the barrel calorimeter, with accordion-shaped absorber plates placed radially and readout electrodes interleaved. Each outer wheel contains 768 absorbers of 1.7 mm thick lead, while the inner wheels each have 256 absorbers of 2.2 mm thick lead. The endcap sections also have an 11 mm thick presampler of similar design to that used in the barrel section [19, 29].

3.2.4.2 Hadronic Calorimeter

The hadronic calorimeter makes up the remainder of the ATLAS calorimeter system and is comprised of four sub-systems; the tile barrel calorimeter and tile extended barrel calorimeter are both based on using iron absorber plates with plastic scintillator tiles interspersed,

while the hadronic endcap calorimeter and the forward calorimeter are both based on LAr technology similar to the EM calorimeter. The tile barrel calorimeter has an inner radius of 1144 mm and an outer radius of 2115mm and a length of 5640 mm. The tile barrel calorimeter consists of 64 modules, each of which is a radial slice of the detector. Each module consists of 64 steel plates that are each 5 mm thick and run the radial length of the module. Between consecutive full length plates there are 11 alternating layers of scintillating plastic tiles and steel spacing tiles which is 4 mm thick. These layers progressively increase in length from the inner radius to the outer radius in order to provide high precision measurements while maintaining the necessary depth of interaction lengths to contain very energetic jets. A 1.5 mm gap along both edges of each alternating layer contains a wavelength shifting fiber which carries the scintillation light to photomultiplier tubes located along the outer radius of the modules where the signals are amplified, digitized and processed by readout electronics. The extended barrel calorimeter consists of two sections, one at each end of the tile barrel calorimeter. Each of these sections is 2900 mm long but otherwise follows the same general design as the tile barrel calorimeter with minor modifications to 12 of the 64 modules in each extended barrel calorimeter to accommodate necessary structural supports for the LAr cryostat. A gap region exists between the tile barrel calorimeter and the extended barrel calorimeter on each side. This gap is necessary to provide services to the LAr calorimeters and the inner detector, and while approximately 750 mm wide it is adjusted as needed to accomodate these necessary services. The gap region contains the intermediate tile calorimeter which consists of an irregular arrangement of absorber and scintillator tiles used to estimate the energy lost in the dead material of the gap region. In total the tile barrel calorimeter covers the $|\eta| < 1.0$ region while the extended barrel calorimeter covers $0.8 < |\eta| < 1.7$ and the intermediate tile calorimeter covers $0.8 < |\eta| < 1.0$ [30].

The hadronic endcap calorimeter consists of two wheels located outside of the electromagnetic endcap calorimeters at both ends of the detector, for a total of four wheels. Each of these wheels is further made up of 32 identical wedge-shaped modules. The front wheel on each side starts at a $|z|$ of 4,277 mm and is 816.5 mm in length. The rear wheels start at a $|z|$ of 5134 mm with a length of 961 mm, leaving a 2 mm gap between the wheels. Each front wheel module contains 25 parallel copper plates which are each 25 mm thick and are evenly spaced in z and arrayed transverse to the beamline. The rear wheel modules each contain 17 parallel copper plates which are 50 mm thick and are also evenly spaced in z and arrayed transverse to the beamline. This means that all of the plates are separated by 8.5 mm gaps which are filled with liquid argon. Three electrodes are evenly spaced in each gap with the outer two electrodes held at 2000 V and the central electrode providing the signal for amplification and processing. All of the plates have an outer radius of 2090 mm and the first 9 plates of the front wheels has an inner radius of 372 mm while the remaining plates all have an inner radius of 475 mm, providing coverage in the region $1.5 < |\eta| < 3.2$ [31].

The final sub-system of the ATLAS hadronic calorimeter is the forward calorimeter. This system covers the region $3.1 < |\eta| < 4.9$ and resides entirely inside the 475 mm inner radius of the hadronic endcap calorimeter. This region is extremely harsh with very high radiation densities and many design compromises were necessary to ensure the forward calorimeter could survive and operate in this environment. The forward calorimeter is composed of three sections at each end of the detector. These sections are cylindrical and are arranged coaxially along the length of the beam pipe as seen in Figure 3.4. Each section is made of an absorber matrix cylinder with holes along its length in a honeycomb pattern. Each of these holes contains a thin walled electrode tube and an electrode rod of slightly smaller radius. The small gap between the electrode rod and tube is filled with liquid argon and the

electrode rod is held at 250 V relative to the electrode tube. In the section on either side of the detector which is nearest the interaction point the absorber matrix and the electrode rod are both made of copper. In the remaining sections the absorber matrix and electrode rods are made of tungsten. These materials were chosen due to their densities as well as their thermal properties, ability to be produced to the necessary specifications, and hadronic shower sizes. In all of the modules the electrode tube is made of copper and the electrical signal is read out from each absorber rod for amplification and processing. The liquid argon gaps are smaller than is common in LAr detectors, being $269 \mu m$, $376 \mu m$, and $508 \mu m$ in the three sections at each end of the detector and increasing with the distance from the interaction point. This is necessary to prevent charge accumulation in the liquid argon which would degrade performance and is caused by the high radiation density of the region, which decreases with distance from the interaction point. The overall layout of the segments is approximately projective from the interaction point, with the inner radius of the segments increasing proportional to $|z|$, the electrode spacing increasing from 7.50 mm to 9.00 mm across the three segments, and the number of electrodes decreasing from 12,260 tubes in each module nearest the interaction point to 8224 electrodes in each module furthest from the interaction point [32, 33].

3.2.5 Muon Spectrometer

The ATLAS Muon Spectrometer (MS) is the outermost of the ATLAS detector systems and accounts for a majority of the detector's volume. The purpose of this system is to detect muons as they traverse the ATLAS detector and making precision position measurements at three different detector layers to calculate the momentum of each muon based on the curvature of the muon's trajectory as it travels through the ATLAS magnetic field. To accomplish

this goal the muon spectrometer has four subsystems which employ differing detector technologies as needed in the various regions of the ATLAS detector. Monitored Drift Tubes (MDTs) and Cathode Strip Chambers (CSCs) provide high precision tracking information over the large area of the muon spectrometer in three concentric layers, called stations. The MDT system uses gas drift tube technology and covers the region $|\eta| < 2.7$, while the CSC system uses multiwire proportional chambers with a cathode strip readout and covers $2.0 < |\eta| < 2.7$. Both the MDT and CSC systems have long response times and are not capable of being used in the Level 1 trigger system as described in Section 3.2.6, so two additional muon spectrometer systems are employed for the initial detection of muons. The Resistive Plate Chamber (RPC) covers the region $|\eta| < 1.05$ using resistive plate capacitors which locally discharge when their internal gas is ionized while the Thin Gap Chamber (TGC) systems covers $1.05 < |\eta| < 2.4$ using multiwire proportional chambers with a smaller geometry than the CSC system [34]. The overall layout of these systems is shown in Figure 3.5.

3.2.5.1 Monitored drift tubes

The monitored drift tube (MDT) chambers provide the majority of the precision muon tracking capability in ATLAS. MDT modules are arranged into barrel and end-cap regions, with the barrel composed of three concentric cylinders with radii of 5, 7.5, and 10 m with coverage of $|\eta| < 1.0$ and the endcap regions containing four disks each at $|z|$ of 7, 10, 14, 22 m respectively and covering the range $1.0 < |\eta| < 2.7$. Each chamber is composed of two sets of drift tube multilayers on either side of a rigid support structure which is 150 mm thick. The multilayers in MDT chambers in the stations nearest the interaction point have four layers of drift tubes while all other MDT chamber multilayers have three layers of drift tubes. Each drift tube is 30 mm in diameter and is filled with a 91% Ar, 4% N_2 ,

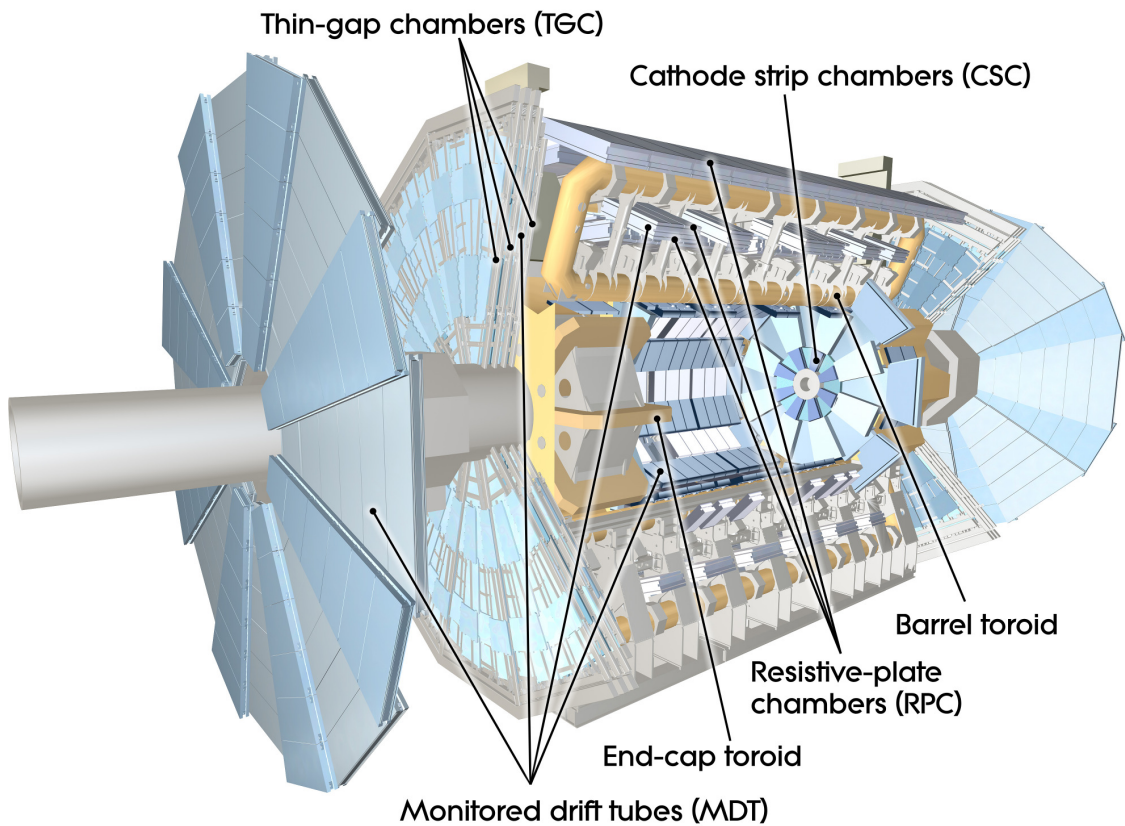


Figure 3.5: Cutaway diagram of the ATLAS muon spectrometer and toroid magnet systems [7].

5% CH_4 gas mixture. Each tube is read out from a central 50 μm tungsten wire. The wire is held at 3270 V and gives a spacial resolution of 80 μm with a maximum drift time of approximately 500 ns. Because of this long drift time it is necessary to correlate the signals from the MDT system with corresponding signals in the RPC and TGC systems which provide much more prompt results in order to determine which bunch crossing the MDT signals originate from [34].

3.2.5.2 Cathode strip chambers

The cathode strip chambers (CSCs) are multiwire proportional chambers used for precision muon position measurements in the region of highest radiation density, $2.0 < |\eta| < 2.7$ in the station nearest to the interaction point. Similar to the MDT, the CSC consists of two multilayers with each multilayer containing four monolayers. Each monolayer is a 5.08 mm gas gap containing a 30% Ar, 50% CO_2 and 20% CF_4 gas mixture. In the center of each gas gap is a plane of parallel anode wires. The anode wires are 30 μm diameter tungsten wires separated by 2.54 mm and held at 2600 V. The walls forming the gap are copper-clad and etched to form thin cathode strips. The cathode strips on one of the walls run orthogonal to the anode wires and provide the precision coordinate measurement, while the cathode strips on the other wall are coarser and run parallel to the anode wires to provide the transverse coordinate measurement. For the precision strips it is only necessary to read out every third strip in order to exceed the resolution of the MDT by using charge interpolation between the strips, and these read-out strips are separated by 5.08 mm. The final resolution in the bending direction is 60 μm for a monolayer [34].

3.2.5.3 Resistive plate chambers

The resistive plate chambers (RPCs) are designed to complement the MDT system in the barrel region ($|\eta| < 1.05$). Each RPC chamber is a simple design; two resistive plates form a capacitor and are held at 8900 V with a 2 mm gap filled with 97% $C_2H_2F_4$ and 3% C_4H_{10} . An incident muon will ionize the gas and cause a local discharge of the capacitor. This discharge is read out via capacitative coupling by metal strips running in orthogonal directions on both sides of the resistive capacitor. The RPC chambers are placed two thick at each of three stations. The two middle stations are directly inside and outside of the middle MDT barrel station, and the far station is directly inside of the outer MDT barrel station. This system provides prompt muon detection with a delay of less than 10 ns and a timing uncertainty of 1.5 ns. The signal position is known to within a resolution of 1 cm which is used by the level 1 trigger system and provides a complementary position measurement to the MDT [34].

3.2.5.4 Thin gap chambers

The thin gap chambers (TGCs) fill a role similar to the RPC, prompt detection of muons for use in level 1 triggering and a complementary position measurement to the MDT, but in the endcap region ($1.05 < |\eta| < 2.4$). The TGCs are based on multiwire proportional chamber technology similar to the CSCs but with a smaller geometry and faster readout time. Each TGC gas gap is 2.8 mm wide and is filled with a highly quenching 55% CO_2 and 45% $n - C_5H_{12}$ gas mixture. A central plane of $50 \mu m$ tungsten anode wires are spaced 1.8 mm apart and are held at 3100 V. The signals from these wires are read out with 4-20 wires forming an individual readout channel depending on η . Signals are also read out from etched copper strips on one of the walls of each gap to provide a measurement of the azimuthal angle

for each track. This configuration gives each gap a position resolution of approximately 9 mm and a time response of 7 ns, which is sufficient for bunch identification and use by the level 1 trigger system. TGC modules are made up of either gas gap doublets or triplets with 20 mm of separation between consecutive gas gaps. The inner wheel at $|z| = 7\text{ m}$ of each endcap has a layer of doublet chambers and the middle layer wheel at $|z| = 14\text{ m}$ has two layers of doublet chambers and a layer of triplet chambers, giving the total system a depth of nine gaps [34].

3.2.6 Triggering and data acquisition

As described in Section 3.1, proton bunch crossings occur inside the ATLAS detector every 25 ns. With the size and complexity of the ATLAS detector (the average event is 1.3 Mbytes of data [19]) it is not possible to read out and store the detector response for every bunch crossing, thus a trigger and data aquisition system (TDAQ) has been implemented to identify and record the most interesting events. The trigger system is divided into three levels, each of which takes as input the accepted events of the previous level and itself reduces the rate of accepted events using increasingly complex algorithms. The level 1 (L1) trigger uses local information in the calorimeter and muon systems to reduce the accepted event rate from 40 MHz to 75 kHz, the level 2 (L2) trigger uses more precise information including tracking from the inner detector for the region of interest (RoI) that caused the level 1 acceptance to further reduce the accepted event rate from 75 kHz to 3.5 kHz, and the event filter (EF) is the final trigger level which uses the highest granularity information from the entire detector to further reduce the accepted event rate from 3.5 kHz to the 200 Hz which is saved for analysis.

The level 1 trigger has an event input rate of 40 MHz and a maximum event acceptance

rate of 75 kHz with a total latency of $2.0 \mu s$. The 40 MHz input event rate means that no single part of the trigger decision can take more than 25 ns, which is achieved by using a highly parallelized hardware implementation. The electromagnetic liquid-argon calorimeter and hadronic tile calorimeter systems as well as the RPCs and TGCs in the muon spectrometer each have their signals read out to the level 1 trigger system. The calorimeter signals are processed by hardware located in the ATLAS counting room adjacent to the cavern which houses ATLAS, while the muon system signals are processed by hardware located on the ATLAS detector. These level 1 trigger processors each only process their local detector area and operate at a lower granularity than the systems are ultimately capable of. The processors look for energy clusters above a variety of set thresholds depending on the system and region of the detector, with an above threshold area forming a region of interest (RoI). The exception to the local scope of the level 1 trigger system is a special processor which calculates the total transverse energy of each event as well as the missing transverse energy of each event and compares them to a variety of thresholds. All of the processors send a list of surpassed thresholds to the central trigger processor (CTP) which correlates and counts the multiplicity of surpassed thresholds and determines a level 1 trigger decision for each event based on a programmable trigger menu [35].

The level 2 trigger has an event input rate of 75 kHz from the level 1 trigger and event acceptance rate of 3.5 kHz with a total latency of 10 ms. Unlike the level 1 trigger, the level 2 trigger system uses all of the ATLAS detector systems and is implemented in software. For each event, the detector signals for all of the systems are read out in each of the RoIs identified by the level 1 trigger system to a node in the level 2 server farm. A series of algorithms are then applied in software to the event depending on the exact level 1 trigger conditions in order to refine the measurements. A final level 2 decision is reached based on

the outcome of these algorithms [36].

The final level of the trigger system is the event filter. The event filter has an event input rate of 3.5 kHz and a final event acceptance rate of 200 Hz with a latency of 1 s. This trigger level is very similar to the level 2 trigger system however rather than only calculating a trigger decision based on the RoIs, the event filter calculates a decision based on the entire event. Each event accepted by the level 2 system has all of the detector systems read out to a node in the event filter server farm. Based on the complete event information a lengthier and more precise calibration is performed, and based on this more detailed information an event filter decision is calculated. Events which are accepted by the event filter are read out from ATLAS to be saved for analysis [35].

Chapter 4

Object Definitions

In order to perform a search for $W' \rightarrow t\bar{b}$ each event needs to be reconstructed from the raw ATLAS data. This raw data is a collection of energy deposits in the calorimeters and tracking hits from the inner detector and muon spectrometer which needs to be refined into a more useable form. The raw data is reconstructed into analysis objects which generally correspond to the particles that passed through the detector. Different types of particles will interact with the various detector systems in different ways, leaving distinct signatures:

- Electrons leave a track in the inner detector and an energy shower in the EM calorimeter.
- Muons leave a track in the inner detector and in the muon spectrometer with minimal energy deposited in the calorimeters.
- Jets leave tracks in the inner detector and energy showers in the EM and hadronic calorimeters.
- Photons do not leave a track in the inner detector and produce only an energy shower in the EM calorimeter.
- Neutrinos do not interact with the detector but their presence can be inferred from an imbalance in the total event momentum in the transverse plane.

For the $W' \rightarrow t\bar{b}$ analysis the objects of interest are electrons, muons, jets, and the missing transverse energy (MET) corresponding to a neutrino. It is possible for “fake” objects to be created due to detector resolution effects or by other particles interacting with the detector in rare or unexpected ways. For example, jets that deposit all of their energy in the EM calorimeter before reaching the hadronic calorimeter would appear to be electrons while electrons that do not lose all of their energy in the EM calorimeter and “punch-through” to the hadronic calorimeter can appear to be jets. The object definitions are chosen to balance the rejection of fakes with acceptance of real objects.

4.1 Electron definition

Electrons are a key component of the $W' \rightarrow t\bar{b}$ and their reconstruction uses a complex algorithm to identify them at high efficiency while keeping the fakes rate low. In order to have access to higher efficiency or higher purity samples as needed the electrons are reconstructed with increasingly stringent requirements to form three qualities. The requirements for the 3 electron qualities of loose, medium and tight are summarized in Table 4.1. The reconstruction starts by performing a sliding window search of the middle layer of the EM calorimeter, where a $3 \times 5 (\eta \times \phi)$ window of calorimeter cells (each 0.025×0.025 in $\eta \times \phi$) is moved about the calorimeter to find the local maxima of energy enclosed. Maxima with an energy above 2.5 GeV are called seed clusters. Seed clusters are then checked against the tracking information, and clusters with a track within $\Delta\eta$ and $\Delta\phi$ requirements determined by the electron quality are considered electron candidates [2].

Electron candidates have their energy recomputed using a $3 \times 7 (\eta \times \phi)$ window of calorimeter cells with corrections applied based on the position and energy and are assigned

a four-momentum based on the tracking and corrected energy. A final set of cuts shown in Table 4.1 is applied to electron candidates based on the quality, with cut values optimized in 10 bins of η and 11 bins of cluster transverse energy (E_T), where $E_T = \frac{\text{cluster } E}{\cosh(\text{track } \eta)}$ [2]. In addition to these requirements the tight electrons are required to pass an enhanced set of cuts. Electron candidates are rejected if they are in the EM calorimeter crack region of $1.37 < |\eta| < 1.52$ because the calorimeter performance is degraded. The E_T is required to be greater than 25 GeV because this analysis is focused on high energy events. Electron candidates are rejected if they have $\Delta R < 0.4$ with a jet, where $\Delta R = \sqrt{\Delta\eta^2 + \Delta\phi^2}$. The final requirement for tight electrons is that they are isolated in the tracker and calorimeter as defined by cutting on the parameters Ptcone30 and Etcone20 respectively, with both cuts being energy dependent with 90% efficiency. Ptcone30 is the sum of the p_T of all tracks in a cone with half opening angle of 0.3 minus the p_T of the candidate's track. Similarly, Etcone20 is the sum of the E_T in a cone with half opening angle of 0.2 minus the E_T of the cluster.

4.2 Muon definition

Muons are of approximately equal importance to the analysis as electrons, but thankfully they are much easier to identify and reconstruct in ATLAS. As described in Section 3.2.5, the muon spectrometer is the largest ATLAS sub-detector and is dedicated to identifying and measuring muons. Muons are reconstructed with different qualities similar to how electrons are reconstructed. This analysis only uses muons reconstructed with the “muidcombined” quality so only that algorithm is described here. Muidcombined muon candidates are formed by independently reconstructing a track in the muon spectrometer (MS) and inner detector

Type	Cut Description
Loose electrons	
Detector acceptance	<ul style="list-style-type: none"> • $\eta < 2.47$
Hadronic leakage	<ul style="list-style-type: none"> • Ratio of the E_T in the first layer of the hadronic calorimeter to the EM cluster E_T ($\eta < 0.8$ and $\eta > 1.37$) • Ratio of the E_T in all layers of the hadronic calorimeter to the EM cluster E_T ($0.8 < \eta < 1.37$)
EM calorimeter middle layer	<ul style="list-style-type: none"> • Ratio of the 3×7 cell energy to the 7×7 cell energy • Shower width in η
Medium electrons (including Loose cuts)	
EM calorimeter first layer	<ul style="list-style-type: none"> • Total shower width • Ratio of the difference in the largest and second largest energy deposits to the sum of those energies
Track quality	<ul style="list-style-type: none"> • Number of hits in the pixel detector (≥ 1) • Sum of hits in the pixel detector and SCT (≥ 7) • Transverse impact parameter (< 5 mm)
Track matching	<ul style="list-style-type: none"> • $\Delta\eta$ between the track and cluster (< 0.01)
Tight electrons (including Medium cuts)	
Track quality	<ul style="list-style-type: none"> • Number of hits in the first layer of the pixel detector (≥ 1) • Transverse impact parameter cut (< 1 mm)
Track matching	<ul style="list-style-type: none"> Ratio of the cluster energy to the track momentum • $\Delta\phi$ between the track and cluster (< 0.02) • $\Delta\eta$ between the track and cluster (< 0.005)
TRT	<ul style="list-style-type: none"> • Number of hits in the TRT • Ratio of the number of high-threshold hits to the total number of hits
Photon conversion	<ul style="list-style-type: none"> • Matches to reconstructed photon conversions are rejected

Table 4.1: Definition of variables used for electron identification cuts [2].

Type	Cut Description
Muon energy	<ul style="list-style-type: none"> • $p_T > 25 \text{ GeV}$
Detector acceptance	<ul style="list-style-type: none"> • $0.1 < \eta < 2.5$
Track quality	<ul style="list-style-type: none"> • Number of pixel hits + number of crossed dead pixel cells > 0 • Number of SCT hits + number of crossed dead SCT strips ≥ 5 • Number of crossed dead pixel cells + number of crossed dead SCT strips < 3 • For $0.1 < \eta < 1.9$: number of TRT hits + number of TRT outliers > 5 and $\frac{\text{number of TRT outliers}}{n_{\text{TRT}}} < 0.9$ • Distance along z from track to primary vertex $< 2 \text{ mm}$
Isolation	<ul style="list-style-type: none"> • $\frac{\text{MiniIso10_4}}{\muon p_T} < 0.05$ • Muon and all jets with $p_T > 25 \text{ GeV}$ have $\Delta R > 0.4$

Table 4.2: Definition of muidcombined muon reconstruction cuts.

(ID), and if these tracks match within $\Delta R < 0.05$ then a combined track is reconstructed from both systems. Several cuts are detailed in Table 4.2 which ensure that only well-defined tracks that lie in the most sensitive regions of the detector and that are isolated from other activity are included in the analysis. Two new variables are introduced in these cuts, nTRT is the sum of the number of TRT hits and the number of TRT outliers while MiniIso10_4 is the sum of the p_T of all objects inside a cone with half opening angle of 0.1 minus the muon p_T with a maximum of 40 GeV.

4.3 Jet definition

As described in Section ??, bare quarks and gluons undergo hadronization before they can interact with the detector. This forms a multitude of tracks and calorimeter enrgy deposits in a spread, which is treated as a single object called a jet. Being of such a composite nature, jets are complicated objects and there are many different ways to define and reconstruct them.

This analysis uses the *anti*– k_t algorithm [37] to define and reconstruct jets. The *anti*– k_t algorithm starts with a list of all objects, in this case the calorimeter cell energies. From this list of objects, a list of all distances is computed where the distance between objects is defined in Equation 4.1, and the distance between the object and the beam as defined in Equation 4.2. If the minimum distance is between two objects then they are merged to form a new object, the original objects are removed from the list and the new object is added to the list, then all distances are recalculated. If the minimum distance is between an object and the beam then the object is classified as a jet and removed from the list. This process is repeated recursively until the object list is exhausted. In Equation 4.1 the parameter R is the characteristic size of the jet. Larger values of R produce fewer, wider jets which are more likely to contain products from more than one parton. Conversely smaller values of R produce more, smaller jets that may not contain all of the products of individual partons. For this analysis $R = 0.4$, consistent with other ATLAS top quark analyses.

$$d_{ij} = \min(p_{T,i}^{-2}, p_{T,j}^{-2}) \frac{\Delta\eta_{ij}^2 + \Delta\phi_{ij}^2}{R^2} \quad (4.1)$$

$$d_i = p_T^{-2} \quad (4.2)$$

After forming jets with the *anti*– k_t algorithm a correction is applied to each jet based on the jet's position and p_T to correct for the specific response of each region of the detector. The corrected jets then have a series of quality cuts applied. Any jets with negative energy are removed as these are unphysical. If any jets are within $\Delta R < 0.2$ of an electron, the jet nearest the electron is removed because it is likely a double counting of the electron as a jet.

4.3.1 Jet b-tagging

Jets that originate from different particles can often exhibit different kinematics, and by analyzing the kinematics of a given jet it is possible to predict the flavor of the parton that produced the jet. This process is generally referred to as “tagging”, with jets that pass the tagging criteria called “tagged” and jets that fail the tagging criteria called “untagged”. In this analysis b-tagging is employed to sort jets based on how likely they are to have originated from a b quark (b-jets). Specifically, the MV1 [38] b-tagging algorithm is used.

MV1 is a neural network analysis of ATLAS b-tagging algorithms SV0, IP3D+SV1, and JetFitterCombNN. SV0, IP3D+SV1, and JetFitterCombNN all use the secondary vertex caused by the b quark’s relatively long hadronization time, as discussed in Section ??, to distinguish b-jets from other jets. This secondary vertex can be parameterized into the transverse and longitudinal impact parameters (d_0 and z_0) which are the distances between the secondary and primary vertex in the radial or z projection respectively, or the decay length (L_0) which is the distance between the primary and secondary vertex. SV0, IP3D+SV1, and JetFitterCombNN use varying mixtures of these parameters as well as the parameters’ significances, which are defined as the ratio of the parameter and its uncertainty, to discriminate between b-jets and all other jets [39]. MV1 uses the outputs of these other b-tagging algorithms to produce a single weight that corresponds to how likely a jet is to have originated from a b quark. For this analysis a tagging cut on each jet is placed at the 70% b tagging efficiency value, which means that 70% of b quark initiated jets are expected to pass the cut and be tagged.

4.4 Missing transverse energy definition

With particles colliding nearly head-on along the beam line, the sum of the products' momenta in the transverse plane should be approximately 0. However, neutrinos and some theoretical exotic particles are not expected to interact with the ATLAS detector, causing the measured final state to have an imbalance in the transverse momentum. The negative of this measured imbalance is called the missing transverse energy (MET). Unfortunately MET is sensitive to any mismeasurement in the detector as well as the possibility of being faked by an interacting particle missed by the detector by traveling through cracks or dead regions. To correct for these different sources individual calibrations are applied to soft jets, hard jets, electrons, muons, and cell-out energy fragments. Hard jets are jets as defined in Section 4.3 with $p_T > 20 \text{ GeV}$. Soft jets are jets as defined in Section 4.3 with $20 \text{ GeV} > p_T > 10 \text{ GeV}$. Electrons and muons are defined using the definitions in Section 4.1 and Section 4.2 respectively. Cell-out energy fragments are any energy in the calorimeter which is not included in the other objects [40].

Chapter 5

Background Simulation

In order to devise and optimize the analysis strategy both signal and background events are modeled. Most of these events are simulated using Monte Carlo (MC) techniques where each event is generated, showered and hadronized, run through a detector simulation, and reconstructed using a variety of software packages. The exception to this are the W+jets and multijet backgrounds which are modeled using either partially or wholly data driven techniques as described in Sections 5.2.1 and 5.2.2 respectively.

5.1 Monte Carlo simulation

The MC simulation of events is broken down into four stages. Event generation simulates the initial physics event and its decay. Showering and hadronization simulate the formation of jets from any bare quarks or gluons in the generated events. Detector simulation models the interaction of the physics event with the ATLAS detector using a GEANT4 [41] simulation of the ATLAS detector, resulting in a detector response for the event. The final step is event reconstruction where the same algorithms used to analyze data events are applied to the simulated detector responses to build analysis objects.

There are a plethora of software packages available to perform MC simulation of events, and these packages make a variety of different assumptions and simplifications of the physics they are simulating. This leads to the situation that different packages are able to more

accurately simulate different physics processes and careful consideration and investigation is necessary to ensure the simulations used in the analysis are as accurate as possible. Since $W' \rightarrow t\bar{b}$ is a single top process it was extremely useful to consult the extensive work already done comparing the different MC generator and showering programs for each process by the ATLAS single top group.

For all processes except W' the current group recommendation has been used. For the W' signal processes the MADGRAPH [42] generator has been used due to its ease of implementation and handling of spin correlations of decays. The W' events were showered with PYTHIA [43] similar to most of the background signals. Table 5.2 shows which programs were chosen to simulate each sample's generation and showering [42] [43] [44] [45] [46] [47]. With the exception of the data driven methods described in Section 5.2, the background and signal samples are normalized using their theoretical cross-sections (σ), the total luminosity (\mathcal{L}), and a k-factor (k) which estimates the higher order corrections to the cross-section. Equation 5.1 gives the normalized number of events expected for each sample (N). The cross-section and k-factor values for the signal and background samples are given in Table 5.1 and Table 5.2 respectively.

$$N = k\sigma\mathcal{L} \quad (5.1)$$

5.2 Data driven estimates

While the above method works well to simulate many background processes, it is sometimes useful to use control regions of data to estimate some backgrounds. For W+jets it is necessary to correct the overall normalization as well as the relative abundance of the simulated samples

W' Mass [GeV]	W'_L σ [pb]	W'_L k	W'_R σ [pb]	W'_R k
500	12.333	1.3684	17.510	1.2906
750	2.7223	1.3144	3.7174	1.2779
1000	0.81915	1.2564	1.0652	1.2796
1250	0.28025	1.2405	0.37278	1.2260
1500	0.10618	1.2202	0.13932	1.2183
1750	0.043693	1.1893	0.055667	1.2062
2000	0.018551	1.1774	0.023718	1.1740
2250	0.0082073	1.1638	0.010283	1.1669
2500	0.0038171	1.1512	0.0046794	1.1485
2750	0.0018512	1.1529	0.0021970	1.1522
3000	0.00095811	1.1687	0.0011035	1.1592

Table 5.1: Cross-sections and k-factors for generated W' samples.

Process	σ [pb]	k	Generator	Showering
single top s-channel	1.6424	1.1067	POWHEG	PYTHIA
single top t-channel	25.750	1.1042	ACERMC	PYTHIA
single top Wt-channel	20.461	1.0933	POWHEG	PYTHIA
$t\bar{t}$	114.51	1.1992	POWHEG	PYTHIA
W+lf	31994	1.133	ALPGEN	PYTHIA
W+c	1126.0	1.52	ALPGEN	PYTHIA
W+cc	403.44	1.133	ALPGEN	PYTHIA
W+bb	133.99	1.133	ALPGEN	PYTHIA
Z+jets	2804.4	1.229	ALPGEN	HERWIG
diboson	17.075	1.7223	HERWIG	HERWIG

Table 5.2: Simulated background samples with associated cross-sections, k-factors, generating programs and showering programs.

based on the flavor associated jet. Multijets has a very high rate of occurrence and a very low acceptance making it very difficult to predict, so this analysis uses the matrix method to estimate this background from data.

5.2.1 W+jets normalization

The W+jets samples in this analysis are globally normalized using the charge asymmetry method in the region $m(W') < 330 \text{ GeV}$. This region has a signal contamination $< 5\%$ for all signal mass points considered in the analysis. This method normalizes the W+jets sample in each analysis channel using the theoretical asymmetry ratio $r_{MC} = \frac{W^+}{W^-}$ to account for the observed asymmetry in data. The ratio between the observed asymmetry and the expected asymmetry is applied as a normalization factor to the entire channel, as shown in Equation 5.2.

$$N_{W^+} + N_{W^-} = \frac{r_{MC} + 1}{r_{MC} - 1} (D^+ - D^-) \quad (5.2)$$

$N_{W^+} + N_{W^-}$ is the normalized W+jets yield and D^+ and D^- are the number of data events with positive and negative leptons respectively. The fraction of W+jets composed by W+lf, W+c, W+cc, and W+bb is determined by simultaneously varying the fraction of the total W+jets sample each sub-channel composes and fitting the MET distribution. For this fit the W+cc and W+bb samples are merged into a single W+hf sample and so they receive the same normalization factor. The normalization factors for each sample are given in Table 5.3.

Process	2jets 1tag	2jets 2tag	3jets 1tag	3jets 2tag
W+lf	0.941462	1.31867	0.883688	1.96718
W+c	0.801521	1.12266	0.752335	1.67477
W+cc	1.39795	1.95806	1.31217	2.92102
W+bb	1.39795	1.95806	1.31217	2.92102

Table 5.3: W+jets normalization factors.

5.2.2 Multijets estimate

The contribution of the multijet process to this analysis is estimated using the matrix method. The matrix method uses data events which have passed the event selection in Chapter 6 except with a loose lepton which has relaxed requirements compared to the tight lepton required for the signal region. Both the loose and tight lepton are defined in Chapter 4. For both electrons and muons

$$N^{loose} = N_{real}^{loose} + N_{fake}^{loose} \quad (5.3)$$

$$N^{tight} = \epsilon_{real} N_{real}^{loose} + \epsilon_{fake} N_{fake}^{loose} \quad (5.4)$$

where N is the number of data events containing a lepton of the indicated type. $\epsilon_{real} = \frac{N_{real}^{tight}}{N_{real}^{loose}}$ and $\epsilon_{fake} = \frac{N_{fake}^{tight}}{N_{fake}^{loose}}$ are the conversion efficiencies for loose leptons to tight leptons. ϵ_{real} is estimated using the tag and probe method on $Z \rightarrow ll$ events, while ϵ_{fake} is estimated using a multijets enhanced data sample where the lepton isolation criteria have been removed.

With the total number of events with loose and tight leptons known from the dataset, Equation 5.3 and Equation 5.4 can be inverted and combined with the fakes conversion efficiency to solve for N_{fake}^{tight} which is the multijets estimate for the analysis.

Chapter 6

Event selection

Before the final analysis described in Chapter 7 can be performed, an event selection specific to the signal kinematics is applied. This event selection is designed to remove background events while having minimal impact on the signal and defines the control regions used to perform the data-driven background estimates described in Section 5.2. Events are also separated into different channels by the event selection and these channels are individually optimized.

6.1 Composite objects

While Chapter 4 details how basic analysis objects are reconstructed from the raw detector response, Figure 6.1 shows several intermediate particles that can also be reconstructed. These intermediate states of the W boson, top quark, and ultimately the W' boson are what define this channel as unique from any other process with the same final state, such as Wbb . These intermediate particles also have unique kinematics that distinguish $W' \rightarrow t\bar{b}$ from other processes.

6.1.1 W boson and neutrino reconstruction

The W boson in Figure 6.1 is the only intermediate particle composed entirely of final state objects and its reconstruction is as simple as adding the 4-momenta of the lepton and

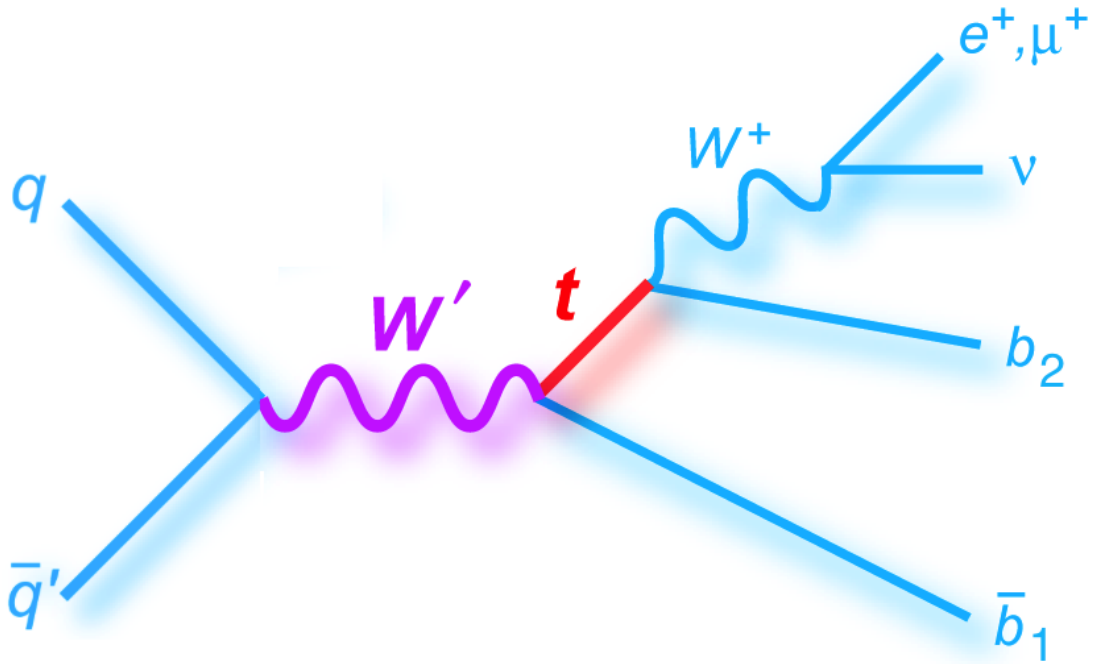


Figure 6.1: Illustration of the $W' \rightarrow t\bar{b}$ process.

neutrino together. The complication with this is that the 4-momentum of the neutrino is not known. Section 4.4 describes how the neutrino's p_T can be determined from the MET by assuming that the momentum is balanced in the transverse plane. This same technique cannot be used to determine p_z for the neutrino because there is no reason the interacting partons should have the same momentum along the beamline as each other. Instead the W boson and neutrino are defined simultaneously by requiring that the lepton (a single lepton selection is applied in Section 6.3) and neutrino combine to form an on-shell W boson with a mass of 80.4 GeV. Both the lepton and neutrino are assumed to be massless and the neutrino's p_T is assumed to be equivalent to the MET. This gives rise to a quadratic equation for the neutrino's p_z , with solutions given by Equation 6.1.

$$p_{z,\nu} = \frac{\mu p_{z,l}}{p_{T,l}^2} \pm \sqrt{\frac{\mu^2 p_{z,l}^2}{p_{T,l}^4} - \frac{E_l^2 p_{T,\nu}^2 - \mu^2}{p_{T,l}^2}} \quad (6.1)$$

$$\mu = \frac{M_W^2}{2} + \cos(\Delta\phi_{l,\nu}) p_{T,\nu} p_{T,l} \quad (6.2)$$

In Equation 6.3, $p_{T,l}$ and $p_{T,\nu}$ are the transverse momenta of the lepton and neutrino respectively, and $p_{z,l}$ and $p_{z,\nu}$ are the z-momenta of the lepton and neutrino. $\Delta\phi_{l,\nu}$ is the difference in ϕ between the lepton and neutrino. There are three possible categories of solution to Equation 6.1 based on the sign of the discriminant. If the discriminant is positive then there are two real solutions to Equation 6.1 and the solution with the lowest $|p_z|$ is chosen to define the neutrino, creating a less energetic final state. If the discriminant is 0 then there is only one p_z solution then the neutrino is uniquely defined. If the discriminant is negative then the solutions for p_z are imaginary, in this case the p_T of the neutrino is rescaled so that the discriminant becomes 0, then the neutrino p_z is uniquely defined and the neutrino p_T is taken to be the rescaled value.

6.1.2 Top quark reconstruction

While it is possible to reconstruct the top quark in Figure 6.1, there is an ambiguity about which jet originated from the top quark decay. The indeterminacy is resolved differently depending on which channel the event belongs to. If the event contains only 1 b-tagged jet then the invariant mass of each jet and the reconstructed W boson is calculated and the combination with a mass closest to the top quark mass of 172.5 GeV forms the reconstructed top quark. For events that contain 2 b-tagged jets the mass of the W boson and each b-tagged jet is calculated, with the pair producing a mass closest to 172.5 GeV forming the

top quark. The cut flow for each channel is described in greater detail in Section 6.3.

6.1.3 W' reconstruction

Similar to how the top quark is reconstructed, the W' boson is reconstructed differently depending on which analysis channel the event falls into. For events that contain 2 b-tagged jets the W' boson is reconstructed by combining the reconstructed top quark with the b-tagged jet that was not used to reconstruct the top quark. For events with 1 b-tagged jet the W' boson is reconstructed by combining the reconstructed top quark with the highest p_T jet not used to reconstruct the top quark, requiring that the b-tagged jet is included in the W' reconstruction. This means that for events where the b-tagged jet was included in the top quark reconstruction that the jet combined with the top quark is not b-tagged. For events where the top quark reconstruction does not include the b-tagged jet, the jet combined with the top quark to form the W' boson must be b-tagged.

6.2 Data triggers

In order for an event to be recorded by the ATLAS detector and included in an analysis it must pass the trigger selection described in Section 3.2.6. To search for $W' \rightarrow t\bar{b}$ the ATLAS single lepton triggers are used. The single electron triggers require that electrons either have an $E_T > 24$ GeV and pass medium isolation requirements for the hadronic leakage, shower width in η , and track isolation as described in Section 4.1 or have an $E_T > 60$ GeV without any isolation requirement. The single muon triggers require that muons either have a $p_T > 24$ GeV and pass medium isolation requirements for the ID track isolation described in Section 4.2 or have a $p_T > 36$ GeV without any isolation requirement. The complete set of

requirements for electrons and muons detailed in Chapter 4 is applied offline, after the data has been recorded. Events must also have been taken during an LHC stable beam period and during a time when all of the ATLAS subsystems were properly operating. The combination of these requirements corresponds to an integrated luminosity of 20.3 fb^{-1} .

6.3 Cut flow

Before performing the multivariate analysis described in Chapter 7, it is useful to apply a set of event selection cuts. These cuts are designed to remove background events with large kinematical differences from the signal samples so that the multivariate analysis can be more focused on discriminating between the hard to classify events. The event selection also defines the separate analysis channels which will undergo individually optimized multivariate analyses. The event selection cuts are as follows:

- Exactly 1 lepton.
- Lepton $p_T > 35 \text{ GeV}$.
- $\text{MET} > 35 \text{ GeV}$
- W boson transverse mass ($m_T(W)$) + MET $> 60 \text{ GeV}$, where $m_T(W)$ is defined in Equation 6.3.
- Exactly 2 or 3 jets.
- Exactly 1 or 2 b-tagged jets.
- W' boson mass ($m(W')$) $> 330 \text{ GeV}$.

$$m_T(W) = \sqrt{2p_{T,l}p_{T,\nu}(1 - \cos(\Delta\phi_{l,\nu}))} \quad (6.3)$$

The number of jets and the number of b-tagged jets defines a unique analysis channel which is referred to by the number of jets and b-tagged jets in events in that particular channel, for example the 2jets 1tag channel contains events with exactly 2 jets and exactly 1 b-tagged jet. This produces four separate analysis channels, 2jets 1tag, 2jets 2tag, 3jets 1tag, and 3jets 2tag.

The cuts on the lepton number, lepton p_T , and MET are chosen to match the decay channel seen in Figure 6.1 where we expect a single high p_T lepton and large MET from the W boson decay. The cut on $m_T(W) + \text{MET}$ is called the triangular cut and is commonly used in single top analyses to discriminate against the multijets background. The cut on $m(W')$ is chosen to define a control region used to perform a data driven normalization of the W+jets background as described in Section 5.2.1. The cut value of 330 GeV was chosen to maximize the size of the control region while keeping the signal contamination to less than 5% for all of the signal samples.

Both of the 1tag channels have significantly larger backgrounds than the 2tag channels so two additional cuts are applied to the 1tag channels only:

- E_T of the leading jet ($E_T(\text{jet1}) > 140$ GeV).
- Transverse energy of the reconstructed top quark ($E_T(\text{Top}) > 175$ GeV).

These cuts are chosen by ranking a list of event kinematics variables by their discrimination power after performing the initial event selection cuts. The discrimination power of each variable is determined by mapping the signal efficiency (ϵ_S) versus the background efficiency

(ϵ_B) for successively raised cuts on the variable. The area between the curve this process maps out and the line of $\epsilon_S = \epsilon_B$ is defined to be the discrimination power of the variable. For the two most discriminating variables, $p_T(jet1)$ and $E_T(Top)$, the cut is chosen to be at least 95% efficient for all signal samples. The final event yields are shown in Table 6.1.

Sample	2jets 1tag	3jets 1tag	2jets 2tag	3jets 2tag
$W'_R 500$	12601.14	5599.62	8874.10	5120.80
$W'_R 750$	4018.08	2723.38	2468.55	2172.28
$W'_R 1000$	1117.67	937.33	606.33	657.60
$W'_R 1250$	337.63	311.93	155.44	189.40
$W'_R 1500$	101.52	107.72	41.97	57.29
$W'_R 1750$	32.09	36.60	12.11	18.28
$W'_R 2000$	11.07	13.18	4.12	6.20
$W'_R 2250$	4.09	5.01	1.48	2.06
$W'_R 2500$	1.71	1.94	0.63	0.84
$W'_R 2750$	0.80	0.86	0.34	0.40
$W'_R 3000$	0.42	0.42	0.19	0.22
$W'_L 500$	6680.34	3078.17	5235.86	3129.40
$W'_L 750$	2307.41	1551.99	1556.07	1310.33
$W'_L 1000$	681.85	577.36	411.47	438.10
$W'_L 1250$	229.29	213.66	112.84	138.45
$W'_L 1500$	75.38	77.88	32.26	44.19
$W'_L 1750$	25.97	30.55	10.65	14.45
$W'_L 2000$	9.75	11.16	3.43	4.99
$W'_L 2250$	3.81	4.55	1.37	1.98
$W'_L 2500$	1.65	1.89	0.60	0.78
$W'_L 2750$	0.73	0.82	0.30	0.40
$W'_L 3000$	0.40	0.41	0.18	0.21
single top s-channel	138.10	73.92	98.82	58.71
single top t-channel	1957.69	1080.64	242.73	373.00
single top Wt-channel	624.74	979.43	80.10	270.67
$t\bar{t}$	4586.93	9410.07	1480.34	5108.30
W+lf	2950.59	1255.28	45.78	45.27
W+c	4877.90	1989.33	78.18	71.61
W+cc	3471.35	2470.32	81.00	127.04
W+bb	3395.41	2086.27	455.80	675.72
Z+jets	361.64	379.02	2.32	9.45
diboson	214.10	119.48	16.34	15.36
multiplets	1132.34	540.02	59.54	58.68
total background	23710.80	20383.78	2640.95	6813.83
data	21106.00	18317.00	2632.00	6666.00

Table 6.1: Event yields for signal samples, background samples, and data by analysis channel.

Chapter 7

Multivariate analysis

The event selection described in Chapter 6 does not sufficiently optimize the statistical significance of a potential signal in each of the analysis channels. The method used to optimize the significance in this analysis is a boosted decision tree (BDT) multivariate analysis (MVA). The details of the BDT algorithm are discussed in Section 7.1, but the basic premise is that events are sorted into background-like and signal-like bins using a series of cuts called a decision tree. This decision tree optimizes the separation of signal and background events at each node by placing a cut on a single variable, with both output possibilities forming a new decision node iteratively until the specified end conditions are met. Misclassified events, that is signal events in a background-like bin or background events in a signal-like bin, have their relative weight "boosted" and a new decision tree is trained. This training and boosting process is iterated many times and all of the decision trees combined form the BDT. This boosting serves to increase the importance of hard to classify events and make them more likely to be correctly categorized in subsequent decision trees. A final decision weight is assigned to each event based on the aggregate purity of the bins it was sorted into in each decision tree, which represents how signal-like or background-like each event is. This iterative process allows for a more nuanced handling of variable correlations than a simple cuts based analysis which is effectively a single decision tree. The BDT also has the convenient property that it condenses the discrimination power from many variables into a single highly discriminating weight which is more easily understood by the human analyst.

7.1 Boosted decision trees

The boosted decision tree (BDT) algorithm [48] is designed to optimize the discrimination between signal and background events. The implementation of the BDT algorithm used in this analysis is done by the Toolkit for Multivariate Data Analysis with ROOT (TMVA) [49] and while the principles of the analysis are general to all BDTs, the details are specific to this software package. Each of the analysis channels (2jets 1tag, 2jets 2tag, 3jets 1tag, and 3jets 2tag) has an independent BDT trained with the variables for each channel described in Section 7.1.2, and the BDT settings for each channel are described in Section 7.1.3.

The BDT training begins with a sample of signal events and background events, with each event having a weight equal to its contribution to the overall normalization and a set of kinematic variables defined to be used in the BDT. An optimal cut on one of these variables is determined by maximizing ΔG as defined in Equation 7.1 for all possible cuts on these variables where $G_{pre-cut}$ is calculated for all of the events and $G_{passed\ cut}$ and $G_{failed\ cut}$ are calculated for the events which pass and fail the cut respectively.

$$\Delta G = G_{pre-cut} - G_{passed\ cut} - G_{failed\ cut} \quad (7.1)$$

$$G = \sum_{events} WP(1 - P) \quad (7.2)$$

In Equation 7.2 G is called the Gini index, W is the event weight, and P is the purity which is fraction of events belonging to the signal. With the optimal separation cut defined all of the events are sorted into two bins: events that pass the cut, and events that fail the cut. The process of finding the optimal cut and sorting the events based on that cut forms a

decision node.

Each of the two output bins from the first decision node then form their own decision nodes to be applied to only those events. A new optimal cut is determined for each of these nodes and the events are sorted into four bins (two for each decision node). This process is continued iteratively, further subdividing the sample into more bins at each iteration, until a termination condition is met. A minimum number of events is required to be in a bin in order for that bin to become a new decision node, and there is a maximum depth in the decision tree for a node to become a decision node. The initial decision node is at a depth of 1, the bins output from that decision node are at a depth of 2, and so on. Any bins that do not form decision nodes instead form termination nodes and are defined as signal or background nodes based on the majority of events in that termination node. The decision and termination nodes together form a decision tree, an example of which is given in Figure 7.1.

While a single decision tree can provide some discrimination power between signal and background events, the discrimination power can generally be increased by training multiple decision trees and increasing the weight of events misclassified as either signal or background by each tree. A misclassified event is a signal event that is sorted into a background termination node or a background event that is sorted into a signal termination node, and this analysis uses the Adaboost algorithm to increase the weight of such events when training subsequent decision trees. The new weight of a misclassified event is given by $w_{boosted}$ in Equation 7.3, where β is the boosting strength and is one of the parameters optimized in Section 7.1.3 and $w_{pre-boosted}$ is the event weight before being boosted.

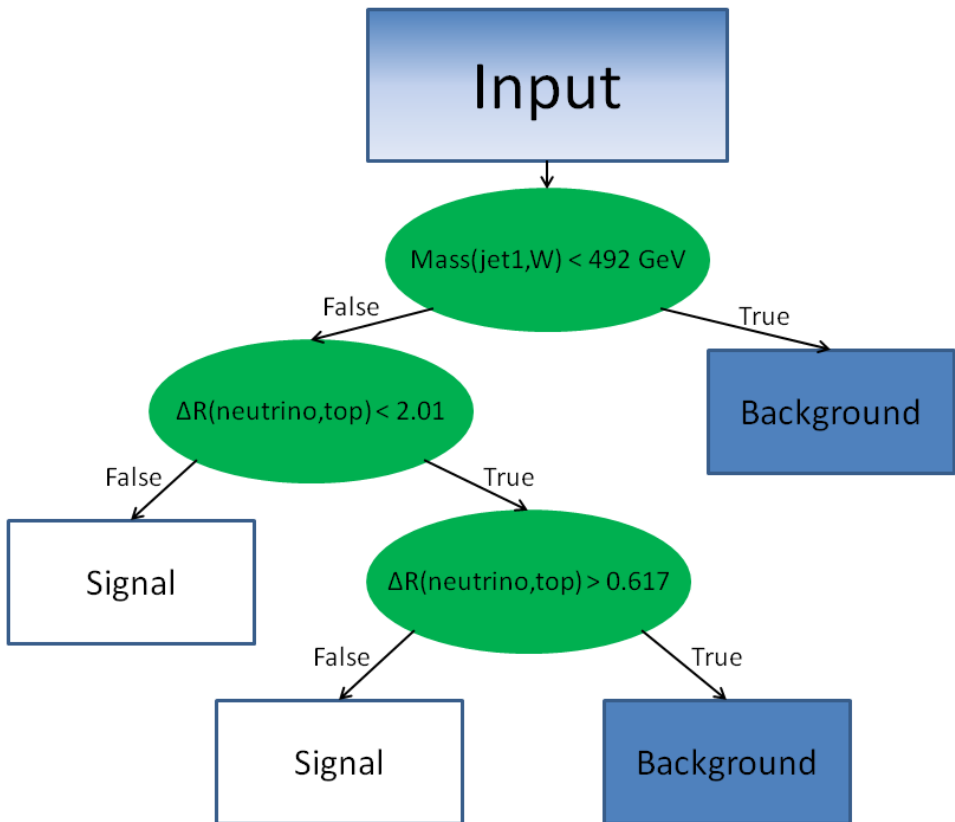


Figure 7.1: An example decision tree which sorts input events into signal and background bins. The variables used in the decision tree are described in Section 7.1.2

$$w_{boosted} = \left(\frac{1 - err}{err} \right)^\beta w_{pre-boosted} \quad (7.3)$$

$$err = \frac{\text{sum of misclassified event weights}}{\text{sum of all event weights}} \quad (7.4)$$

After the misclassified events have their weights boosted, all events have their weights scaled to keep the total sum of events weights normalized and a new decision tree can be trained. The total number of decision trees trained is one of the parameters optimized in Section 7.1.3.

With each event being sorted by multiple decision trees, an aggregate BDT decision weight (y_{Boost}) is formed by taking a weighted average of the individual decision tree responses as given by Equation 7.5.

$$y_{Boost} = \frac{1}{N_{Trees}} \sum_{i=1}^{N_{Trees}} \ln \left(\frac{1 - err_i}{err_i} \right) h_i \quad (7.5)$$

For Equation 7.5, N_{Trees} is the total number of decision trees trained and err_i is given by Equation 7.4 for each tree. The result of each tree for the event is represented by h_i , which is $+1$ or -1 if the event was sorted into a signal or background termination node by that tree. Thus the final BDT decision weight for each event is a value between -1 and $+1$, where -1 represents an ideal background event and $+1$ represents an ideal signal event.

7.1.1 Overtraining

If the BDT has too many degrees of freedom compared to the statistical size of the generated samples during training then the BDT begins to optimize the decision trees based on the specific variable values of individual events rather than on the overall distributions. This is

called overtraining and it causes the BDT output to be drastically different if the trained BDT is applied to a new sample simulated under identical conditions. In order to check if a BDT is overtrained all of the event samples are split in half before training. One half, called the training sample, is used to train the BDT and is run through the resulting BDT to compute the BDT decision weight distribution. The remaining half of the events, called the testing sample, is run through the already trained BDT and produces an independant BDT decision weight distribution. The training and testing distributions for both the signal and background samples should be similar if the BDT is not overtrained, and they are compared using a Kolmgorov-Smirnov (KS) test [50]. The KS test provides a probability that two samples come from the same distribution, and if the KS result is < 0.5 for either the signal or background distributions then the BDT is determined to be overtrained.

7.1.2 Variable selection

The variables that are used in the BDT to separate the signal and background events has a large impact on the separation power of the BDT. Variables should be chosen that can discriminate between signal and background events, where the discrimination power is defined the same as in Section 6.3. Because the correlations between several different variables are not always obvious for all of the different processes included in the signal and background samples, the analysis begins with a large list of variables in an attempt to be as comprehensive as possible. For each sample the analysis objects, as defined in Chapter 4, are the lepton (lep), reconstructed neutrino (neutrino), reconstructed W boson (W), reconstructed top quark (top), reconstructed W' boson (W'), the leading jet (jet1), the sub-leading jet (jet2), the leading b-tagged jet (bjet1), and in the appropriate analysis channels the third jet (jet3) and sub-leading b-tagged jet (bjet2). For each of these objects the energy, mass,

pseudorapidity, azimuthal angle, transverse momentum, and transverse energy are considered as possible variables for inclusion in the BDT. In addition a set of two body variables is included in this list which consists of the mass, difference in pseudorapidity ($\Delta\eta$), difference in azimuthal angle ($\Delta\phi$), and opening angle (ΔR) for every pair of analysis objects. A final set of global event variables consisting of the MET, the azimuthal angle of the MET ($\phi(MET)$), the total sum of the transverse energy in the event (Sum E_T), the total sum of the transverse energy of the analysis object in the event (H_T), the aplanarity of the event (a measure of how much of the energy in the event resides in one plane), and the sphericity of the event (a measure of how evenly the energy of an event is distributed around the interaction point). This forms an initial list of approximately 200 variables depending on the analysis channel, however past experience in the single-top analyses suggests that fewer than 20 variables are necessary for a BDT to achieve good separation of signal and background events. In order to remove unnecessary variables, variables with a discrimination power $< 20\%$ are removed from the list for each channel which leaves approximately 50 variables for each channel. It is important that these variables be well modeled so the background distributions are compared to the data and any variables with a KS value < 0.5 are removed. A BDT is then trained using the remaining variables and the variables are ranked by importance, which is how frequently they are used in the individual decision trees. The five least important variables are removed from the variable list and the process is repeated until only 20 variables remain. At this point the training and variable removal iterations continue but only a single variable is removed in each iteration until the removal of a variable would cause the separation power of the BDT to degrade to $< 90\%$ of the maximum value obtained during these iterations. Table 7.1 lists the final variables for each of the analysis channels in order of importance, and Figures 7.2-7.14 show the data-Monte Carlo comparison plots for

2jets 1tag	3jets 1tag	2jets 2tag	3jets 2tag
$p_T(\text{top})$	mass(jet1,W)	mass(W')	mass(W')
mass(W')	H_T	$\Delta R(\text{lepton},\text{top})$	sphericity
$E(W')$	mass(W')	aplanarity	$p_T(\text{top})$
mass(jet1,jet2)	mass(jet1,jet2)	H_T	$\Delta\eta(\text{lepton},W)$
$\Delta\eta(\text{lepton},W)$	MET	$p_T(\text{bjet1})$	$E_T(\text{bjet1})$
Sum E_T	$\Delta R(\text{neutrino},\text{top})$	$p_T(\text{bjet2})$	$\Delta R(\text{bjet1},\text{top})$
mass(jet1,W)	$E(\text{lepton})$	mass(bjet1,bjet2)	$\Delta R(\text{lepton},\text{bjet1})$
$\Delta R(\text{lepton},\text{top})$	$p_T(\text{top})$	$E_T(W)$	$\Delta\phi(W,\text{top})$
mass(lepton,jet1)	$p_T(W)$	$\Delta R(\text{lepton},\text{bjet2})$	$\Delta\eta(\text{lepton},\text{top})$
$\Delta\eta(\text{neutrino},\text{top})$	$E(W')$	$\Delta R(\text{bjet1},\text{bjet2})$	mass(lepton,bjet1)
$E_T(\text{lepton})$	$\Delta\eta(\text{lepton},W)$	$\Delta R(\text{lepton},W)$	$\Delta R(\text{bjet1},W)$
$p_T(W)$	mass(lepton,jet1)	$p_T(\text{top})$	$p_T(\text{lepton})$
H_T	$\Delta R(\text{lepton},\text{top})$	sphericity	aplanarity
MET	mass(jet1,top)	$p_T(\text{lepton})$	
$\Delta\eta(\text{neutrino},\text{jet2})$	$\Delta\eta(\text{neutrino},W)$		
$\Delta R(\text{jet2},W)$			
$\Delta R(\text{lepton},\text{jet2})$			
mass(jet1,top)			

Table 7.1: Boosted decision tree variable lists for the four analysis channels. Variables are ranked by importance.

these variables.

7.1.3 BDT parameter optimization

The BDT parameters are the specific values used in the BDT training algorithm described in Section 7.1. These values have a strong impact on the resulting BDT and have a complicated relationship with the variables chosen for the BDT as well as any possible overtraining of the BDT. Because of this it is important to optimize these values but this is not a straight forward process. For each value of these parameters to be tested a new BDT must be trained which makes it computationally impractical to optimize the parameters simultaneous with the variable selection. Instead an iterative approach is taken, with each parameter value

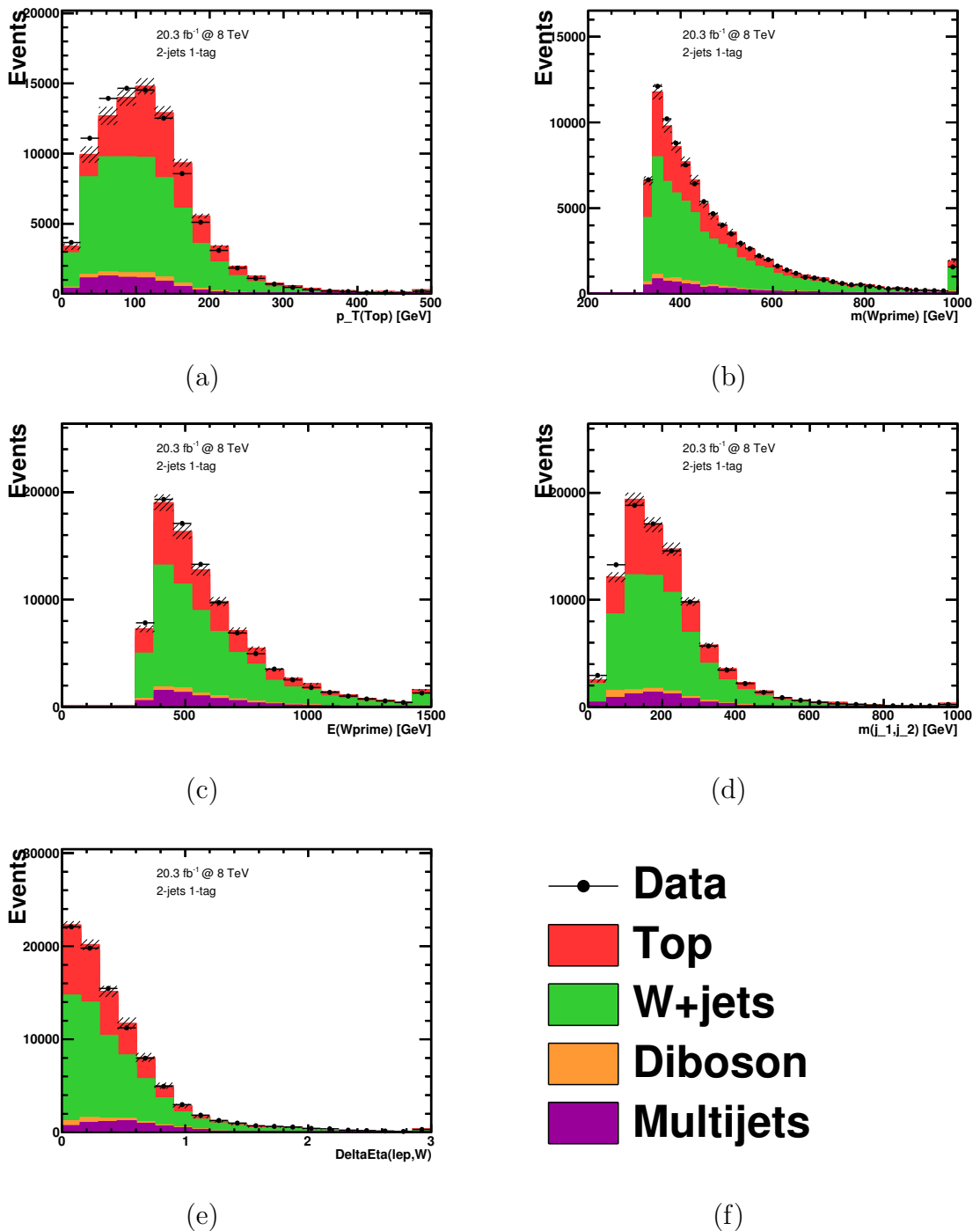


Figure 7.2: Comparison of data to Monte Carlo prediction of the 1st-5th variables by importance in the 2jet 1tag BDT

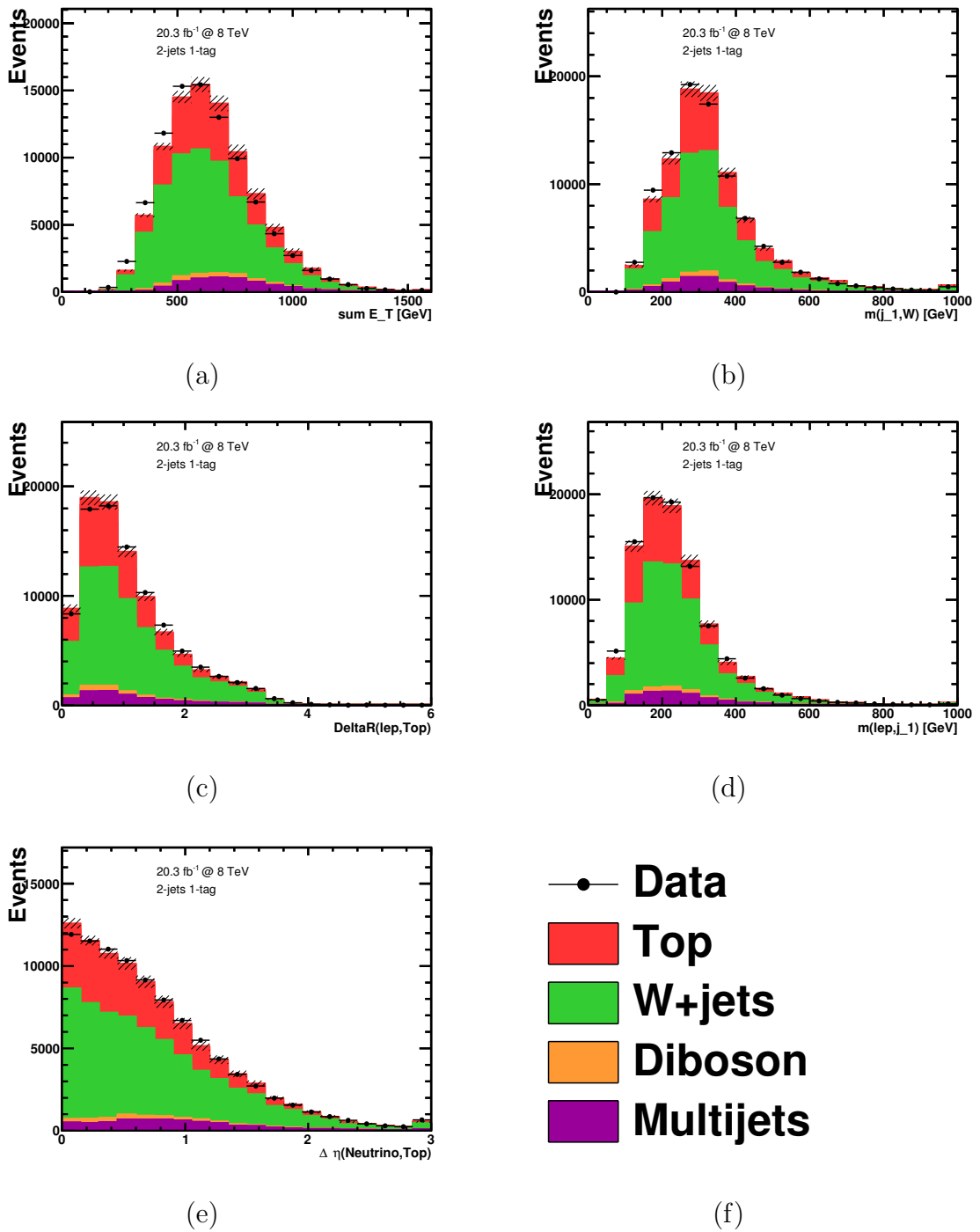


Figure 7.3: Comparison of data to Monte Carlo prediction of the 6th-10th variables by importance in the 2jet 1tag BDT

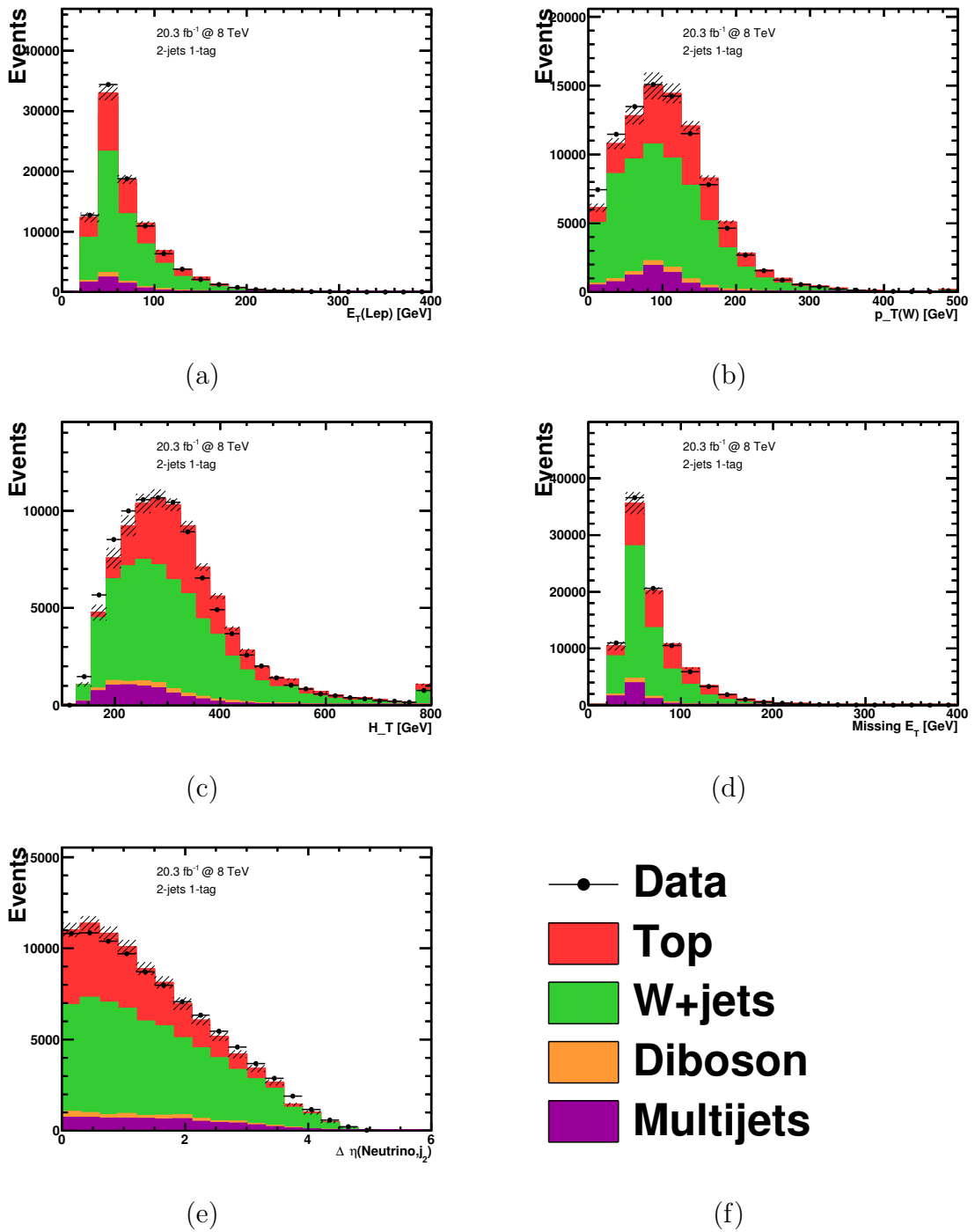


Figure 7.4: Comparison of data to Monte Carlo prediction of the 11th-15th variables by importance in the 2jet 1tag BDT

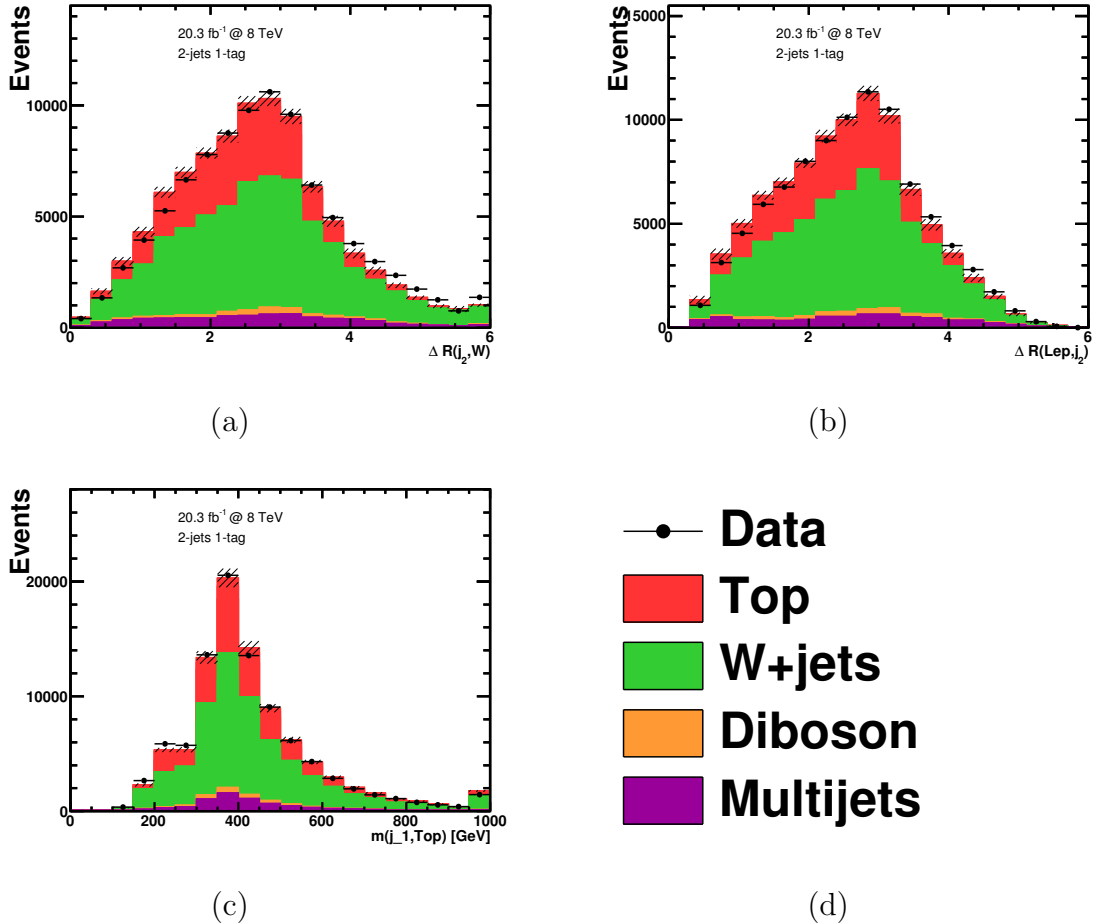


Figure 7.5: Comparison of data to Monte Carlo prediction of the 16th-18th variables by importance in the 2jet 1tag BDT

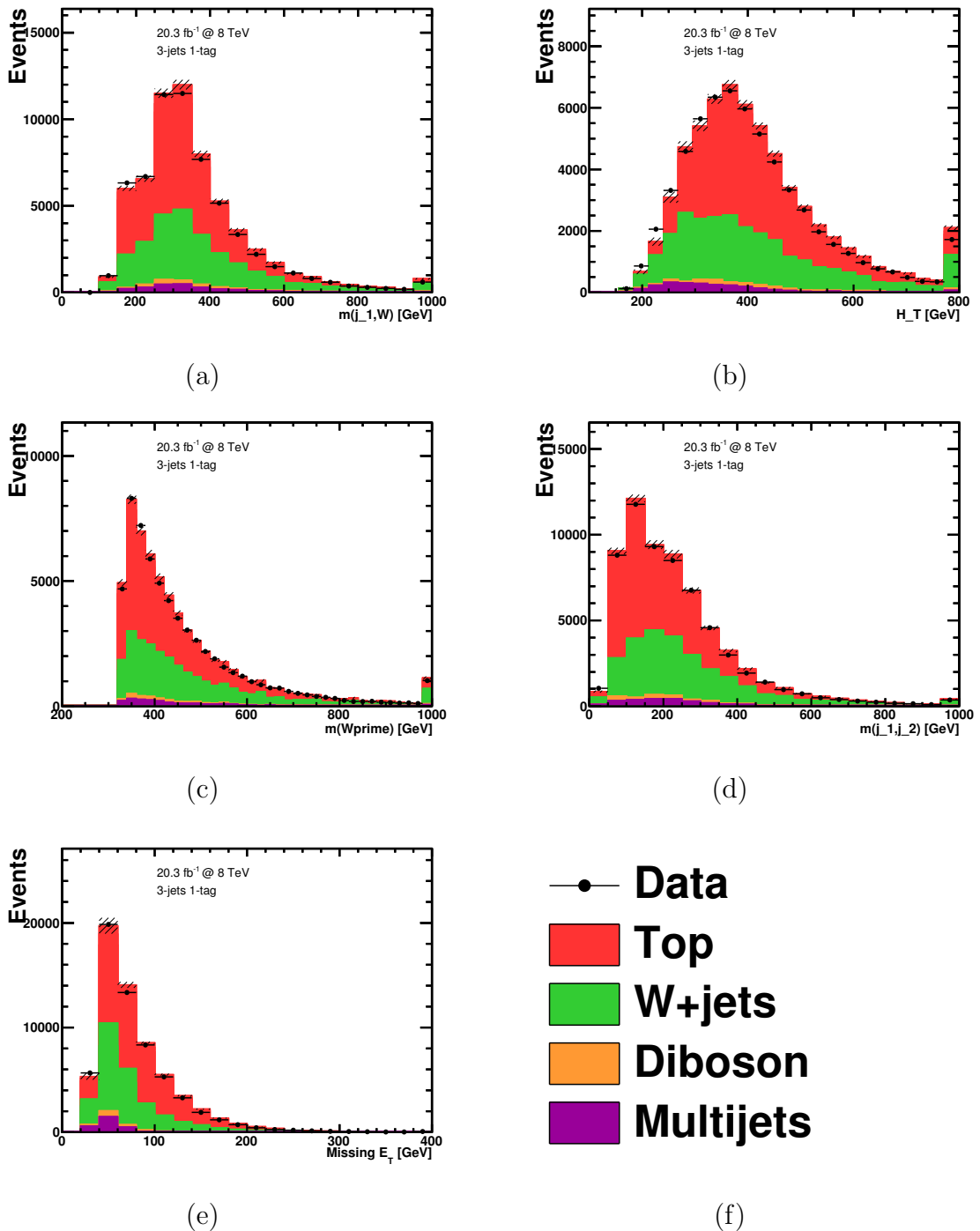


Figure 7.6: Comparison of data to Monte Carlo prediction of the 1st-5th variables by importance in the 3jet 1tag BDT

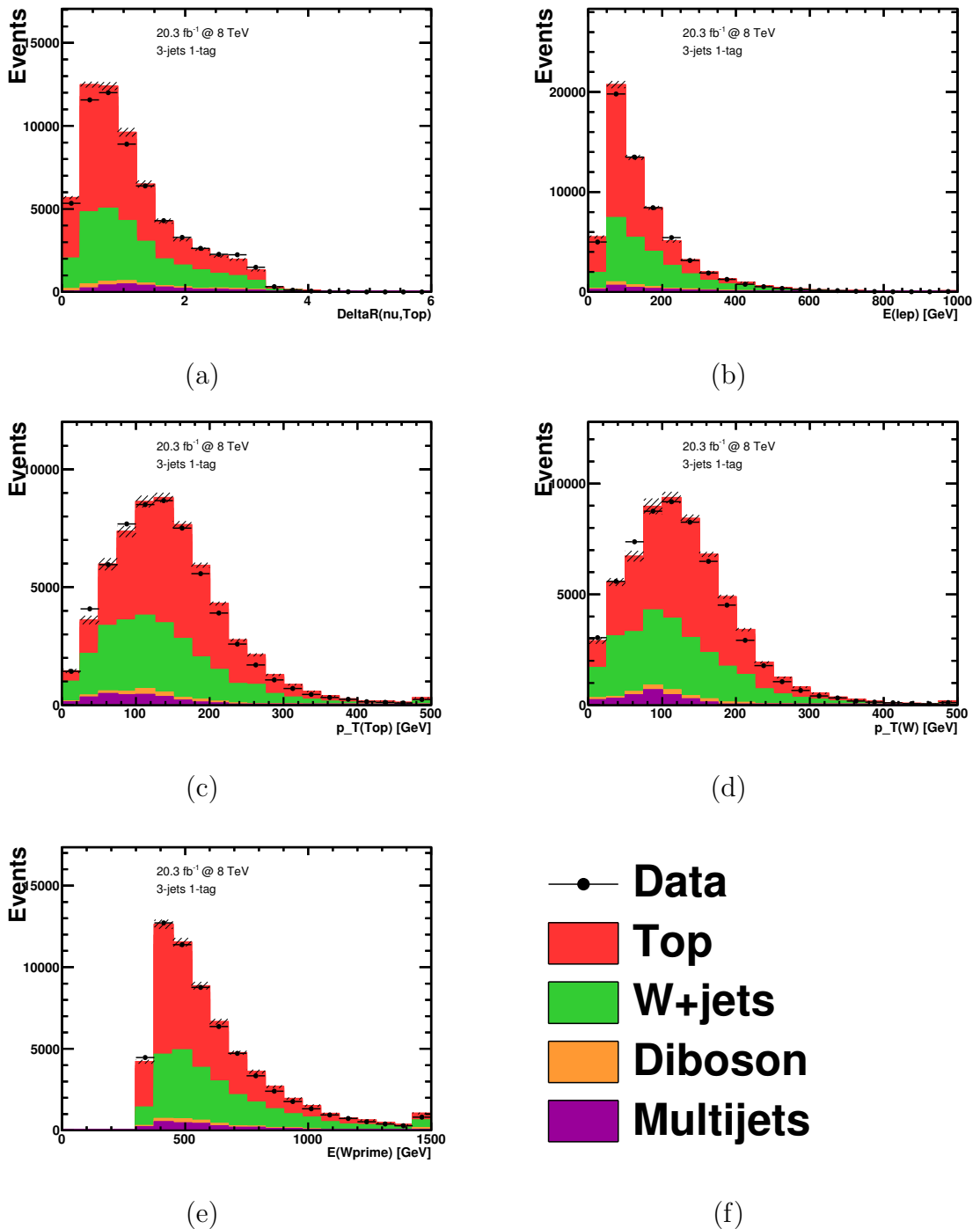


Figure 7.7: Comparison of data to Monte Carlo prediction of the 6th-10th variables by importance in the 3jet 1tag BDT

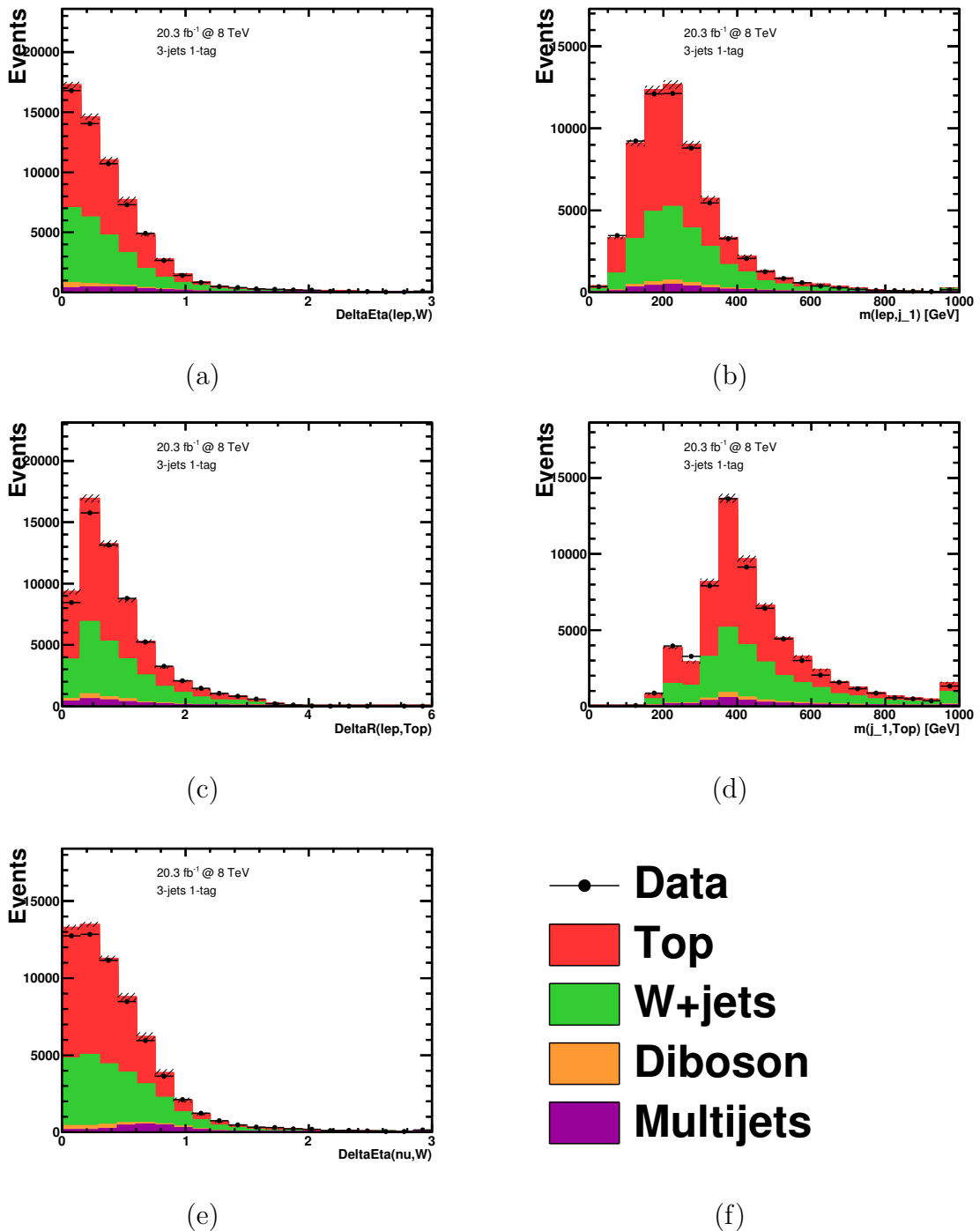


Figure 7.8: Comparison of data to Monte Carlo prediction of the 11th-15th variables by importance in the 3jet 1tag BDT

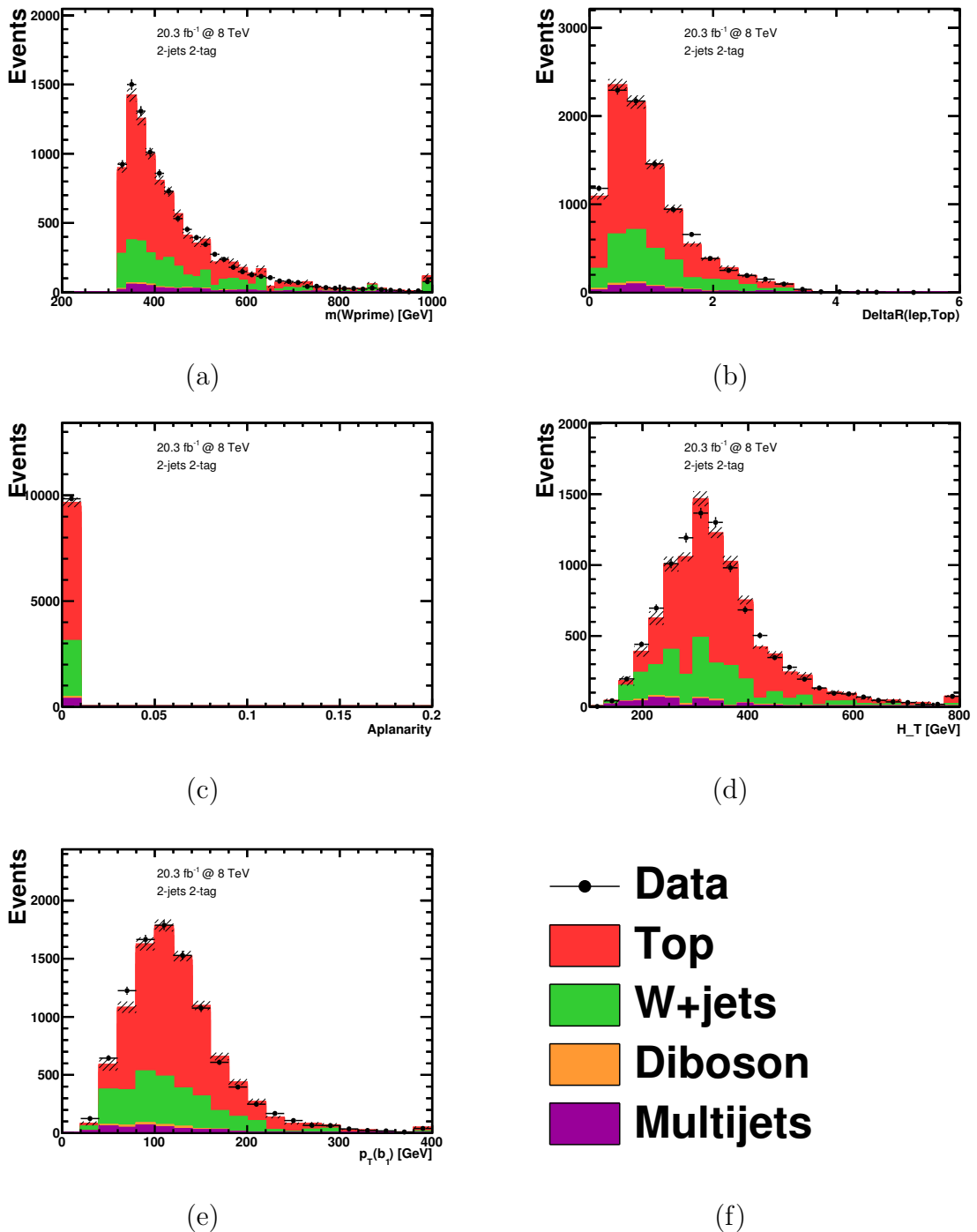


Figure 7.9: Comparison of data to Monte Carlo prediction of the 1st-5th variables by importance in the 2jet 2tag BDT

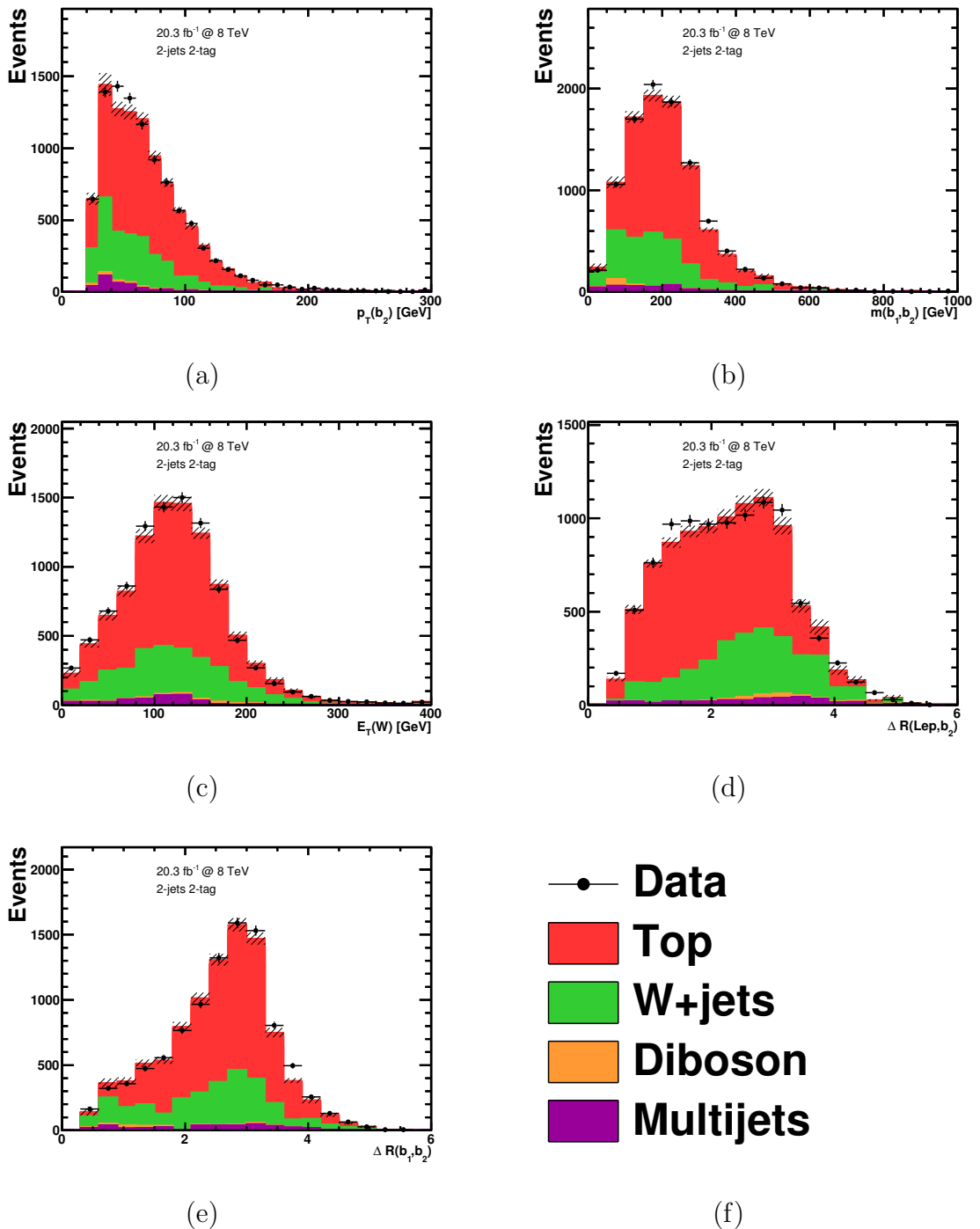


Figure 7.10: Comparison of data to Monte Carlo prediction of the 6th-10th variables by importance in the 2jet 2tag BDT

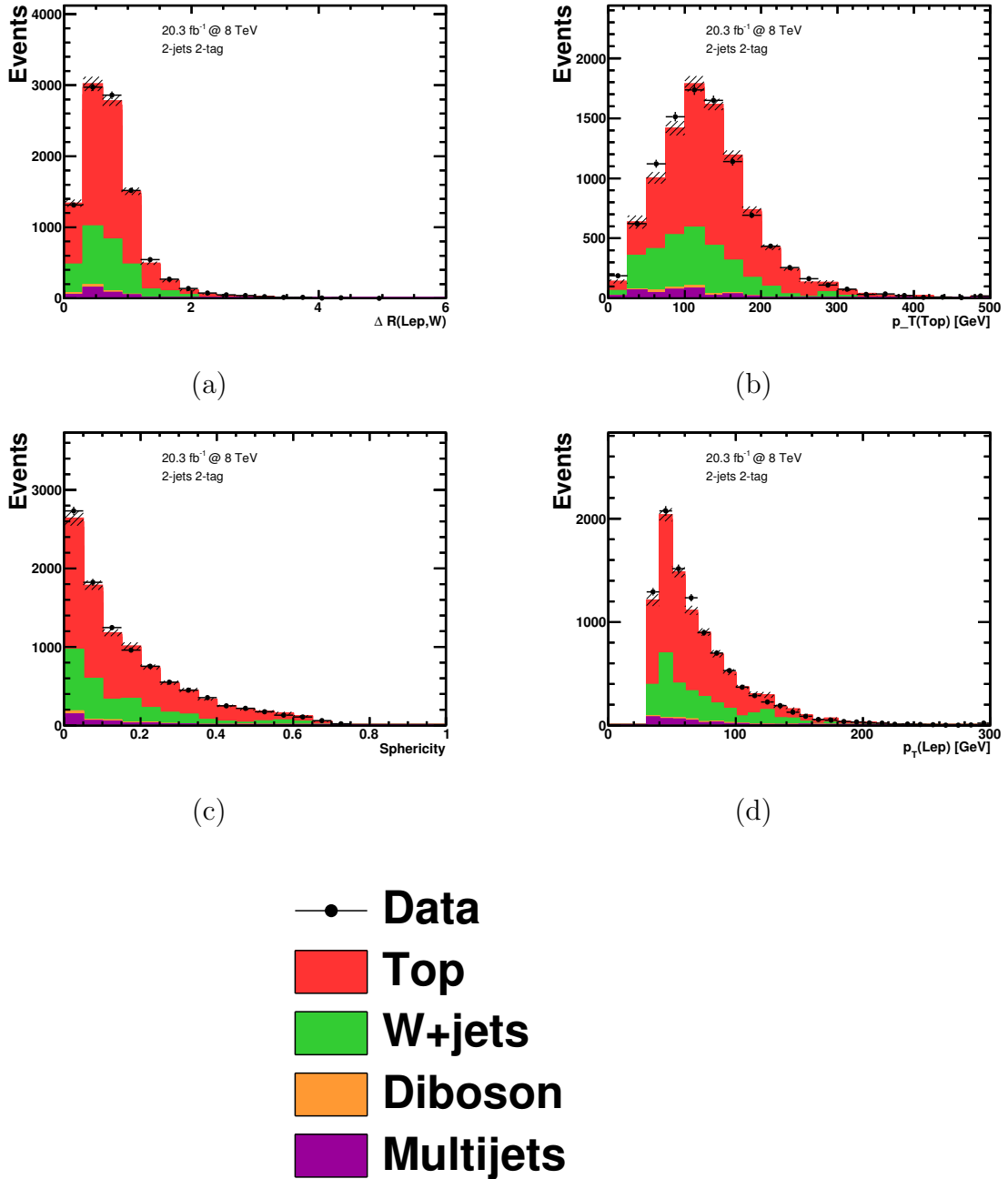


Figure 7.11: Comparison of data to Monte Carlo prediction of the 11th-14th variables by importance in the 2jet 2tag BDT

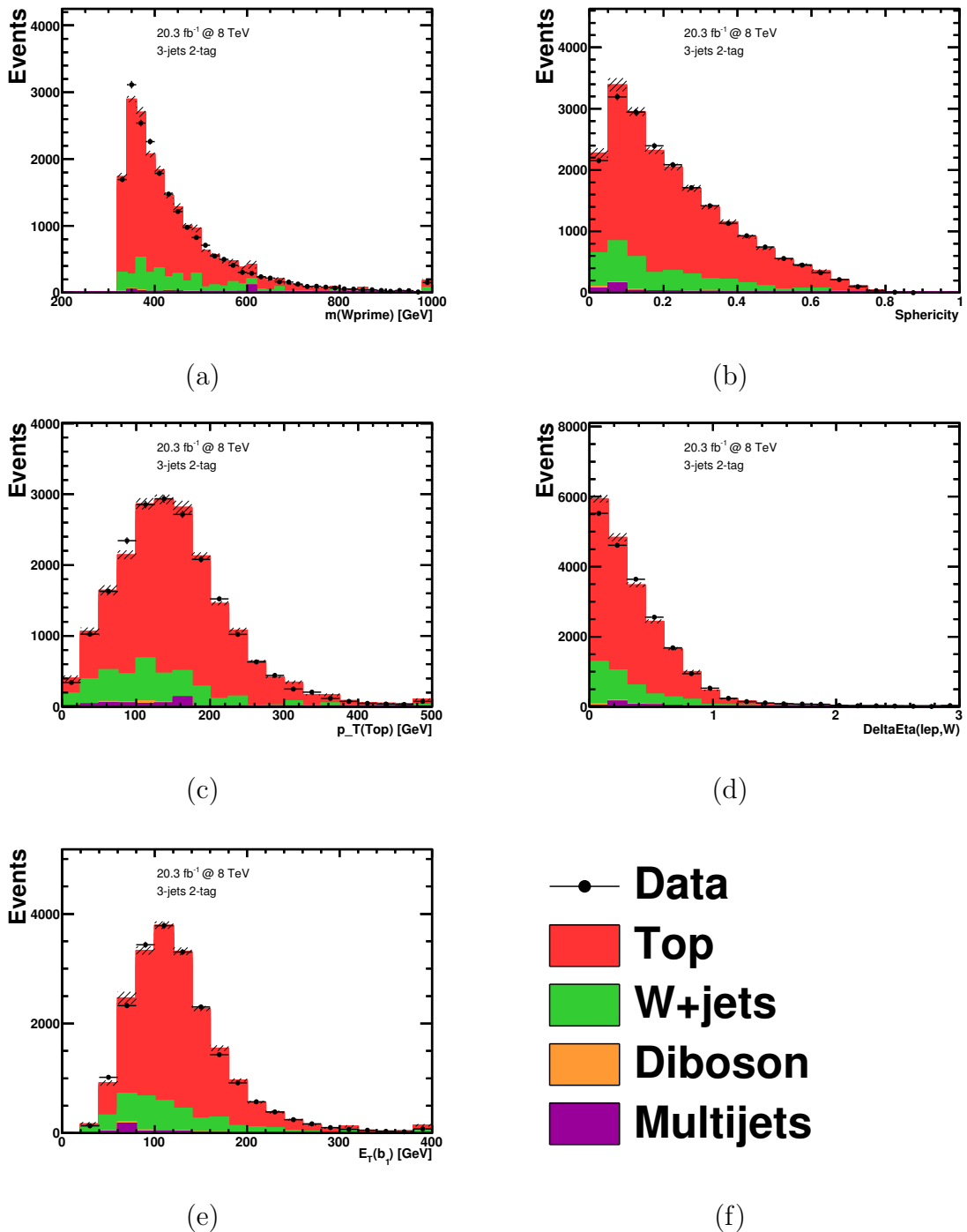


Figure 7.12: Comparison of data to Monte Carlo prediction of the 1st-5th variables by importance in the 3jet 2tag BDT

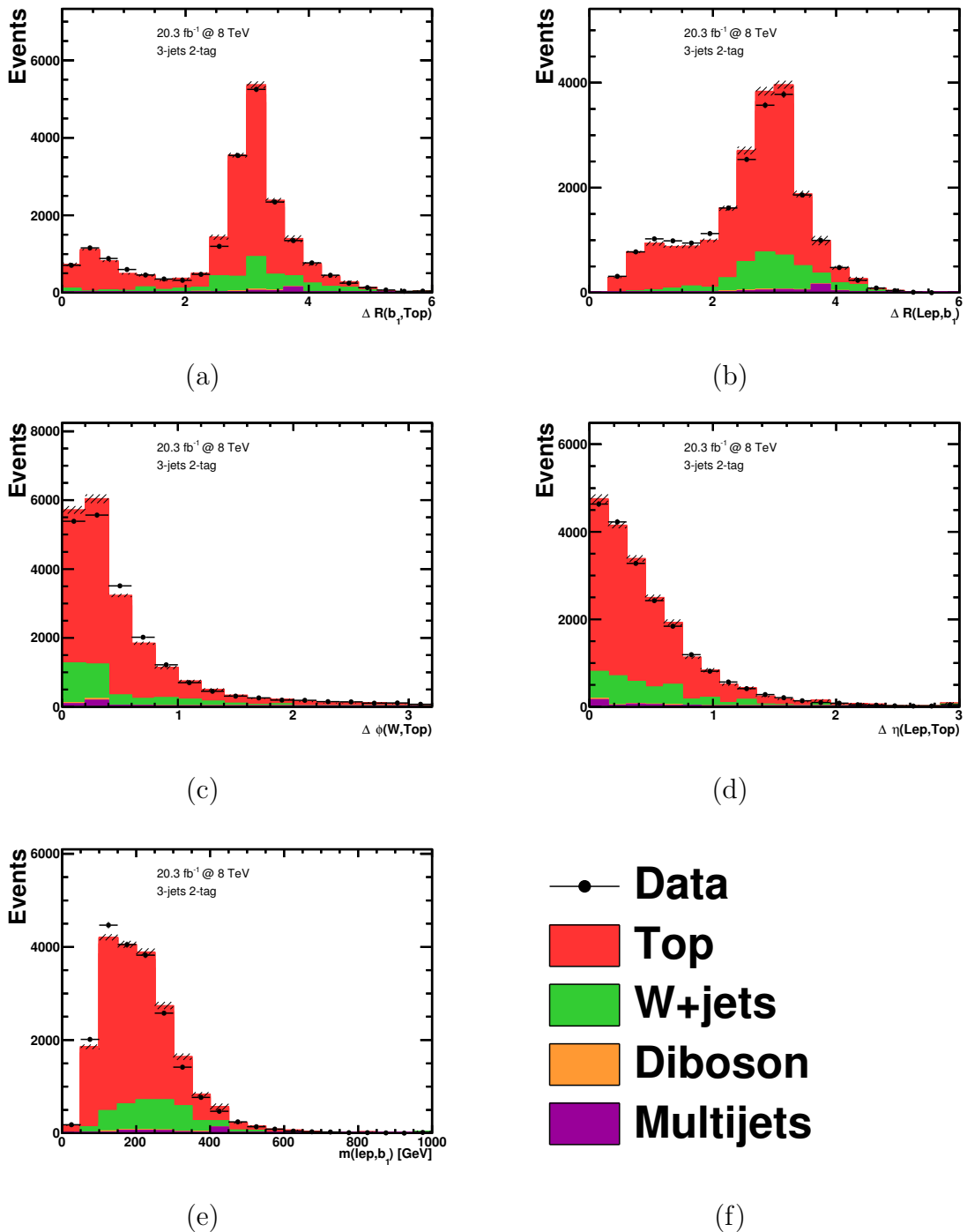


Figure 7.13: Comparison of data to Monte Carlo prediction of the 6th-10th variables by importance in the 3jet 2tag BDT

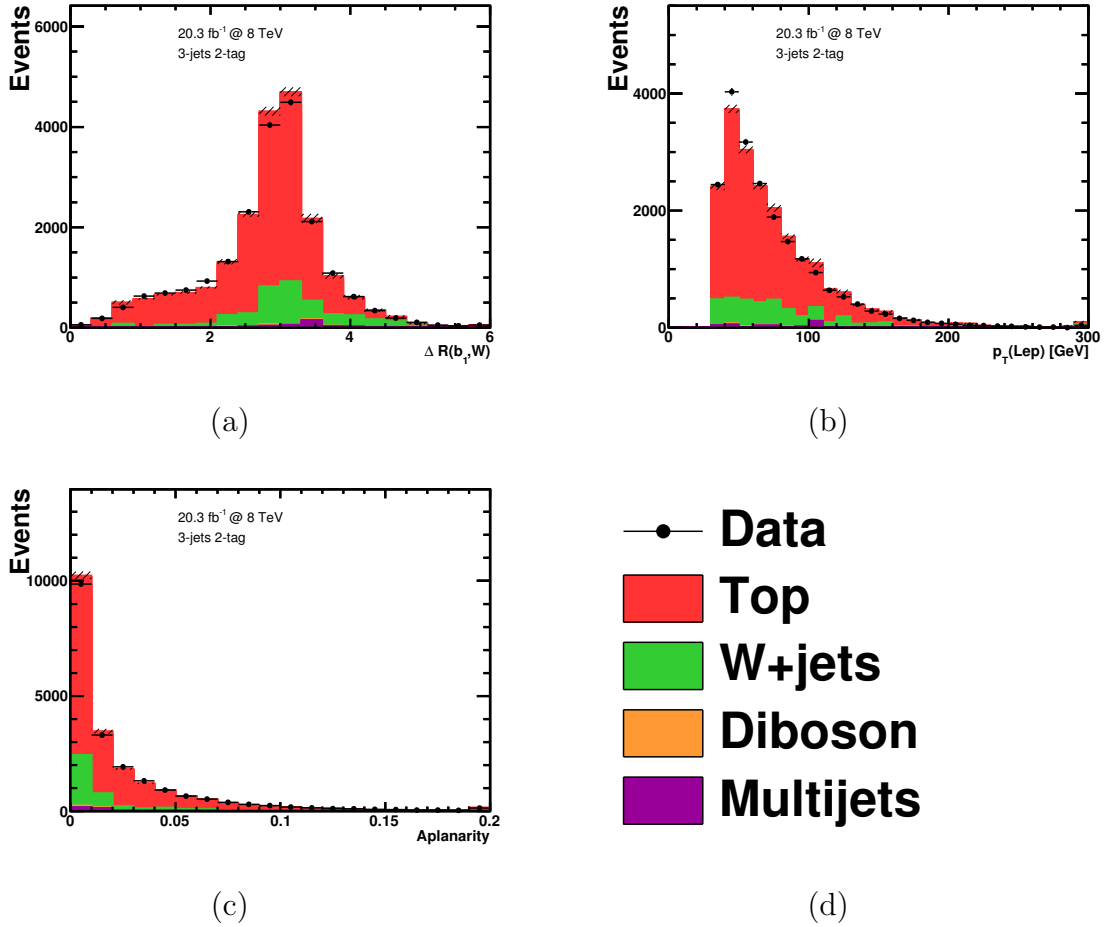


Figure 7.14: Comparison of data to Monte Carlo prediction of the 11th-13th variables by importance in the 3jet 2tag BDT

being optimized individually by scanning a range of values in discrete steps after the variable selection has been performed. An optimal parameter is chosen based on the BDT separation power after any overtrained trees have been removed. The variable selection and subsequent BDT parameter optimization are then redone if any parameter value changed by more than one step during the optimization. While it is possible for this method to get stuck in local optimizations, it has produced stable results with the available computational resources. A description of the parameters is provided below in the order they are optimized along with the initial training value of each parameter and the range and step size of the optimization scan. The final value of these parameters is provided in Table 7.2.

- **nTrees** is the number of individual decision trees to be trained by the BDT. This affects both the performance and possible overtraining of the BDT by allowing more degrees of freedom in the optimization. The range 60-200 is scanned with a step size of 20 and a default value of 120.
- **nEventsMin** is the minimum number of events for a decision node to be formed instead of a termination node. This affects the BDT performance and any possible overtraining by limiting how complex the individual decision trees can become. The range 100-300 is scanned with a step size of 20 and a default value of 200.
- **maxDepth** is the maximum decision depth of each decision tree in the BDT. Similar to nEventsMin, this affects the BDT performance and any possible overtraining by limiting how complex the individual decision trees can become. The range 6-12 is scanned with a step size of 1 and a default value of 9.
- **AdaBoost** is the boosting strength β in Equation 7.3. This primarily affects the performance of the BDT by adjusting how important the hard to classify events are.

Parameter	2jets 1tag	3jets 1tag	2jets 2tag	3jets 2tag
nTrees	160	100	100	100
nEventsMin	200	200	180	200
maxDepth	10	10	8	8
AdaBoost	0.7	0.7	0.5	0.7
nCuts	10	12	14	12

Table 7.2: Optimized Boosted decision tree parameters for each of the four analysis channels.

The range 0.4-1.0 is scanned with a step size of 0.1 and a default value of 0.7.

- **nCuts** is how many possible cuts are tested for each variable when determining the optimal cut for a decision node. This affects the BDT performance by ensuring the decision nodes have adequate granularity in their optimization. The range 8-16 is scanned with a step size of 2 and a default value of 12.

7.1.4 BDT output distributions

The BDT output distributions for the four analysis channels are shown in Figure 7.15.

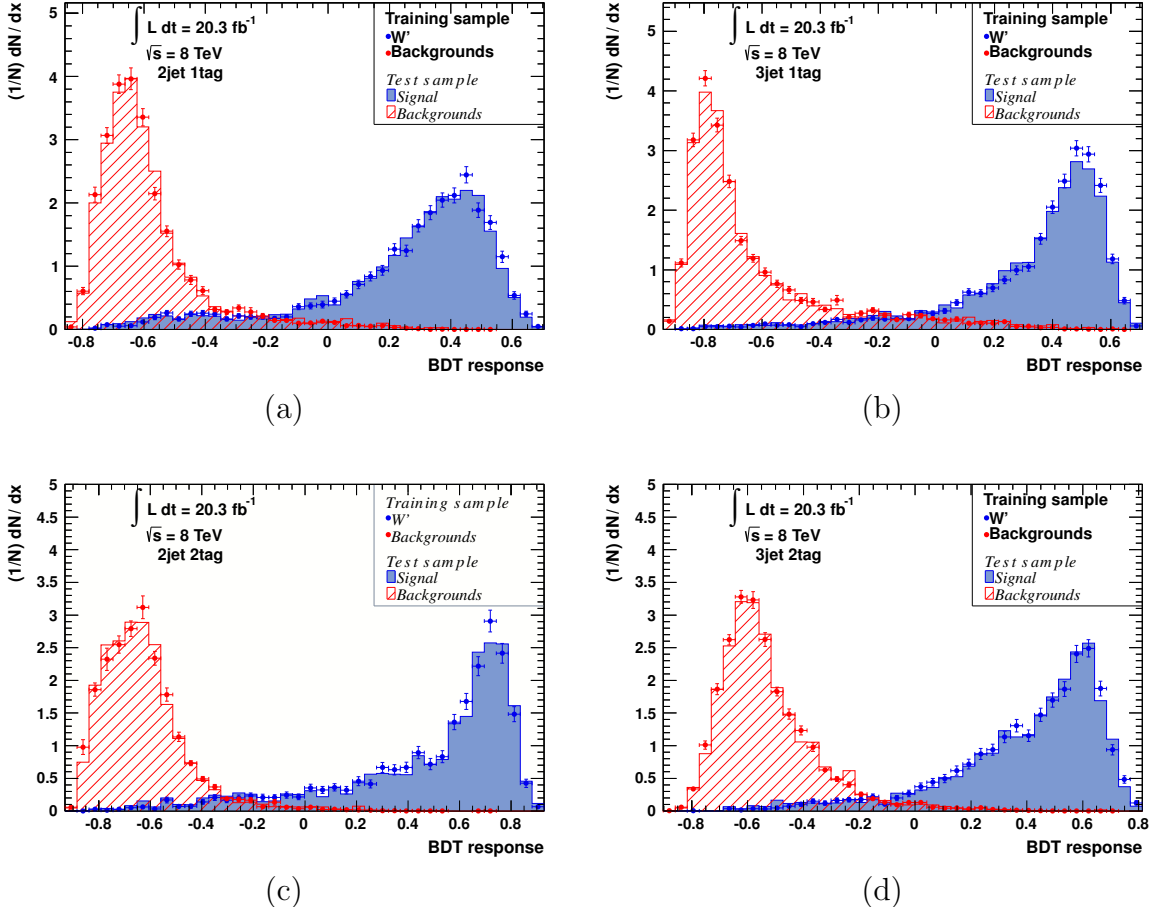


Figure 7.15: The BDT output distribution with the signal and background processes split into testing and training samples for (a) the 2jet 1tag analysis channel (b) the 2jet 2tag analysis channel (c) the 3jet 1tag analysis channel (d) the 3jet 2tag analysis channel.

Chapter 8

Statistical analysis

With the separation of background and signal events optimized by the multivariate analysis (MVA) described in Chapter 7, the statistical significance of the analysis must be determined. Possible sources of systematic error and their effects are described in Section 8.1. With no statistically significant excess of events found by the analysis, 95% confidence level (C.L.) limits are placed on the cross-section times branching ratio of W' bosons with masses in the range 0.5 TeV - 3.0 TeV. The methodology used to derive these results is described in Section 8.2, and the results are given in Section 8.3.

8.1 Systematic uncertainties

ATLAS is a complicated experiment as described in Chapter 3, and the calibration and interpretation of the detector response from the many systems introduce possible biases to the data. Additionally, the simulated Monte Carlo signal and background events may have biases in their generation and simulation which must be accounted for. Tables 8.1 and 8.2 summarize the effects of these uncertainties on the background and signal event yields.

8.1.1 Jet energy scale (JES)

The jet energy scale (JES) uncertainty represents the potential bias in the measurement of the jet energies and includes both theoretical and experimental components. The theoretical

Systematic Uncertainty	2jets 1tag		3jets 1tag	
	Signal	Background	Signal	Background
JES				
JER				
Jet Reconstruction				
JVF				
b-tagging				
LES/LER				
Lepton Reconstruction				
MET				
PDF				
ISR/FSR				
MC Generator				
Theory Normalization				
W+jets Normalization				
Multijet Normalization				
Luminosity				

Table 8.1: Summary table of the systematic shifts in signal and background event yields of the 1tag analysis channels.

Systematic Uncertainty	2jets 2tag		3jets 2tag	
	Signal	Background	Signal	Background
JES				
JER				
Jet Reconstruction				
JVF				
b-tagging				
LES/LER				
Lepton Reconstruction				
MET				
PDF				
ISR/FSR				
MC Generator				
Theory Normalization				
W+jets Normalization				
Multijet Normalization				
Luminosity				

Table 8.2: Summary table of the systematic shifts in signal and background event yields of the 2tag analysis channels.

components of the uncertainty come from the use of Monte Carlo simulations to derive the nominal JES correction factors for jets, while the experimental components of the uncertainty come from an imperfect knowledge of the conditions a collision takes place in, such as the pileup. To estimate these uncertainties additional Monte Carlo samples are produced with varied simulation conditions and compared to data. In order to derive the JES calibration the energy of a jet is balanced in p_T against a reference object. This reference object can be a photon, a leptonically decaying Z boson, a jet in a different pseudorapidity region of the detector, or several jets with lower p_T . Each of these types of reference objects contributes to the overall calibration differently depending on the pseudorapidity and p_T of the jet [51]. The effects of the JES uncertainty on the W' search are evaluated by generating Monte Carlo samples with $+1\sigma$ and -1σ shifts in JES and applying the event selection and multivariate analysis to them.

8.1.2 Jet energy resolution (JER)

The jet energy resolution (JER) uncertainty is the precision with which the energy of jets can be measured by the ATLAS detector. The JER uncertainty is estimated by measuring the p_T balance in dijet events [52]. In order to assess the effect of this resolution on the W' search Monte Carlo samples are generated with all of the jet energies modified by a random offset chosen using a Gaussian distribution with a standard deviation equal to the measured JER uncertainty and the event selection and multivariate analysis are applied to the modified sample.

8.1.3 Jet reconstruction efficiency

The effects of the efficiency of the jet reconstruction algorithm on the W' search are estimated by randomly removing jets from the simulated events according to the jet reconstruction efficiency. This efficiency is determined by matching jets reconstructed from tracking information with jets reconstructed from the calorimeter. The modified sample has the event selection and multivariate analysis applied to it and half of the difference in the BDT weight distribution between the modified sample and nominal sample is taken as a symmetric uncertainty around the nominal values [53].

8.1.4 Jet vertex fraction (JVF)

The jet vertex fraction (JVF) is the fraction of each jet’s total p_T with tracks pointing to the event’s primary vertex. This is a useful variable for removing pileup jets and a cut is applied to it for each jet as described in Section 4.3. The uncertainty in the efficiency of this cut is determined by taking the difference in cut values necessary to attain the same jet efficiency in data and Monte Carlo Z+jets samples [54]. New Monte Carlo samples are produced with the JVF cut varied up and down from the nominal value by this uncertainty and these modified samples have the event selection and multivariate analysis applied to them to determine the effect on the BDT weight distribution.

8.1.5 b-tagging performance

The MV1 b-tagging algorithm is described in Section 4.3.1 and is central to the analysis for background rejection and the definition of the analysis channels. The MV1 algorithm provides an output for each jet which a cut is applied to in order to achieve 70% b-tagging

efficiency. The b-tagging efficiency, c-tagging efficiency, and mis-tagging rate are all measured in data by applying the MV1 algorithm to analysis channels with high purities of b-jets, c-jets, and light flavor jets respectively. The b-tagging efficiency, c-tagging efficiency, and mis-tagging rate thus all have uncertainties derived from the systematic and statistical uncertainties in their measurement [39, 55, 56]. The effects of these uncertainties is evaluated by reweighting the Monte Carlo events by $\pm 1\sigma$ shifts in each.

8.1.6 Lepton energy scale and resolution

The lepton energy scale and resolution uncertainties are determined by comparing $Z \rightarrow ll$ data and Monte Carlo events. The lepton energy scale is binned in E_T and pseudorapidity and the difference in the dilepton invariant mass peak in each bin determines the lepton energy scale uncertainty for that bin. The lepton energy resolution is not binned and the difference in the width of the simulated and measured widths of the dilepton invariant mass peak determines the uncertainty in the lepton energy resolution [57, 58]. The effects of the lepton energy scale uncertainty are evaluated by producing Monte Carlo samples with $+1\sigma$ and -1σ shifts in the lepton energy scale and applying the event selection and multivariate analysis to them. The effects of the lepton energy resolution are determined by modifying the nominal lepton energies by a random offset chosen using a Gaussian distribution with a standard deviation equal to the lepton energy resolution uncertainty and applying the event selection and multivariate analysis to the modified events.

8.1.7 Lepton trigger and reconstruction

The simulated Monte Carlo events are weighted by lepton trigger and reconstruction efficiencies measured in the $Z \rightarrow ll$ and $W \rightarrow l\nu$ channels. These efficiencies are functions of the lepton kinematics and are determined by relaxing the respective requirements and measuring how often the original trigger or reconstruction requirements are met. The uncertainty in these efficiencies is determined by taking half the difference in the measured data and Monte Carlo efficiencies as a symmetric uncertainty about the nominal value [57, 58].

8.1.8 Missing transverse energy (MET)

As described in Section 4.4, the MET calculation contains terms for the leptons, jets, soft jets, and cell-out energy. The effects of the uncertainty in the lepton or jet terms are included in the lepton and jet energy scale and resolution uncertainties. The uncertainty in the soft jet and cell-out terms is estimated using a $Z \rightarrow \mu\mu$ sample with no jets having $p_T > 20$ GeV. The projection of the MET onto the reconstructed Z boson's transverse direction is calculated for a data sample and Monte Carlo simulated sample. The average deviation from unity, defined as the ratio of this variable between the data and Monte Carlo samples, is taken as the uncertainty in the soft jets and cell-out energy [40]. New Monte Carlo samples are generated with each of these varied up and down by this uncertainty and the event selection and multivariate analysis are applied to these samples to evaluate the effect on the final BDT weight distribution.

8.1.9 Parton distribution function (PDF)

Estimates of the uncertainties in the parton distribution functions are provided by their authors as a set of uncertainty eigenvectors. The Monte Carlo samples are reweighted according to each of the 68% C.L. uncertainty eigenvectors for CT10, MWST2008NLO68CL [59], and NNPDF23 [60] and half of the largest variation from the nominal sample is taken as a symmetric uncertainty on each Monte Carlo sample.

8.1.10 Initial state radiation and final state radiation (ISR/FSR)

Initial state radiation and final state radiation (ISR/FSR) is the radiation of a particle immediately before or after the hard interaction of a process. The uncertainty in modeling these effects is estimated by varying the ISR/FSR settings of PYTHIA within the range consistent with previous measurements of $t\bar{t}$ [61]. Six additional $t\bar{t}$ samples are produced with these varied ISR/FSR settings and have the event selection and multivariate analysis applied to them. The maximum deviation of the resulting BDT weight distributions from the nominal distribution is taken as a symmetric systematic uncertainty on the sample.

8.1.11 Monte Carlo event generator and parton showering

The different Monte Carlo event generation and parton showering programs make a variety of different approximations and produce events with different kinematic distributions. To reduce the analysis' sensitivity to the effects of a specific event generator or parton shower program a systematic uncertainty is included for all top quark processes which is estimated by taking the difference from the nominal Monte Carlo sample and a Monte Carlo sample produced with another event generator or parton shower program. For the $t\bar{t}$ sample the nominal

POWHEG+PYTHIA sample is compared to samples produced with POWHEG+HERWIG, MC@NLO+HERWIG, and ALPGEN+HERWIG and the largest difference is taken as a symmetric uncertainty. The nominal single top quark t-channel sample produced with ACERMC+PYTHIA is compared to a sample produced with MC@NLO+HERWIG and the difference between the samples is taken as a symmetric uncertainty. For the single top quark s-channel the nominal POWHEG+PYTHIA sample is compared to a sample produced with MC@NLO+HERWIG and the difference is taken as a symmetric uncertainty. For the single top quark Wt channel, the nominal POWHEG+PYTHIA sample is compared to a sample produced with MC@NLO+HERWIG and samples produced with POWHEG+PYTHIA with the two different NLO calculation schemes (diagram removal and diagram subtraction) are compared to each other, and the larger difference is taken as a symmetric uncertainty on the nominal sample.

8.1.12 Theoretical cross-sections

All of the Monte Carlo samples, with the exception of the W+jets and multijets samples, are normalized to a calculated theoretical cross-section. These cross-sections have associated uncertainties in their calculation and each channel is assigned an independent flat uncertainty to account for this. The $t\bar{t}$ sample has a cross-section uncertainty of $-5.9/+5.1\%$. For the single top quark processes the uncertainty in the s-channel cross-section is $\pm 3.9\%$, the uncertainty in the t-channel cross-section is $-2.1/+3.9\%$, and the uncertainty in the Wt channel cross-section is $\pm 6.8\%$. The Z+jets and diboson samples both have a cross-section uncertainty of 42%.

8.1.13 W+jets normalization

The W+jets Monte Carlo samples are normalized using a data driven technique described in Section 5.2.1. An uncertainty in this normalization is determined by applying each of the applicable uncertainties described in this Section to the control region used to derive the W+jets normalization. The variation in the normalization caused by each of these individual uncertainties is then added in quadrature to calculate the total W+jets normalization uncertainty.

8.1.14 Multijet normalization

The multijet background is normalized using the matrix method as described in Section 5.2.2. Since this is a small background and a detailed estimation of the uncertainty in its normalization would be very difficult, a 50% uncertainty on the sample's normalization is applied.

8.1.15 Luminosity

There is a $\pm 3.6\%$ uncertainty in the luminosity of the data set used for this analysis, which is preliminary result derived from updated van der Meer scans performed in April 2012 [62]. Since all of the Monte Carlo samples are normalized to this luminosity, this uncertainty is assessed as a flat $\pm 3.6\%$ uncertainty in all of the Monte Carlo samples.

8.2 Limit setting procedure

The statistical analysis for the $W' \rightarrow t\bar{b}$ search uses the CL_S method [63, 64] implemented in the MClimt software package. The CL_S method is a binned likelihood method, meaning the likelihood of each bin of the BDT weight distribution occurring is computed and then

all of the bins are combined into a global likelihood. This method was chosen because it is more powerful than a single bin counting experiment and is less sensitive to fluctuations in the background, as described below.

The CL_S method is easy to build from basic Poisson and Gaussian statistics. The likelihood of observing N events if there are μ expected events is given by Poisson statistics as:

$$\mathcal{L}(N|\mu) = \frac{\mu^N e^{-\mu}}{N!} \quad (8.1)$$

The inclusion of uncertainties into this likelihood is done by modifying the expected number of events through nuisance parameters (θ), each representing a single uncertainty. The expected number of events of each samples (N_i) is modified by the probability density function of each of the uncertainties that affect that sample (G), and then all of the samples are summed over to produce the final expected number of events as shown in Equation 8.2

$$\mu = \sum_i N_i \prod_j G(\theta_{ij}, \delta_{ij}) \quad (8.2)$$

The probability density function for each of the uncertainties can in principle be any non-negative unitary distribution, but for this analysis they are all assumed to be Gaussian distributions with a mean of 1 and a standard deviation of δ . One of the consequences of Equation 8.2 is that μ is now a multi-dimensional probability distribution and not a single value.

So far this procedure has described a single counting experiment. Each bin of the BDT weight distribution can be treated as an independent counting experiment and the likelihood of observing an event distribution (N_{obs}) with N_k events in the k^{th} bin is given by the product

of the independent bins' likelihoods as shown in Equation 8.3.

$$\mathcal{L}(N_{obs}|\theta_{ij}, \delta_{ij}) = \prod_k \frac{\mu_k^{N_k} e^{-\mu_k}}{N_k!} \quad (8.3)$$

In order to determine if a signal is excluded, 10,000 psuedo-experiments are generated for each of two hypotheses: one hyopthesis (H_1) includes the signal and all of the background processes while the other hypothesis (H_0) includes only the background processess. These pseudo-experiments are generated by randomly choosing a value for each nuisance parameter based on that parameter's probability distribution function. This shifted distribution is used to set the expected number of events of a Poisson distribution in each bin, these Poisson distributions are then randomly sampled to produce the final psuedo experiment distribution. For each psuedo experiment the log-likelihood ratio (LLR) is computed according to Equation 8.4.

$$LLR = -2\ln \left(\frac{\mathcal{L}(N|H_1)}{\mathcal{L}(N|H_0)} \right) \quad (8.4)$$

The LLR of the observed data set is also calculated and used to determine the strength of the limit on the signal process. CL_{S+B} is defined as the fraction of pseudo-experiments generated with the signal-plus-background hypothesis (H_1) with an LLR greater than the LLR of the data set. Similarly, CL_B is defined as the fraction of pseudo experiments generated with the background only hypothesis (H_0) with an LLR greater than that of the data set. CL_S is the likelihood of the signal being included in the data and is defined as the ratio of CL_{S+B} to CL_B as shown in Equation 8.5, which has the advantage of being less sensitive to fluctuations in the background modeling because they will largely cancel.

$$CL_S = \frac{CL_{S+B}}{CL_B} \quad (8.5)$$

A signal is excluded at the 95% confidence level if it has a $CL_S < 0.05$. After the signal has been excluded or not at its nominal cross-section the process is repeated with the normalization of the signal sample decreased (if the current cross-section was excluded) or increased (if the current cross-section was not excluded) by a factor k . This is iteratively repeated until CL_S equals 0.05. When this occurs the value of k can be used to determine the 95% limit on the cross-section as shown in Equation 8.6.

$$\sigma_{95\% \text{ limit}} = k\sigma_{nominal} \quad (8.6)$$

This can be taken one step further and 95% confidence level limits can be placed on the coupling strengths g'_R and g'_L . The effective Lagrangian density used to generate the signal samples was given in Equation 2.9 and is repeated here in Equation 8.7.

$$\mathcal{L}_{W'} = \frac{1}{2\sqrt{2}} V'_{ij} W'_\mu \bar{f}^i \gamma^\mu (g'_R(1 + \gamma_5) + g'_L(1 - \gamma_5)) f^j \quad (8.7)$$

The cross-sections of these processes is thus proportional to g'^2_R or g'^2_L . The signal processes were all generated with g'_R or g'_L equal to the Standard Model W coupling strength g , so the ratio of the observed limit on the cross-section to the nominal cross-section can be used to compute an equivalent limit on $\frac{g'_R}{g}$ or $\frac{g'_L}{g}$ using Equation 8.8.

$$\sqrt{k} = \sqrt{\frac{\sigma_{95\% \text{ limit}}}{\sigma_{nominal}}} = \frac{g'}{g} \quad (8.8)$$

8.3 Results

The limit setting procedure described in Section ?? is performed for each of the 22 W'_R and W'_L mass points (11 mass points each) in all four of the analysis channels (2jet 1tag, 2jet 2tag, 3jet 1tag, 3jet 2tag). The limits on cross-section times branching ratio for the W'_R mass points in each of the analysis channels are plotted in Figure ??, and the limits on cross-section times branching ratio for the W'_L mass points in each of the analysis channels are plotted in Figure ???. The red line in these plots shows the theoretical cross-section times branching ratio as a function of W' mass which is calculated with $g' = g$. The solid black line shows the observed 95% confidence level limit on the cross-section times branching ratio as a function of W' mass. The region above this line has been excluded at the 95% confidence level and regions where the theoretical cross-section times branching ratio are above the observed limit have been excluded for $g' = g$. The dashed line is the expected limit, which is derived similarly to the observed limit but is the median result of 10,000 background only pseudo-data sets used in place of the data. The green and yellow bands are the 68% (1σ) and 95% (2σ) uncertainty region of the expected limit results. The mass value where the theoretical cross-section times branching ratio crosses the observed or expected limit is known as the mass limit and is a commonly used figure of merit for exclusions such as this. The mass limits for each of the analysis channels is given in Table 8.3 for a W'_R boson and in Table 8.4 for a W'_L boson.

The limits on the cross-section times branching ratio can also be used to calculate limits on $\frac{g'}{g}$ as described by Equation 8.8. By using the observed or expected limits on the cross-section times branching ratio, observed or expected limits on $\frac{g'_R}{g}$ and $\frac{g'_L}{g}$ can be calculated for each of the tested mass points for the W'_R and W'_L bosons respectively. These limits are

Analysis Channel	Observed Mass Limit	Expected Mass Limit
2jet 1tag		
3jet 1tag		
2jet 2tag		
3jet 2tag		

Table 8.3: Expected and observed mass limits for a W'_R boson in the individual analysis channels.

Analysis Channel	Observed Mass Limit	Expected Mass Limit
2jet 1tag		
3jet 1tag		
2jet 2tag		
3jet 2tag		

Table 8.4: Expected and observed mass limits for a W'_L boson in the individual analysis channels.

plotted as a function of the W' mass and an exclusion region is formed, as seen in Figures ?? and ??.

The individual analysis channels can also be combined by treating each channel as more bins in the BDT weight distribution. The resulting combination is analyzed in an identical manner to the individual analysis channels and similar limits can be made. Because of their kinematic similarities, the 2jet 1tag and 3jet 1tag channels are combined to form the 1tag combined channel, and the 2jet 2tag and 3jet 2tag channels are combined to form the 2tag combined channel. A final combination of all of the analysis channels forms the full combination channel. The limits on the cross-section times branching ratio for a W'_R and W'_L boson are shown in Figure ?? and ?? respectively. The derived mass limits from the combined channels for a W'_R or W'_L boson are given in Table 8.5 and 8.6. The limits on $\frac{g'_R}{g}$ and $\frac{g'_L}{g}$ are shown in Figure ?? and ??.

Analysis Channel	Observed Mass Limit	Expected Mass Limit
1tag combined		
2tag combined		
full combination		

Table 8.5: Expected and observed mass limits for a W'_R boson in the combined analysis channels.

Analysis Channel	Observed Mass Limit	Expected Mass Limit
1tag combined		
2tag combined		
full combination		

Table 8.6: Expected and observed mass limits for a W'_L boson in the combined analysis channels.

Chapter 9

Conclusion

BIBLIOGRAPHY

BIBLIOGRAPHY

- [1] J. Beringer and et al. (Particle Data Group) Phys. Rev. D86 **86** (2012) 010001, 2013 partial update for the 2014 edition.
- [2] *Expected electron performance in the ATLAS experiment*, Tech. Rep. ATL-PHYS-PUB-2011-006, CERN, Geneva, Apr, 2011.
- [3] J. Pequenao, *Computer generated image of the whole ATLAS detector*, Mar, 2008.
- [4] ATLAS Collaboration, *The ATLAS Experiment at the CERN Large Hadron Collider*, JINST **3** (2008) S08003.
- [5] J. Pequenao, *Computer generated image of the ATLAS inner detector*, Mar, 2008.
- [6] J. Pequenao, *Computer Generated image of the ATLAS calorimeter*, Mar, 2008.
- [7] J. Pequenao, *Computer generated image of the ATLAS Muons subsystem*, Mar, 2008.
- [8] L. H. Ryder, *Quantum Field Theory*. Press Syndicate of the University of Cambridge, 2006.
- [9] E. M. Henley and A. Garcia, *Subatomic Physics*. World Scientific Publishing Co. Pte. Ltd., 2007.
- [10] (Super-Kamiokande Collaboration) Collaboration, *Evidence for Oscillation of Atmospheric Neutrinos*, Phys. Rev. Lett. **81** (1998) 1562–1567.
- [11] [ATLAS Collaboration] Collaboration, G. Aad et al., *Observation of a new particle in the search for the Standard Model Higgs boson with the ATLAS detector at the LHC*, Phys. Lett. B **716** (2012) 1, arXiv:arXiv:1207.7214 [hep-ex].
- [12] [CMS Collaboration] Collaboration, S. Chatrchyan et al., *Observation of a new boson at a mass of 125 GeV with the CMS experiment at the LHC*, Phys. Lett. B **716** (2012) 30, arXiv:arXiv:1207.7235 [hep-ex].
- [13] C. Itzykson and J.-B. Zuber, *Quantum Field Theory*. McGraw-Hill, Inc., 1980.

- [14] E. Boltezar, H. Haseroth, W. Pirkl, T. Sherwood, U. Tallgren, P. Tetu, D. Warner, and M. Weiss, *The New CERN 50MeV Linac*, Proc. 1979 Linear Accelerator Conference **BNL 51134** (1979) no. 66, .
- [15] B. Mikulec, A. Blas, C. Carli, A. Findlay, K. Hanke, G. Rumolo, and J. Tan, *LHC Beams from the CERN PS Booster*, .
- [16] M. Barnes, M. Benedikt, E. W. Blackmore, A. Blas, J. Borburgh, R. Cappi, M. Chanel, V. Chohan, F. Cifarelli, G. Clark, G. Daems, L. R. Evans, A. B. Fowler, R. Garoby, J. Gonzlez, D. G. Grier, J. Gruber, S. Hancock, C. E. Hill, A. Jansson, E. Jensen, S. R. Koscielniak, A. Krusche, R. Losito, P. Maesen, F. Mammarella, K. D. Metzmacher, A. Mitra, J. Olsfors, M. Paoluzzi, J. Pedersen, R. Poirier, U. Raich, K. W. Reiniger, T. C. Ries, J. P. Riunaud, J. P. Royer, M. Sassowsky, K. Schindl, H. O. Schnauer, L. Sermeus, M. Thivent, H. M. Ullrich, W. Van Cauter, M. Vretenar, and F. V. Vlker, *The PS complex as proton pre-injector for the LHC: design and implementation report*. CERN, Geneva, 2000.
- [17] P. Collier and B. Goddard, *PREPARATION OF THE SPS AS LHC INJECTOR*. CERN, Geneva, 1998.
- [18] O. S. Brning, P. Collier, P. Lebrun, S. Myers, R. Ostojic, J. Poole, and P. Proudlock, *LHC Design Report*. CERN, Geneva, 2004.
- [19] ATLAS Collaboration Collaboration, *ATLAS detector and physics performance: Technical Design Report, 1*. Technical Design Report ATLAS. CERN, Geneva, 1999. Electronic version not available.
- [20] ATLAS Collaboration Collaboration, *ATLAS magnet system: Technical Design Report, 1*. Technical Design Report ATLAS. CERN, Geneva, 1997.
- [21] G. Aad, M. Ackers, F. A. Alberti, M. Aleppo, G. Alimonti, J. Alonso, E. C. Anderssen, A. Andreani, A. Andreadza, J.-F. Arguin, K. E. Arms, D. Barberis, M. B. Barbero, M. Bazalova, R. B. Beccherle, K. H. Becks, P. K. Behera, F. Bellina, J. Beringer, K. Bernardet, J. B. Biesiada, L. Blanquart, J. Boek, G. R. Boyd, P. Breugnon, P. Buchholz, B. Butler, M. Caccia, A. C. Capsoni, C. Caso, D. Cauz, M. Cepeda, R. Cereseto, M. Cervetto, M. L. Chu, M. Citterio, J. C. Clemens, Y. C. Coadou, M. Cobal, A. Coccaro, S. Coelli, S. Corrard, M. Cristinziani, S. Cuneo, S. Dauria, M. Dameri, G. Darbo, S. Dardin, B. DeLotto, U. De Sanctis, J. B. De Vivie De Regie, C. del Papa, P. Delpierre, B. Di Girolamo, W. Dietsche, F. Djama, D. Dobos, M. Donega, J. Dopke, K. Einsweiler, A. Eyring, D. Fasching, L. Feligioni, D. Ferguson, W. Fernando, P. Fischer, M. J. Fisher, T. Flick, G. Gagliardi, E. Galyaev, K. K. Gan, M. Garca-Sciveres, N. Garelli, G. G. Gariano, G. G. Gaycken,

C. Gemme, P. Gerlach, M. G. D. Gilchriese, M. P. Giordani, D. Giugni, K. W. Glitza, C. Gssling, T. Golling, F. Goozen, I. Gorelov, G. Gorfine, C. Grah, H. M. Gray, I. M. Gregor, J. Grosse-Knetter, K. Grybel, P. Gutierrez, G. D. Hallewell, N. Hartman, M. Havranek, B. Heinemann, T. Hen, M. R. Hoeferkamp, D. Hoffmann, M. Holder, W. Honerbach, C. Horn, S. Hou, G. S. Huang, F. Huegging, E. W. Hughes, I. Ibragimov, I. Ilyashenko, M. Imhaeuser, J. M. Izen, J. Jackson, D. Jana, R. C. Jared, P. Jez, T. Johnson, J. Joseph, H. Kagan, M. Karagounis, R. D. Kass, M. Keil, S. Kersten, P. Kind, J. Klaiber-Lodewigs, L. Klingbeil, R. Klingenberg, A. Korn, V. V. Kostyukhin, I. Kostyukhina, O. Krasel, H. Krger, K. Krger, J. Kudlaty, T. Khl, O. Kvashnicka, K. Lantzsch, T. Lari, S. L. Latorre, S. C. Lee, T. Lenz, G. Lenzen, J. Lepidis, J. Levque, M. Leyton, D. Lopez Mateos, K. F. Loureiro, D. Lke, L. Luisa, J. Lys, R. J. Madaras, P. Mttig, F. M. Manca, E. Mandelli, M. Marcisovsky, Z. Marshall, G. Martnez, L. Masetti, M. Ma, M. Mathes, R. McKay, G. Meddeler, R. Meera-Lebbai, C. Meroni, J. Metcalfe, W. T. Meyer, D. W. Miller, W. Miller, S. Montesano, M. M. Monti, P. Morettini, J. M. Moss, T. Mouthuy, P. Nechaeva, W. Ockenfels, G. A. Odino, M. Olcese, B. Osculati, F. Parodi, A. Pekedis, K. Perez, I. Peric, C. Pizzorno, J. Popule, R. Post, F. Ragusa, A. M. Rahimi, B. Raith, S. Rajek, K. Reeves, I. Reisinger, J. D. Richardson, E. I. Rosenberg, L. P. Rossi, I. Rottlnder, A. R. Rovani, A. Rozanov, O. Runlfsson, E. R. Ruscino, A. F. Saavedra, F. S. Sabatini, M. Saleem, S. Sandvoss, B. Sanny, L. Santi, M. I. Scherzer, C. Schiavi, A. Schreiner, J. Schultes, A. Schwartzman, R. Seibert, S. C. Seidel, H. Severini, S. Shanava, P. Scho, P. Skubic, A. C. Smith, D. S. Smith, J. Snow, T. Stahl, T. Stockmanns, S. Strandberg, M. Strauss, D. Ta, F. Tegenfeldt, P. K. Teng, R. Ter-Antonian, J. Thadome, T. Tic, L. Tomasek, M. Tomasek, F. Tomasi, K. Toms, C. Tran, J. Treis, N. Triplett, C. Troncon, L. Vacavant, S. Vahsen, J. Valenta, G. Vegni, F. Vernocchi, E. Vigeolas, J. Virzi, E. Viscione, V. Vrba, J. Walbersloh, W. Walkowiak, J. Weber, T. F. Weber, J. Weingarten, C. Weldon, N. Wermes, U. Werthenbach, J. S. Wirth, R. Witharm, B. Witt, M. Wittgen, J. Wstenfeld, R. Wunstorf, J. Wyckoff, W.-M. Yao, C. Young, R. Zaidan, M. Zdrazil, F. Zetti, J. Zhong, M. Ziolkowski, G. Zizka, and M. M. Zoeller, *ATLAS pixel detector electronics and sensors*, J. Instrum. **3** (2008) P07007.

- [22] A. Abdesselam and T. Akimoto, *The Barrel Modules of the ATLAS SemiConductor Tracker*, Tech. Rep. ATL-INDET-PUB-2006-005. ATL-COM-INDET-2006-009. CERN-ATL-COM-INDET-2006-009, CERN, Geneva, Jul, 2006.
- [23] A. Abdesselam and F. Anghinolfi, *The ATLAS semiconductor tracker end-cap module*, Nucl. Instrum. Methods Phys. Res., A **575** (2007) no. 3, 353–389.
- [24] ATLAS Collaboration, *The ATLAS TRT barrel detector*, Journal of Instrumentation **3** (2008) no. 02, P02014.
- [25] ATLAS Collaboration, *The ATLAS TRT end-cap detectors*, Journal of

- [26] A. Bingl, *The ATLAS TRT and its Performance at LHC*, Journal of Physics: Conference Series **347** (2012) no. 1, 012025.
- [27] B. Aubert, B. Beaugiraud, J. Colas, P. Delebecque, L. D. Ciaccio, M. E. Kacimi, P. Ghez, C. Girard, M. Gouanre, D. Goujdami, A. Jeremie, S. Jzquel, R. Lafaye, N. Massol, P. Perrodo, H. Przysiezniak, G. Sauvage, J. Thion, I. Wingerter-Seez, R. Zitoun, Y. Zolnierowski, R. Alforque, H. Chen, J. Farrell, H. Gordon, R. Grandinetti, R. Hackenburg, A. Hoffmann, J. Kierstead, J. Koehler, F. Lanni, D. Lissauer, H. Ma, D. Makowiecki, T. Muller, S. Norton, V. Radeka, D. Rahm, M. Rehak, S. Rajagopalan, S. Rescia, K. Sexton, J. Sondericker, I. Stumer, H. Takai, A. Belymam, D. Benchekroun, C. Driouichi, A. Hoummada, M. Hakimi, M. Knee, R. Stroynowski, B. Wakeland, V. Datskov, V. Drobin, M. Aleksa, J. Bremer, T. Carli, M. Chalifour, J. Chevalley, F. Djama, L. Ema, C. Fabre, P. Fassnacht, F. Gianotti, A. Gonidec, J. Hansen, L. Hervas, T. Hott, C. Lacaste, C. Marin, P. Pailler, A. Pleskatch, D. Sauvage, G. Vandoni, V. Vuillemin, H. Wilkens, S. Albrand, B. Belhorma, J. Collot, P. de Saintignon, D. Dzahini, A. Ferrari, J. Fulachier, M. Gallin-Martel, J. Hostachy, G. Laborie, F. Ledroit-Guillon, P. Martin, J. Muraz, F. Ohlsson-Malek, S. Saboumazrag, S. Viret, R. Othegraven, C. Zeitnitz, D. Banfi, L. Carminati, D. Cavalli, M. Citterio, G. Costa, M. Delmastro, M. Fanti, L. Mandelli, M. Mazzanti, F. Tartarelli, E. Aug, S. Baffioni, J. Bonis, W. Bonivento, C. Bourdarios, C. D. la Taille, L. Fayard, D. Fournier, G. Guilhem, P. Imbert, L. Iconomidou-Fayard, G. L. Meur, M. Mencik, J.-M. Noppe, G. Parrou, P. Puzo, D. Rousseau, A.-C. Schaffer, N. Seguin-Moreau, L. Serin, G. Unal, J.-J. Veillet, F. Wicek, D. Zerwas, F. Astesan, W. Bertoli, B. Canton, F. Fleuret, D. Imbault, D. Lacour, B. Laforge, P. Schwemling, E. Abouelouafa, A. B. Mansour, R. Cherkaoui, Y. E. Mouahhidi, H. Ghazlane, A. Idrissi, K. Bazizi, D. England, V. Glebov, T. Haelen, F. Lobkowicz, P. Slattery, J. Belorgey, N. Besson, M. Boonekamp, D. Durand, J. Ernwein, B. Mansouli, F. Molini, J. Meyer, P. Perrin, J. Schwindling, J. Taguet, H. Zacccone, B. Lund-Jensen, S. Rydstroem, Y. Tayalati, B. Botchev, G. Finocchiaro, J. Hoffman, R. McCarthy, M. Rijssenbeek, J. Steffens, M. Zdrazil, and H. Braun, *Construction, assembly and tests of the {ATLAS} electromagnetic barrel calorimeter*, Nuclear Instruments and Methods in Physics Research Section A: Accelerators, Spectrometers, Detectors and Associated Equipment **558** (2006) no. 2, 388 – 418.
- [28] M. Andrieux, B. Belhorma, A. Belymam, D. Benchekroun, R. Cherkaoui, C. Clement, J. Collot, P. de Saintignon, C. Driouichi, D. Dzahini, Y. E. Mouahhidi, H. Erridi, A. Ferrari, H. Ghazlane, J. Hostachy, A. Hoummada, A. Idrissi, G. Laborie, B. Lund-Jensen, P. Martin, J. Muraz, and J. Soederqvist, *Construction and test of the first two sectors of the ATLAS barrel liquid argon presampler*, Nuclear Instruments and Methods in Physics Research Section A: Accelerators, Spectrometers, Detectors and Associated Equipment **479** (2002) no. 2-3, 316 – 333.

- [29] A. E. L. A. E. C. Group, M. Aleksić, F. Astesan, D. Banfi, F. Barreiro, P. Barrillon, C. Benchouk, W. Bertoli, J. Bremer, H. M. Braun, B. Canton, L. Carminati, T. Carli, C. Cerna, M. Chalifour, J. L. Chevalley, M. Citterio, J. Collot, G. Costa, P. Dargent, B. Dekhissi, J. E. Derkaoui, F. Djama, C. Fabre, A. Fallou, M. Fanti, P. Fassnacht, D. Fournier, C. G. Ruiz, F. Gianotti, J. Giner, A. Gonidec, F. Henry-Couannier, L. Hervas, T. Hott, F. Hubaut, D. Imbault, P. Karst, V. A. Kazanin, K. Y. Kotov, L. Labarga, D. Lacour, B. Laforge, P. Lopez-Iturriaga, G. Mac, V. Malychev, L. Mandelli, P. S. Mangeard, B. Mansouli, C. P. Marin, A. L. Maslennikov, M. Mazzanti, J. P. Meyer, E. Monnier, E. N. D. Busto, V. Niess, C. Oliver, I. A. Orlov, P. M. Pailler, S. V. Peleganchuk, J. D. Peso, A. Pleskatch, P. Pralavorio, S. Prat, P. Puzo, M. Raymond, B. Resende, S. Rodier, P. Romero, F. Rossel, D. Sauvage, A. G. Schamov, P. Schwemling, J. Schwindling, C. Serfon, J. Setien, L. Serin, A. Soukharev, C. D. L. Taille, A. Talyshев, G. Tartarelli, Y. A. Tikhonov, S. Tisserant, J. Toth, G. Unal, G. Vandoni, J. J. Veillet, V. Vuillemin, H. G. Wilkens, and H. Zhang, *Construction, assembly and tests of the ATLAS electromagnetic end-cap calorimeters*, Journal of Instrumentation **3** (2008) no. 06, P06002.
- [30] ATLAS TileCal Collaboration, J. Abdallah, P. Adragna, C. Alexa, R. Alves, P. Amaral, A. Ananiev, K. Anderson, X. Andresen, A. Antonaki, V. Batusov, P. Bednar, E. Bergeaas, C. Biscarat, O. Blanch, G. Blanchot, C. Bohm, V. Boldea, F. Bosi, M. Bosman, C. Bromberg, Y. A. Budagov, D. Calvet, C. Cardeira, T. Carli, J. Carvalho, M. Cascella, M. V. Castillo, J. Costello, M. Cavalli-Sforza, V. Cavasinni, A. S. Cerqueira, C. Clment, M. Cobal, F. Cogswell, S. Constantinescu, D. Costanzo, P. Da Silva, M. Davidek, T. David, J. Dawson, K. De, T. Del Prete, B. Di Girolamo, S. Dita, J. Dolejsi, Z. Dolezal, A. Dotti, R. Downing, G. Drake, I. Efthymiopoulos, D. Errede, S. Errede, A. Farbin, D. Fassouliotis, E. Feng, A. Fenyuk, C. Ferdi, B. C. Ferreira, A. Ferrer, V. Flaminio, J. Flix, P. Francavilla, E. Fullana, V. Garde, K. Gellerstedt, V. Giakoumopoulou, V. Giangiobbe, O. Gildemeister, V. Gilewsky, N. Giokaris, N. Gollub, A. Gomes, V. Gonzlez, J. Gouveia, P. Grenier, P. Gris, V. Guarino, C. Guicheney, A. Sen-Gupta, H. Hakobyan, M. Haney, S. Hellman, A. Henriques, E. Hign, N. Hill, S. Holmgren, I. Hruska, M. Hurwitz, J. Huston, I. Jen-La Plante, K. Jon-And, T. Junk, A. Karyukhin, J. Khubua, J. Klereborn, S. Kopikov, I. Korolkov, P. Krivkova, Y. Kulchitsky, Y. Kurochkin, P. Kuzhir, V. Lapin, T. Le Compte, R. Lefvre, R. Leitner, J. Li, M. Liablin, M. Lokajcek, Y. Lomakin, P. Lourtie, L. Lovas, A. Lupi, C. Maidantchik, A. Maio, S. Maliukov, A. Manousakis, C. Marques, F. Marroquim, F. Martin, E. Mazzoni, F. S. Merritt, A. Myagkov, R. Miller, I. Minashvili, L. Miralles, G. Montarou, S. Nmcek, M. Nessi, I. Nikitine, L. Nodulman, O. Norniella, A. Onofre, M. Oreglia, B. Palan, D. Pallin, D. Pantea, A. Pereira, J. E. Pilcher, J. Pina, J. Pinho, E. Pod, F. Podlyski, X. Portell, J. Poveda, L. Pribyl, L. E. Price, J. Proudfoot, M. Ramalho, M. Ramstedt, L. Raposeiro, J. Reis, R. Richards, C. Roda, V. Romanov, P. Rosnet, P. Roy, A. Ruiz, V. Rumiantsev, N. Russakovich, J. Sada Costa, O. Salto, B. Salvacha, E. Sanchis, H. Sanders, C. Santoni, J. Santos, J. G. Saraiva, F. Sarri, L. P. Says, G. Schlager, J. L. Schlereth, J. M. Seixas, B. Selldn,

N. Shalanda, P. Shevtsov, M. Shochet, V. Simaitis, M. Simonyan, A. Sisakian, J. Sjlin, C. Solans, A. Solodkov, J. Solovianov, O. Silva, M. Sosebee, F. Span, P. Speckmeyer, R. Stanek, E. Starchenko, P. Starovoitov, M. Suk, I. Sykora, F. Tang, P. Tas, R. Teuscher, S. Tokar, N. Topilin, J. Torres, D. Underwood, G. Usai, A. Valero, S. Valkr, J. A. Valls, A. Vartapetian, F. Vazeille, C. Vellidis, F. Ventura, I. Vichou, I. Vivarelli, M. Volpi, A. White, A. Zaitsev, A. Zenin, T. Zenis, Z. Zenonos, S. Zenz, and B. Zilka, *Design, Construction and Installation of the ATLAS Hadronic Barrel Scintillator-Tile Calorimeter*, Tech. Rep. ATL-TILECAL-PUB-2008-001. ATL-COM-TILECAL-2007-019, CERN, Geneva, Nov, 2007.

- [31] D. M. Gingrich, G. Lachat, J. L. Pinfold, J. Soukup, D. Axen, C. Cojocaru, G. Oakham, M. O'Neill, M. G. Vincter, M. Alekса, J. Bremer, M. Chalifour, C. Fabre, P. Fassnacht, A. Gonidec, P. Pailler, G. Vandoni, A. Cheplakov, V. Datskov, V. Drobin, A. Fedorov, S. Golubykh, N. Javadov, V. Kalinnikov, S. Kakurin, M. Kazarinov, V. Kukhtin, E. Ladygin, A. Lazarev, A. Neganov, I. Pisarev, N. Rousakovitch, E. Serochkin, S. N. Shilov, A. N. Shalyugin, Y. Usov, J. Bn, D. Bruncko, E. Kladiva, P. Stavina, P. Strzenec, M. Heldmann, M. Hohlfeld, K. Jakobs, L. Kpke, E. Marschalkowski, D. Meder, R. Othegraven, U. Schfer, D. Schroff, H. Secker, J. Thomas, W. Walkowiak, C. Zeitnitz, G. Azuelos, P.-A. Delsart, C. Leroy, R. Mazini, R. Mehdiyev, A. Akimov, M. Blagov, A. Komar, A. Snesarev, M. N. Speransky, V. Sulin, M. Yakimenko, M. Aderholz, T. Barillari, H. Brettel, W. Cwienk, J. Fent, A. Fischer, J. Habring, J. Huber, A. Karev, A. E. Kiryunin, L. Kurchaninov, H. Laskus, S. Menke, P. Mooshofer, H. Oberlack, D. Salihagic, P. Schacht, H. Schmcker, H. Stenzel, D. Striegel, W. Tribanek, J. Zimmer, T. Chen, J. Ping, M. Qi, A. Falou, G. Mace, S. V. Chekulaev, S. Denisov, M. Levitsky, A. Minaenko, G. Y. Mitrofanov, A. Moiseev, A. Pleskatch, V. V. Sytnik, L. Zakamsky, P. Benoit, K. W. Hoyle, A. Honma, M. J. Losty, R. Maharaj, C. J. Oram, E. W. Pattyn, M. Roswick, C. Sbarra, H. P. Wellisch, M. Wielers, P. S. Birney, M. Dobbs, M. Fincke-Keeler, D. Fortin, T. A. Hodges, T. Ince, N. Kanaya, R. K. Keeler, R. Langstaff, M. Lefebvre, R. A. McPherson, D. C. O'Neil, R. Seuster, D. Forbush, P. Mockett, F. Toevs, and H. M. Braun, *Construction, assembly and testing of the ATLAS hadronic end-cap calorimeter*, Tech. Rep. ATL-LARG-PUB-2007-009. CERN-ATL-COM-LARG-2007-006, CERN, Geneva, Apr, 2007.
- [32] R. S. Orr, *THE ATLAS FORWARD CALORIMETER*, Tech. Rep. ATL-LARG-PROC-2011-007, CERN, Geneva, Oct, 2011.
- [33] *The ATLAS Forward Calorimeter*, JINST **3** (2008) no. 02, P02010. <http://stacks.iop.org/1748-0221/3/i=02/a=P02010>.
- [34] ATLAS Collaboration Collaboration, *ATLAS muon spectrometer: Technical Design Report*. Technical Design Report ATLAS. CERN, Geneva, 1997. distribution.

- [35] ATLAS Collaboration Collaboration, *ATLAS level-1 trigger: Technical Design Report*. Technical Design Report ATLAS. CERN, Geneva, 1998.
- [36] ATLAS Collaboration Collaboration, P. Jenni, M. Nessi, M. Nordberg, and K. Smith, *ATLAS high-level trigger, data-acquisition and controls: Technical Design Report*. Technical Design Report ATLAS. CERN, Geneva, 2003.
- [37] M. Cacciari, G. Salam, and G. Soyez, *The anti- kt jet clustering algorithm*, Journal of High Energy Physics **2008** (2008) no. 04, 063.
- [38] ATLAS Collaboration Collaboration, *b-jet tagging calibration on c-jets containing D^{*+} mesons*, Tech. Rep. ATLAS-CONF-2012-039, CERN, Geneva, Mar, 2012.
- [39] ATLAS Collaboration Collaboration, *Commissioning of the ATLAS high-performance b-tagging algorithms in the 7 TeV collision data*, Tech. Rep. ATLAS-CONF-2011-102, CERN, Geneva, Jul, 2011.
- [40] *Performance of Missing Transverse Momentum Reconstruction in ATLAS studied in Proton-Proton Collisions recorded in 2012 at 8 TeV*, Tech. Rep. ATLAS-CONF-2013-082, CERN, Geneva, Aug, 2013.
- [41] GEANT4 Collaboration, S. Agostinelli et al., *GEANT4: A simulation toolkit*, Nucl. Instrum. Meth. A **506** (2003) 250–303.
- [42] J. Alwall, M. Herquet, F. Maltoni, O. Mattelaer, and T. Stelzer, *MadGraph 5 : Going Beyond*, JHEP **1106** (2011) 128, [arXiv:1106.0522 \[hep-ph\]](https://arxiv.org/abs/1106.0522).
- [43] T. Sjostrand, S. Mrenna, and P. Skands, *PYTHIA Generator version 6.418*, JHEP **05** (2006) 026.
- [44] P. Nason, *A new method for combining NLO QCD computations with parton shower simulations*, JHEP 11(2004)-040, hep-ph/0409146 (2004) .
- [45] G. Corcella et al., *HERWIG 6.5: an event generator for Hadron Emission Reactions With Interfering Gluons (including supersymmetric processes)*, JHEP **01** (2001) 010.
- [46] M. L. Mangano, M. Moretti, F. Piccinini, R. Pittau, and A. D. Polosa, *ALPGEN, a generator for hard multiparton processes in hadronic collisions*, JHEP **07** (2003) 001.

- [47] B. P. Kersevan and R. W. Elzbieta, *The Monte Carlo Event Generator AcerMC version 3.5 with interfaces to PYTHIA 6.4, HERWIG 6.5 and ARIADNE 4.1*, hep-ph/0405247 (2008) .
- [48] B. P. e. a. Roe, *Boosted Decision Trees as an Alternative to Artificial Neural Networks for Particle Identification*, physics/0408124v2 (2004) .
- [49] A. Hoecker, P. Speckmayer, J. Stelzer, J. Therhaag, E. von Toerne, and H. Voss, *TMVA: Toolkit for Multivariate Data Analysis*, PoS **ACAT** (2007) 040, arXiv:physics/0703039.
- [50] F. J. Massey, *The Kolmogorov-Smirnov Test for Goodness of Fit*, Journal of the American Statistical Association **46** (1951) no. 253, 68–78.
- [51] S. Adomeit, F. Balli, T. Carli, C. Doglioni, D. Gillberg, G. Halladjian, B. Malaescu, L. Mijovic, C. Meyer, A. Picazio, S. Schramm, A. Schwartzman, J. Taenzer, K. Terashi, and D. Lopez Mateos, *Jet energy scale and its systematic uncertainty in proton-proton collisions at $\sqrt{s}=7$ TeV with ATLAS 2011 data*, Tech. Rep. ATLAS-COM-CONF-2012-171, CERN, Geneva, Aug, 2012.
- [52] [ATLAS Collaboration] Collaboration, G. Aad et al., *Jet energy resolution in proton-proton collisions at $\sqrt{s}=7$ TeV recorded in 2010 with the ATLAS detector*, The European Physical Journal C **73** (2013) no. 3, 1–27. <http://dx.doi.org/10.1140/epjc/s10052-013-2306-0>.
- [53] ATLAS Collaboration, *Jet Reconstruction Efficiency*, <https://twiki.cern.ch/twiki/bin/viewauth/AtlasProtected/TopJetReconstructionEfficiency>.
- [54] T. A. collaboration, *Pile-up subtraction and suppression for jets in ATLAS*, .
- [55] ATLAS Collaboration Collaboration, *b-jet tagging calibration on c-jets containing D^{*+} mesons*, Tech. Rep. ATLAS-CONF-2012-039, CERN, Geneva, Mar, 2012.
- [56] ATLAS Collaboration Collaboration, *Measurement of the Mistag Rate with 5 fb^{-1} of Data Collected by the ATLAS Detector*, Tech. Rep. ATLAS-CONF-2012-040, CERN, Geneva, Mar, 2012.
- [57] G. Aad et al., *Electron performance measurements with the ATLAS detector using the 2010 LHC proton-proton collision data*, The European Physical Journal C **72** (2012) no. 3, 1–46. <http://dx.doi.org/10.1140/epjc/s10052-012-1909-1>.

- [58] *Preliminary results on the muon reconstruction efficiency, momentum resolution, and momentum scale in ATLAS 2012 pp collision data*, Tech. Rep. ATLAS-CONF-2013-088, CERN, Geneva, Aug, 2013.
- [59] A. Martin, W. Stirling, R. Thorne, and G. Watt, *Uncertainties on alpha(S) in global PDF analyses and implications for predicted hadronic cross sections*, Eur.Phys.J. **C64** (2009) 653–680, arXiv:0905.3531 [hep-ph].
- [60] R. D. Ball, L. Del Debbio, S. Forte, A. Guffanti, J. I. Latorre, et al., *A first unbiased global NLO determination of parton distributions and their uncertainties*, Nucl.Phys. **B838** (2010) 136–206, arXiv:1002.4407 [hep-ph].
- [61] ATLAS Collaboration Collaboration, G. Aad et al., *Measurement of $t\bar{t}$ production with a veto on additional central jet activity in pp collisions at $\sqrt{s} = 7$ TeV using the ATLAS detector*, Eur.Phys.J. **C72** (2012) 2043, arXiv:1203.5015 [hep-ex].
- [62] ATLAS Collaboration, G. Aad et al., *Improved luminosity determination in pp collisions at $\sqrt{s} = 7$ TeV using the ATLAS detector at the LHC*, Eur.Phys.J. **C73** (2013) 2518, arXiv:1302.4393 [hep-ex].
- [63] T. Junk, *Confidence level computation for combining searches with small statistics*, Nucl.Instrum.Meth. **A434** (1999) 435–443, arXiv:hep-ex/9902006 [hep-ex].
- [64] A. L. Read, *Presentation of search results: the CL_s technique*, J. Phys. G **28** (2002) no. 10, 2693–704.